THE COLUMNAR TO EQUIAXED TRANSITION IN NICKEL BASED SUPERALLOYS AM1 AND MAR-M200+Hf

by

JOHN WILLIAM FERNIHOUGH

B.A.Sc., The University of British Columbia, 1990

A THESIS SUBMITTED IN PARTIAL FULFILLMENT OF
THE REQUIREMENTS FOR THE DEGREE OF

DOCTOR OF PHILOSOPHY

in

THE FACULTY OF GRADUATE STUDIES

(Department of Metals and Materials Engineering)

We accept this thesis as conforming
to the required standard

THE UNIVERSITY OF BRITISH COLUMBIA

June 1995

In presenting this thesis in partial fulfilment of the requirements for an advanced degree at the University of British Columbia, I agree that the Library shall make it freely available for reference and study. I further agree that permission for extensive copying of this thesis for scholarly purposes may be granted by the head of my department or by his or her representatives. It is understood that copying or publication of this thesis for financial gain shall not be allowed without my written permission.

(Signature)

Department of Metals and Materials Engineering

The University of British Columbia
Vancouver, Canada

Date 29 June 1995

ABSTRACT

The columnar to equiaxed transition (CET) in Ni based superalloys AM1, electron beam remelted AM1 and MAR-M200+Hf was studied using bars instrumented with thermocouples to determine the critical solidification conditions leading to the CET. Two sets of experiments were conducted in the course of the work: the first set using investment cast moulds solidified in the experimental Bridgeman furnace at SNECMA, France. The second set of experiments consisted of directionally solidifying a bar using a copper chill for heat extraction, and were conducted at the University of British Columbia. Despite similar results of thermal gradient and solidification rate during each of the two sets of experiments, a CET was consistently obtained with the UBC experiments while not with the SNECMA experiments. The critical difference was found to be the shape of the liquid/solid interface, which was flat and horizontal in the UBC experiments but extremely curved concave upwards in the SNECMA experiments due to nature of the heat transfer. Hence the bars cast at SNECMA were dominated by secondary dendrite arm growth from the edge inwards. Comparing thermal results with the bar structure for the UBC experiments showed that the equiaxed zone always corresponded to a classical equiaxed thermal response marked by recalescence (a temporary rise in temperature) while the columnar zone corresponded to a monotonic descent in temperature. Application of a dendrite tip tracking program to the thermal data produced results in agreement with direct estimates of thermal gradient and solidification rate from the raw data. The CET was found to occur within a narrow range of solidification rates and thermal gradients, averaging 0.33 mm/sec and 5.45 °C/cm for

EB remelted AM1, 0.322 mm/sec and 8.36 °C/cm for normal AM1, and 0.38 mm/sec and 5.56 °C/cm for MAR-M200+Hf. No significant difference was found between normal and EB refined AM1. These results are in agreement with the Hunt CET model modified for superalloys by using a pseudo binary approximation for dendrite tip growth kinetics and an average nucleation undercooling of 3.7°C.

TABLE OF CONTENTS

List of Tables

List of Figures

NOMENCLATURE

C_l^*	Liquid Solute Concentration at the Interface (wt%)
C_s^*	Solid Solute Concentration at the Interface (wt%)
C_0	Average Alloy Solute Concentration (wt%)
CET	Columnar to equiaxed Transition
CG	Columnar Grained (turbine blade)
D^l	Diffusion Coefficient in the Liquid State (cm^2/sec)
I	Nucleation Rate (per second per cc)
G	Thermal Gradient, °C/cm
G_A	Free Energy change of Solidification (J)
G_C	Gradient of Solute at the Solid/Liquid Interface (wt%/cm)
G_{LIQ}	Thermal Gradient at the Dendrite Tip
G_{TIP}	Thermal Gradient in the Liquid Ahead of the Solid Front
k	Equilibrium Partition Coefficient
m	Liquidus Slope of a Solute Element (°C/wt%)
N_0	Nucleation Site Density (cc^{-1})
P_C	Solutal Peclet Number (of a Dendrite Tip)
PDAS	Primary Dendrite Arm Spacing (μm)
R	Growth Rate of Solid Front or Dendrite (mm/sec)
SX	Single Crystal (turbine blade)
T_E	Equilibrium Melting Point of the Pure Solid (°C)
ΔT	Undercooling below T_E (°C)

ΔT_C	Solute Induced Undecooling of the Dendrite tip (°C)
ΔT_H	Heterogeneous Nucleation Undercooling (°C) (Turnbull-Vonnegut)
ΔT_N	Heterogeneous Nucleation Undercooling (°C) (Hunt)
ΔT_0	Equilibrium Solidification Interval at Composition C_0 (°C)
ΔT_r	Curvature Induced Undercooling at the Dendrite Tip (°C)
ΔT_t	Thermal Undercooling at the Dendrite Tip (°C)
δ	Percent Lattice Mismatch Between Substrate and Nucleated Solid
σ_{SL}	Solid/Liquid Interfacial Surface Energy (J/m^2)
λ_s	Minimum Unstable Wavelength on a Planar Solid/Liquid Interface (μm)
ρ	Radius of a Dendrite Tip (μm)
Ω	Supersaturation
Γ	Solid/Liquid Interfacial Surface Energy (J/m^2)

ACKNOWLEDGMENTS

I would like to sincerely thank the following people, whose assistance made this work possible:

- my supervisor Dr. Alec Mitchell and co-supervisor Dr. Steve Cockcroft for their guidance and suggestions

- Al Schmalz and Colin Edie for their assistance and very useful suggestions in the lab

- Yves Bienvenu, Remy Tintillier and the others at the SNECMA labs and Ecole des Mines who made my experiments there possible

- Leybold Durferrit in Erlensee for the use of their experimental EBCHR furnace

- my family, for their support, encouragement and understanding

I gratefully acknowledge financial assistance from the University Graduate Fellowship Fund, the Natural Sciences and Engineering Research Council, the ICCS Foreign Government Awards Program (France), and SNECMA.

CHAPTER 1: Introduction

The columnar to equiaxed transition (CET) is a change in the grain structure of a casting from elongated columnar grains oriented parallel to the heat flow, to equiaxed grains with random orientations. The CET may occur in castings ranging from 50 tonne steel ingots to the weld bead in small steel and aluminum GTA welds. Since the physical properties of a casting are dependent on the grain structure, it is useful to study and understand the CET in order to promote its occurrence when beneficial, and prevent it when not. For example, the presence of an equiaxed zone makes continuously cast steel billets less prone to internal cracking[1] and improves the toughness, ductility, strength, fatigue life and resistance to solidification cracking in GTA welds of aluminum alloys[2] and stainless steels[3]. On the other hand, the formation of an equiaxed zone during the VAR and ESR processing of Ni-based superalloys causes unwanted solidification porosity and uneven distribution of oxide inclusions[4]. Of particular relevance to the present study, the presence of even one equiaxed grain constitutes a critical defect in directionally solidified single crystal (SX) or columnar grained (CG) jet engine turbine blades.

Nickel based superalloys such as AM1 and MAR-M200+Hf were designed for use in the casting of SX and CG blades, respectively. These blades operate in the jet engine at high temperatures where the grain boundaries are weaker than the grain matrix. Since stress in service is applied parallel to the blade axis, maximum performance of the blades is only possible with the absence of grain boundaries perpendicular to the blade axis in case

of CG blades, and with the complete absence of grain boundaries in the case of SX blades. As the presence of equiaxed grains in the blade castings (also known as "spurious grains" in the industry) creates such unacceptably oriented grain boundaries, their formation during the casting process constitutes a critical defect leading to the rejection of the blade. The high cost to the aerospace investment casting industry of such rejection has provided the motivation for studying the formation of spurious grains.

When spurious grains occur in turbine blade castings they do so as isolated grains and are usually found in the platform and other extremities of the turbine blade. Figure 1.1 shows a typical turbine blade casting without the ceramic mold. The platform is thin and extends well beyond the main body of the blade; effectively behaving as a cooling fin. As the cooling of this type of casting is accomplished by radiation in a Bridgeman furnace, the ratio of surface area to volume becomes very important in determining the cooling rate of a casting or a section of a casting. Therefore, turbine blade platforms cool more rapidly than the rest of the blade, and will begin to supercool below the liquidus temperature of the alloy before dendrites from the main blade body (oriented dendrites) arrive. This phenomena has been observed in industry[88] with corresponding recalescences in temperature measured in the platform when the oriented dendrites arrive.

The possibility that spurious grains could nucleate and grow in the platform before the arrival of the oriented dendrites has been investigated by Cockcroft et al.[89]. Spurious

grain nucleation was found to depend on the nucleation kinetics of the alloy, the extent of undercooling present in the platform, and the time over which undercooling was present before the arrival of the oriented dendrites. The term "nucleation kinetics" refers collectively to the undercooling required for a given rate of nucleation (measured in number of activated sites per cubic cm) and the number of potential nucleation sites initially present (per cubic cm). Although spurious grains may nucleate on the mould surface itself, this is unlikely as the materials which constitute the face coat are chosen specifically to avoid this. Moreover, the mould surface would provide many sites for nucleation, while the number of spurious grains observed is very few in a given platform. Therefore it is reasonable to assume the nucleation sites responsible for spurious grains generation are contained in the alloy itself.

As Ni-based superalloys destined for turbine blades are vacuum melted using high quality starting materials and must meet strict quality guidelines, the number of potential nucleation sites is low. For this reason, spurious grain nucleation in an undercooled platform may or may not occur, depending on the volume of undercooled liquid and whether or not an active nucleation site is found in this volume. As a result, the generation of spurious grains in turbine blade platforms can only be approached statistically and continues to be a problem in the casting of turbine blades. However, since the nucleation sites responsible for spurious grain nucleation in the platforms are the same as those which would cause a generalized CET, the nucleation kinetics governing the two phenomena are intimately related. It is therefore more reasonable to

study the nucleation kinetics involved in spurious grain nucleation by analyzing a full CET in a bar casting, which can take advantage of a considerably larger volume of supercooled liquid and is therefore more easily reproduced.

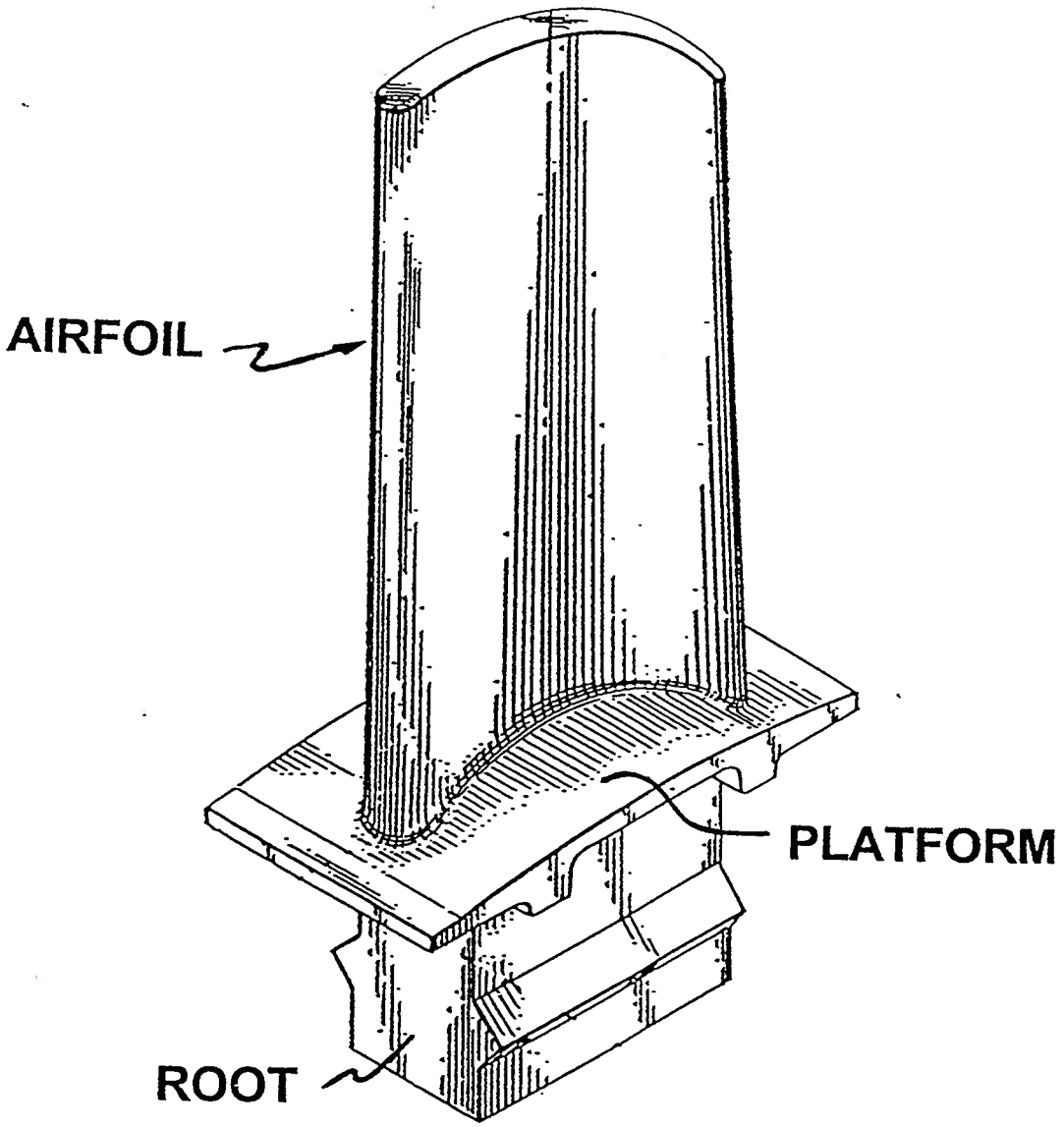

Figure 1.1 Jet Engine Turbine Blade

CHAPTER 2: Literature Review

There is much literature dealing with the CET but it is for the most part theoretical, or qualitative in nature. An extensive review has been conducted by Hunt et al.[5] elsewhere and will not be attempted here. Rather, the trends in the theories and models will be briefly discussed, followed by an evaluation of how they may be applied to a study of the CET in Ni-based superalloys.

The literature on the CET is divided into two categories: that dealing with the origin of the equiaxed grains and that dealing with the competitive growth between equiaxed and columnar grains. Early theories for the CET center on the initial generation of the equiaxed grains via heterogeneous nucleation in the melt, and are still considered as the only explanations for the origin of equiaxed grains. The problem of the competition in growth between the columnar and equiaxed grains has been treated only by recent CET theory because of the complex computer models needed to accurately simulate such a system.

2.1 Early CET Theory: Sources of Equiaxed Grains

As the CET was first observed in large steel castings, the early literature concentrates on the thermal and physical environment present in such castings where the liquid metal is poured into an initially cold mould and allowed to solidify. The first theory for equiaxed grain generation was the "Big Bang" theory by Genders[6] in 1926. According to Genders

the equiaxed grains nucleated immediately after pouring, in a region of liquid adjacent to the mould wall which is thermally supercooled due to large losses of heat to the initially cold mould. In 1935 Papapetrou[7] proposed that fluid flow and the resulting temperature fluctuations in the vertically oriented liquid/solid zone during solidification would remelt dendrite secondary arms, which once detached would act as new grains floating in the liquid. In 1954 Winegard and Chalmers[8] proposed the "constitutional undercooling" theory in which the undercooling of the columnar dendritic front due to solute rejection at the dendrite tips provides sufficient supercooling for the nucleation of the equiaxed grains. Southin[9] proposed in 1967 that the equiaxed grains nucleate during solidification in a region of liquid at the top of the casting, thermally supercooled due to heat losses to the environment. Finally in 1971 Ohno et al.[10] proposed that the equiaxed grains nucleate immediately after pouring on the mould wall itself and are then broken off to float freely in the melt.

The CET literature prior to the arrival of computers and computer modeling is experimental in nature and concentrates on determining the general thermal and physical conditions during casting which either favored or prevented the CET due to a change in one particular source of the equiaxed grains. For example, the presence of convection in the melt was found to favor the CET while using magnetic fields to dampen convection prevented it[11]. Pouring with low melt super heats[11] and into colder moulds[12] were found to favor the CET, as was using alloys which grew at larger constitutional undercoolings[13]

and adding innoculants to enhance heterogeneous nucleation[14]. Mechanical vibration was also found to extend the equiaxed zone and promote grain refinement[15].

Experimental evidence has proven difficult for researchers to rationalize in terms of the operation of a single source of equiaxed grains since a change in casting parameters would affect some or all of the possible sources simultaneously. It also became clear that, beyond the initial generation of equiaxed grains, certain conditions were required in the melt to allow them to grow and block the advancing columnar grains. Hence more significance was given to the competition in growth between equiaxed and columnar grains. As a result, theoretical work on the CET turned towards modeling of the growth of equiaxed and columnar grains and the nucleation kinetics governing heterogeneous nucleation. This required knowledge of the relationship between dendrite growth rates, undercooling at the tip, and the undercooling at which heterogeneous nucleation occurs. Both of these quantities are generally unknown and extremely difficult to determine experimentally. Hence modeling and understanding the CET requires a fundamental approach to dendrite tip growth and nucleation kinetics.

2.2 Fundamentals of the CET

Recent theory and experiments on nucleation kinetics and dendritic growth have allowed a better understanding of the conditions leading to the CET. Heterogeneous nucleation of the equiaxed grains is necessary for a transition to occur, and regardless of the source

of nucleation, the equiaxed grains can only grow in an undercooled liquid. This places great importance on knowing the undercooling of the tip of a dendrite.

2.2.1 Nucleation Kinetics

The rate of nucleation per unit volume in liquid metals has been given by Chalmers[16] as

$$I = \frac{nkT}{h} \cdot \exp\left(-\frac{G_A}{kT}\right) \cdot \exp\left(-\frac{16\pi\sigma_{SL}^3 T_E^2}{3L^2(\Delta T)^2 kT}\right) \qquad (1)$$

where

n = the number of atoms per unit volume of liquid

k = Boltzman's constant

G_A = free energy change of solidification

σ_{SL} = solid/liquid interfacial surface energy

L = free energy of vaporization

T_E = equilibrium melting point of the pure solid

T = temperature

ΔT = supercooling below T_E

The most important feature of equation (1) is that the nucleation rate increases rapidly as the supercooling surpasses a critical quantity defined as the supercooling of nucleation. Nucleation rate is therefore less meaningful than "nucleation temperature" at which all nuclei become active simultaneously. Equation (1) was written for the case of

homogeneous nucleation. It is assumed that heterogeneous nucleation is responsible for the generation of equiaxed grains in the CET as homogeneous nucleation in Ni requires several hundred degrees undercooling[17] which is not normally found in the commercial processes of interest. The presence of a foreign substrate upon which the growth of solid may start changes the free energy balance in equation (1) by a factor of f(θ) given by the following equation:

$$f(\theta) = \frac{(2+\cos\theta)(1-\cos\theta)^2}{4} \qquad (2)$$

where θ is the angle which the critical solid nucleus makes with the foreign substrate. The resulting changes in the rightmost exponential term of equation (1) can reduce the supercooling of nucleation to a fraction of a degree C. The value for θ may be found directly with a free energy balance using the liquid/substrate, liquid/solid and solid/substrate interfacial surface energies. However, these quantities are generally unknown and are extremely difficult to determine experimentally. As a result, the literature on heterogeneous nucleation includes numerous works which attempt to correlate the nucleation substrate, solidifying materials and undercooling of nucleation[18,19] using simpler mechanisms such as lattice mismatch or electrostatic potential. The literature also concentrates on the more easily studied low temperature melting metals such as Sn.

However, experiments with liquid iron, similar in melting point to Ni, have shown that at these temperatures (1550°C) the Turnbull-Vonnegut lattice disregistry theory[17] is a good

predictor of the undercooling necessary for heterogeneous nucleation. The Turnbull-Vonnegut theory links the lattice mismatch between the foreign substrate and newly forming solid of similar crystallographic structure to nucleation undercooling by:

$$\Delta T_H = 0.556\frac{\delta^2}{8} \qquad (3)$$

where

ΔT_H = nucleation undercooling (°C)

δ = percent lattice mismatch between substrate and nucleated solid

Equation (3) is based on a simple elastic strain model which is valid up to approximately 20% disregistry. Bramfitt[20] modified the equation to include dissimilar crystal structures evaluated for their planar disregistry in inter-atomic spacings. Bramfitt[20] and Ohashi et al.[21] measured the undercoolings before nucleation on a number of nitrides, carbides and oxides in Fe. Findings were in agreement with Bramfitt's version of Turnbull-Vonnegut equation and are shown in Figure 2.1.

2.2.2 Extension of Nucleation Theory to Multiconstituent Alloys

Equation (1) was written assuming that only one type of atom was present in the liquid, as was the modification to heterogeneous nucleation. However, experiments with Fe-Ni alloys[22,23], Sn-Bi alloys[24] and Cu-Ni alloys[25] have shown that heterogeneous nucleation always occurs at a constant undercooling below the liquidus temperature of an alloy in

the same system, provided that the alloy solidifies with the same crystal structure. Extending this to Ni-based superalloys which always precipitate FCC solid, if the same foreign substrate is responsible for heterogeneous nucleation in all superalloys, it will become active at the same undercooling below the liquidus for each alloy.

2.2.3 Dendrite Tip Growth Kinetics

The growth of dendrites is controlled by events at the dendrite tip such as the diffusion of heat and solute. Dendrite tips grow at a temperature less than the equilibrium liquidus temperature of the alloy as a result of several contributions. The undercooling with respect to the liquidus of the alloy is given as[26]:

$$\Delta T = \Delta T_C + \Delta T_t + \Delta T_r \qquad (4)$$

where

ΔT_C = solute induced undercooling

ΔT_t = thermal undercooling

ΔT_r = undercooling due to tip curvature

Under normal industrial conditions of growth in metallic alloys the thermal undercooling and curvature undercooling are very small compared to the solutal undercooling. Solutal undercooling occurs due to the fact that as alloys solidify they reject solute into the liquid (with some exceptions) at the liquid/solid interface according to the partition coefficient of the equilibrium phase diagram:

$$C_s^* = kC_l^* \tag{5}$$

where

C_l^* = liquid solute concentration at the interface

C_s^* = solid solute concentration at the interface

k = partition coefficient on the equilibrium phase diagram

Since the mass diffusivity is usually three orders of magnitude smaller than thermal diffusivity in metallic alloys, mass diffusion is the growth limiting factor. Therefore solute accumulates at the solid/liquid interface in a diffusion boundary layer, effectively raising the solute content of the liquid immediately ahead of the dendrite. This accumulation of solute induces a corresponding "supersaturation" of solute in the solid dendrite tip, above that which is expected to result from equilibrium solidification conditions. The supersaturation is denoted by Ω and defined as:

$$\Omega = \frac{\left(C_l^* - C_0\right)}{\left(C_l^* - C_s^*\right)} \tag{6}$$

where

C_0 = solute concentration of the alloy far from the interface

Figure 2.2 shows the thermal and solutal fields around the tip of a dendrite growing under constrained thermal conditions. The accumulation of solute is shown in the upper most frame, while the lower frames illustrate how this may be translated into a

supercooling below the alloy equilibrium liquidus temperature. The solute diffusion field in front of the dendrite tip also creates a variation in the local liquidus temperature of the alloy, as shown by the T_L line in Figure 2.2. As the diffusion field is limited to a small distance ahead of the advancing dendrites, the equilibrium liquidus temperature soon reaches that of the alloy. The local rise in temperature due to the thermal gradient is often less than the local rise in liquidus temperature. Hence a region may be created where the local temperature is less than the local liquidus temperature. This is known as constitutional undercooling and provides the possibility for undercooling to exist (and hence heterogeneous nucleation) in the presence of positive thermal gradients ahead of an advancing front. The undercooling of the dendrite tip is related to the supersaturation through

$$\Delta T_C = mC_0\left(1-\frac{1}{1-\Omega(1-k)}\right) \tag{7}$$

where

m = slope of the liquidus (°C/wt% solute)

Ivanstov first calculated the diffusion field ahead of the dendrite tip at steady state[27], assuming that it is a parabola of revolution, in terms of the supersaturation:

$$\Omega = I(P_C) = P_C \cdot \exp(P_C) \cdot E_1(P_C) = P_C \cdot \exp(P_C) \cdot \int_{P_C}^{\infty} \frac{\exp(-z)}{z} dz \tag{8}$$

I(Pc) is the Ivanstov function of P_C, the solutal Peclet number, given by

$$P_C = \frac{R\rho}{2D^l} \tag{9}$$

where

R = rate of advance of the dendrite tip

ρ = radius of the dendrite tip

D^l = liquid diffusion coefficient

The solutal Peclet number may be viewed as the ratio of the dendrite tip radius to the effective diffusion boundary layer which is defined as $R/2D^l$.

2.2.4 Dendrite Tip Undercooling

In order to determine the dendrite tip undercooling as a function of growth conditions, the supersaturation must be calculated. The analysis of Ivanstov relates the supersaturation of the growing dendrite tip to both ρ and R, but does not permit a unique solution to equation (8) given the available thermal growth conditions. In order to specify a unique solution, Zener[28] proposed the "extremum" theory in which the dendrite tip grows at the maximum velocity for a given supercooling. However, the theory was in poor agreement with the experiments of Glicksman et al.[29]. Much better agreement was found with the "marginal stability" theory of Langer and Muller-Krumbhaar[30,31,32] in which the dendrite grows with a tip radius corresponding to the smallest sinusoidal wavelength λ_s which constitutes an unstable perturbation on a planar solid/liquid interface. The perturbation analysis of Mullins and Sekerka[33] gives:

$$\lambda_s = \rho = 2\pi\sqrt{\frac{\Gamma \cdot D^l}{R \cdot k \cdot \Delta T_0}} = 2\pi\sqrt{\frac{\Gamma}{m \cdot \xi \cdot G_C - G}} \tag{10}$$

where

Γ = solid/liquid interfacial surface energy

G_C = gradient of solute at the solid/liquid interface (wt%/cm)

ΔT_0 = equilibrium solidification interval at the composition C_0

The second expression for λ_s is defined by an analysis by Kurz, Giovanni and Trivedi in their "KGT" model of dendrite tip growth[34], with ξ given by:

$$\xi = 1 - \frac{2k}{\left(1 + \frac{1}{\sigma^* P_C}\right) - 1 + 2k} \tag{11}$$

where σ^* is defined as a constant of approximately 0.025[35,36] which varies slightly according to alloy system[37] . Kurz et al. also evaluated the solute gradient at the dendrite tip using a flux balance from Ivanstov's solution:

$$G_C = \frac{R \cdot C_l^* \cdot (k-1)}{D^l} \tag{12}$$

Substituting the expression for G_C into the last expression in equation (10) and employing the definition of the Peclet number gives a quadratic equation in the growth rate R:

$$R^2 A + RB + C = 0 \tag{13}$$

where

$$A = \frac{\pi^2 \Gamma}{P_C^2 D_l^2} \tag{14}$$

$$B = \frac{mC_0(1-k)\xi_s}{D_l\left[1-(1-k)I(P_C)\right]} \tag{15}$$

$$C = G \tag{16}$$

Equation (13) may then be iteratively solved to find the unique tip radius corresponding to a specified growth rate. Finally, the supersaturation as a function of tip radius is known, and may be used to find the undercooling of the dendrite tip. Several such formulations relating growth conditions to undercooling have been made, with similar results. Hunt developed a comparable but simplified expression for dendrite growth which predicts tip undercoolings similar to the above expressions over a limited range of solidification conditions. Hunt verified his theory by directly measuring the dendrite tip temperatures in Al-Cu alloys[38], and found good agreement between theory and experimental results. In addition, Lacaze et al.[90] found good agreement between calculations based on an earlier formulation by Trivedi and their experimentally determined tip undercoolings in Ni-7.2%Al-6.4wt%Ta.

2.2.5 Extension of Dendrite Tip Growth Theory to Multiconstituent Alloys

The theories for dendrite tip growth presented so far are only valid for binary alloys. Coates et al.[39] showed that the perturbation analysis of Mullins and Sekerka for planar

interfaces could be mathematically extended to include ternary and multi-constituent alloys provided that there were no interdiffusional effects of the overlapping solute fields of the different solute elements, and that the correct partition coefficients were used. In effect, each solute element makes a separate and independent contribution to the constitutional supercooling of the interface. Bobadilla et al.[40] and Rappaz et al.[41] extended the theory to the growth of dendrites, in which the expression for dendrite tip radius in equation (10) is modified to:

$$\rho = 2\pi \sqrt{\frac{\Gamma}{\sum_i \left(m_i \cdot G_{c,i} \cdot \xi_i\right) - G}} \tag{17}$$

The individual undercoolings of each solute element *i* may be summed to determine the overall undercooling of the dendrite tip:

$$\Delta T_C = \sum_i \Delta T_{c,i} = \sum_i \frac{m_i \cdot C_{0,i}}{1 - \left(1 - k_i\right) \cdot I(P_{c,i})} \tag{18}$$

Solution to the quadratic equation (13) is then carried out for each solute element. Further simplification to the calculation may be made by assuming that each solute element has the same liquid diffusion coefficient D_l which means that their Peclet numbers and supersaturations are equal. Therefore the expression for supercooling simplifies to

$$\Delta T_C = \Omega \cdot \sum_i m_i \cdot C_{l,i}^* \cdot \left(1 - k_i\right) = \Omega \cdot \overline{m} \cdot \overline{c} \cdot \left(1 - \overline{k}\right. \tag{19}$$

for which the "pseudo-binary" variables are

$$\bar{C} = \sum_i C_{l,i}^* \qquad \bar{m} = \frac{\sum_i m_i \cdot C_{l,i}^*}{\bar{c}} \qquad \bar{k} = \frac{\sum_i m_i \cdot C_{l,i}^* \cdot k_i}{\bar{m} \cdot \bar{c}} \tag{20}$$

Therefore the dendrite tip undercooling for a multiconstituent alloy may be approximated given the growth rate.

2.3 Mathematical Modeling of the CET

Recent work has focused on incorporating nucleation theory and dendrite growth theory into models which attempt to quantitatively predict the position of the CET in a casting. Simple models based on empirical equations were developed by Witzke and Durand[42], Fredrickson et al.[43], Lipton et al.[44] and Hunt[45]. The Hunt model is a special case as the analysis of the CET was reduced to a simple analytical expression. Finite difference models were developed by Flood and Hunt[46,47], and Witzke et al.[48], and a 3-D finite element model was developed by Pardo et al.[3]. More advanced models based on the Monte-Carlo technique have been recently developed by Brown and Spittle[49], Zhu and Smith[50], and Rappaz[51] which track the growth of individual columnar and equiaxed grains. Finally, Wang and Beckermann[52] have developed a multi-phase approach incorporating a finite difference heat and mass transfer model. Most of the models incorporate heat flow, fluid flow and an equation relating constitutional undercooling of the columnar front to growth rate. Heterogenous nucleation is addressed only in the

Rappaz and Hunt models, while the equiaxed grains are considered to be pre-nucleated at the liquidus temperature in all other models.

2.3.1 Criteria for the CET

There is general agreement among modelers that the CET occurs when the volume fraction of equiaxed grains ahead of the columnar front reaches 49%. However, the ultimate goal of every model is to attribute the occurrence of the CET to some critical solidification factor such as thermal gradient or solidification rate. In the Hunt model, the CET occurs below a critical thermal gradient. Witzke related the occurrence of the CET to a critical undercooling of the columnar front. Lipton's criteria was a critical undercooling and volume of undercooled fluid at the liquid/solid interface, and thermal recalescence in the equiaxed zone. Pardo attributed the CET to a critical solidification rate accompanied by low thermal gradients and the presence of effective heterogeneous nuclei[3].

2.3.2 Systems Studied for CET Model Validation

Validation of the CET models has been imprecise. Fredriksson et al.[43] validated their model with a single thermocouple in the center of a large steel ingot while Lipton et al.[44] used multiple thermal measurements in solidifying succinonitrile-borneal. Pardo[3] compared his FEM results to the observed grain structure in TGA welds in austenitic and ferritic stainless steels. Rappaz[51] compared his model results to the grain structure in

small Al-Si alloy castings. Witzke et al.[48] compared their model to physical observations made during casting of ammonium chloride/water, Fe-0.05%C and Al-4.6%Cu alloys. Hunt[45], and Flood and Hunt[46,47], never validated their models with experiments. Weinberg used the Hunt analytical model to analyze his thermal data on Sn-Pb alloys[53] and Al-3%Cu alloys[54] and determined that the CET occurs at a critical thermal gradient and within a narrow range of solidification rates for these alloys. Wang and Beckermann[52] used the experiments of Weinberg as their validation, with limited success. Spittle and Tadayon[55] also applied their simple heat transfer model to the Weinberg results[53,54] and found no agreement between their results. Furthermore, Spittle and Tadayon concluded that it is beyond present ability to predict the CET based on a solidification parameter which could be determined in a simple model. All other models rely on comparison to the macrostructure of a casting with no thermal measurements. The models for which the heterogenous nucleation undercooling is 0°C predict a duplex equiaxed/columnar structure near the CET as the volume fraction of equiaxed grains ahead of the columnar interface approaches 0.49. However this is not seen in practice[5], as the transition is sharp with no mixing of columnar and equiaxed grains.

2.4 The CET in Ni-Based Superalloys

There is very little in the CET literature to apply towards a study of Ni based superalloys, as no model was validated with superalloy castings and no CET experiments have been done on superalloys with the notable exception of Pollock et al.[56]. Pollock established a thermosolutal convection criterion for the CET in the Ni based superalloys studied.

However, another more traditional criterion held in superalloy literature is based on the ratio of G/R at the liquid/solid front.

2.4.1 The Thermosolutal Convection Criterion

Pollock et al. conducted experiments on single crystal castings of specially formulated Ni-based superalloys containing high amounts of refractory elements such as W and Re. These elements segregate strongly to the solid during solidification, and because they are denser than the alloy, leave the depleted interdendritic liquid significantly less dense than the liquid alloy above. The resulting difference in densities leaves the interdendritic liquid susceptible to buoyancy driven flow upwards, as in the generation of freckles[66]. It is known that such buoyancy driven flows are favored by wide interdendritic spacings which offer less resistance to fluid flow.

Pollock et al. found that at low gradients and slow solidification rates the dendritic array underwent a morphological transition to a widely spaced structure dominated by secondary and tertiary growth, and this transition favored the convective instabilities leading to freckling and a generalized CET. The phenomena was observed to begin at a critical primary dendrite arm spacing (PDAS) of 320 microns, with the random nucleation of isolated mis-oriented columnar grains. At a PDAS of 600μm or greater, a generalized CET was observed to occur. The breakdown of the columnar structure was also observed to occur more quickly with larger additions of W and/or Re, lending support to the thermosolutal convection theory. As the generalized CET was usually

preceded by the isolated nucleation of columnar grains, a zone of mixed columnar and equiaxed grains (or mixed columnar and misoriented columnar grains) was usually found between the equiaxed zone and the single crystal columnar zone.

2.4.2 The G/R Criterion

The more popular view in the investment casting literature concerning the CET in superalloys is that it occurs at a critical value of G/R, although no experiment has ever validated this theory. Representative of this is McLean's well known plot[57] of the solid/liquid interfacial morphology of common industrial superalloys as a function of G and R shown in Figure 2.3. Similar plots are also given in the literature by Quested and McLean[58], Kurz and Fisher[26], Sahm and Schubert[59], and Ma et al.[60]. Moreover, the aerospace investment casting industry often publishes "defect maps"[61] based on graphs of G and R similar to McLean's, in which the probability of equiaxed grain formation is shown to increase as G/R decreases. Figure 2.3 shows that as the ratio G/R at the solid/liquid interface decreases the interfacial structure changes from planar to cellular to columnar dendritic and finally to equiaxed dendritic, with each region of stability separated by a line of constant G/R.

The ratio G/R is taken to be indicative of the amount of undercooling of the solidification front relative to the alloy liquidus temperature. However, this is only valid for a planar interface as the G/R criterion was developed uniquely for the transition of a planar interface to a cellular interface. Chalmers et al.[62] showed that the planar interface

becomes unstable when the thermal gradient at the interface is exceeded by the gradient in liquidus temperature resulting from the build up of solute as at the tip of a dendrite. Chalmers determined the critical G/R ratio preceding a breakdown to cellular structure to be:

$$\frac{G}{R} \geq -\frac{m_L C_0 (1-k)}{k D_L} \tag{21}$$

Experiments with Ni based superalloys by Tien and Gamble[63], and Bhambri[64] have shown that these alloys may be grown with a planar interface only when the constitutional supercooling criteria is met. Calculations confirmed that the experimentally measured values of G and R_I corresponded to the accepted values of D_L[65]. Equation (21) is the only expression for a morphological transition during solidification that has been mathematically formulated and verified through experimentation. Further transitions are described by Flemings[65] to occur as G/R decreases, however none have been mathematically formulated or verified. The morphology of the solid/liquid interface in the commercial processes of interest is always dendritic. Therefore, a more accurate expression to represent the undercooling of the interface preceding a CET would be equation (7) which was developed for the tip of a dendrite.

Further proponents of the G/R criterion are Copley et al.[66], but for reasons other than the supercooling at the solid front. Copley et al. proposed that the CET would occur at a critical value of G/R given by

$$\frac{G_S}{R} = \frac{\Delta H}{k_T} \tag{22}$$

where

G_S = thermal gradient at the solidus temperature

R = growth rate of the dendrite tips

ΔH = latent heat of solidification

k_T = thermal conductivity

In effect, equation (22) defines the minimum thermal gradient at the solidus temperature which is required to conduct away the latent heat released in the solidifying mushy zone growing at R. Theoretically, directional solidification breaks down when the minimum gradient is not maintained. However no mechanism is proposed for the development of the equiaxed grains in either G/R based criteria for the CET. Therefore, analyzing the CET in superalloys in order to quantify the nucleation kinetics involved requires a study of the fundamental mechanisms at work. Moreover, these mechanisms must be incorporated into a model which can predict nucleation kinetics based on experimental data.

2.5 Application of CET Theory and Models to Superalloys

The best suited model to apply to Ni based superalloys is the general steady state analytical model of Hunt[45]. The Hunt model is based on a steady state analysis of columnar and equiaxed growth. Hence, thermal gradients in the system are constant,

which greatly simplifies the mathematics involved. In addition, the Hunt model considers heterogeneous nucleation in the constitutionally undercooled liquid at the columnar front to be the only source for equiaxed grains. Hunt's model is extremely attractive because the competition in growth between columnar grains and equiaxed grains, and heterogeneous nucleation at a specified undercooling are all combined into one simple expression. Moreover, Hunt and Flood constructed a one-dimensional and also a 2-dimensional (cylindrical) finite difference heat transfer model including convection in the bulk liquid and heat release from the equiaxed grains and obtained results almost identical to the simple analytical model for Al-3%Cu alloys[46]. The analytical model simplifies to a statement of the critical thermal gradient in the liquid ahead of the columnar dendrites below which a full columnar to equiaxed transition will occur:

$$G < 0.617 N_0^{1/3} \left\{ 1 - \frac{(\Delta T_N)^3}{(\Delta T_C)^3} \right\} \Delta T_C \qquad (23)$$

where

G= critical thermal gradient at the liquid/solid interface below which the CET occurs

N_0= nucleation site density (cc^{-1})

ΔT_C= columnar dendrite tip undercooling

ΔT_N= heterogenous nucleation undercooling at which one site per cc per second becomes active

Equation (23) results from assuming that the CET occurs once the volume fraction of equiaxed grains ahead of the columnar dendrites reaches 0.49. At volume fractions less than 0.49 and greater than 0.01, a dual columnar and equiaxed structure is predicted. Although written in terms of G, equation (23) may also become solidification rate (R) dependent and gradient independent as the R term is hidden in the expression for the undercooling of the dendrite tip ΔT_C. Hunt emphasized that thermal gradient and solidification rate played two separate roles governing the CET while the nature of the system (ΔT_N, ΔT_C, N_0) determines which of the two dominates as the critical factor. In addition, both factors taken together as G·R (cooling rate) play an important role controlling CET behavior.

The cooling rate during solidification determines the amount of time that the equiaxed grains have to grow before the arrival of the columnar front. If the equiaxed grains have not grown to a volume fraction of 0.49 by this time, a CET will not occur. Therefore low cooling rates favor a CET as they maximize the time allowed for equiaxed growth. Likewise, large numbers of nucleation sites favor a CET, as they minimize the growth time required to produce a volume fraction of 0.49. The rate of solidification determines the undercooling of the dendrite tips (via Equation (19)), which may or may not be sufficient to allow heterogeneous nucleation in the liquid ahead of the advancing solid front. Therefore the CET is favored by high solidification rates which maximize front undercooling. The role of the thermal gradient is to provide a finite volume of constitutionally undercooled liquid ahead of the solid front in which active nucleation

sites may be found. Therefore the CET is favored by low thermal gradients which maximize the volume of undercooled liquid.

The Hunt model may be used to analyze experimental results only if the assumptions upon which the model are based accurately reflect the conditions present during the experiments. Therefore, thermal gradients in the liquid ahead of the columnar front should be constant and heterogeneous nucleation in the constitutionally undercooled region at the solid front must be the only source of equiaxed grains. Once these criteria are met, the Hunt model may be used calculate the nucleation undercooling in Ni-based superalloys. Referring to Equation (23), if values of N_0, G and ΔT_C are supplied, the undercooling of heterogeneous nucleation is automatically calculated. The population of nucleation sites (N_0) may be inferred by counting the equiaxed grains in the equiaxed zone and finding their average size. The gradient at the columnar front (G) and the growth rate immediately prior to the CET may be experimentally measured. Dendrite tip undercooling (ΔT_C) may be estimated from the measured growth rates by applying the KGT formulation modified with the pseudo binary approximation for multiconstituent Ni-based superalloys. This constitutes a modification to the original Hunt formulation for dendrite tip undercooling, which is only valid for binary alloys. Therefore the Hunt model will be referred to as the "modified" Hunt model. In addition, it would be very useful to link the resulting ΔT_N to some particular material present in the alloy. This requires the application of heterogeneous nucleation theory to materials likely to be

found in the liquid alloy. The precedents in the literature for this, and application of the KGT model to dendrite tip growth in superalloys will be reviewed.

2.5.1 Application of Heterogeneous Nucleation Theory to Superalloys

The source of heterogeneous nucleation and the nucleation undercooling in Ni-based superalloys are unknown, although they are of central importance to the CET and the generation of spurious grains in castings. For the casting of SX and DC blades, the Ni based superalloys are cast at about 1500°C into molds pre-heated to the same temperature. As the liquidus of these alloys is generally below 1400°C, the resulting superheat prior to solidification eliminates the possibility of the presence of equiaxed grains resulting from mechanisms which depend on a cold mold wall. The filled molds are then withdrawn into a lower, cold chamber while a strong positive thermal gradient is held at the solid/liquid interface throughout the casting process. During this process, as they are drawn into the cold zone the platforms have been observed to supercool by several °C[88] before the arrival of oriented dendrites from the main blade body. It is therefore reasonable to assume that the source of equiaxed grains in the platform is foreign solid material (inclusions) in the alloy, rather than remelted dendrite arms.

Few materials are stable at the casting temperatures of superalloys. Investigations of superalloys with EB button melting have shown that oxides and nitrides are present[67] and one in particular showed the presence of Al_2O_3, $Ca_3Al_2O_6$, $Al_2MgCa_3O_7$ and $MgAl_2O_4$ in the Ni based superalloy Rene 95[68]. Others have shown the presence of TiN at high

temperatures in liquid superalloys[69,70]. The molds used to cast turbine blades are generally made of Al_2O_3 and SiO_2 and possibly other oxides[71] bound with water glass. The mould may play a significant role in nucleation in Ni-based superalloys as Lux et al.[72] showed that using $ZrSiO_4$ bound with water glass as the mould face coat allowed undercoolings of up to 191°C to be reached in commercial MAR-M200 before nucleation, whereas no undercooling was apparent with an Al_2O_3 based facecoat.

Determining which of the materials present in liquid superalloys act as sources for equiaxed grain nucleation would be a major step towards avoiding spurious grains in castings. Various workers have investigated the grain refining effects of some additions on superalloys. Lamberigts et al.[73] found that small castings into cold molds of revert IN 100 high in [N] and [O] were equiaxed while those cast from low [N] and [O] were columnar in structure. Lamberigts found that the revert alloy contained high amounts of TiN particles. Painter et al.[74] found that CrN and TiN added to IN100 were effective grain refiners in equiaxed castings. Chechenstev et al.[75] reported the practice in Russian superalloy foundries of using added ZrN powder as an effective grain refiner in equiaxed castings of Ni based alloy Zh56K. Small ingot casting experiments on IN738LC by Liu et al.[76] found that additions of boron, NiAl and NbC favored the CET by increasing the size of the equiaxed zone and decreasing grain size. The above experiments were all performed on castings poured into cold molds, resulting in high solidification rates and therefore high undercoolings of the solidification front. Whether the same additions

would be effective grain nucleation sites under the slower growth rates of directional solidification is unknown, as is the undercooling at which they become active.

Following Bramfitt and Ohashi, a calculation may be made of the undercooling of potential nucleation sites in Ni based superalloys based on lattice disregistry. A correlation between nucleation undercooling and effectiveness in provoking a CET has already been established. Pardo found that a CET would occur in ferritic stainless steel GTA welds only in the presence of TiN particles[3], which were found to be the most effective nucleating agent by Bramfitt, becoming active at 1.7°C undercooling. Moreover, steels of similar composition but austenitic in structure showed no CET despite the presence of TiN. A calculation of the lattice misfit between TiN and austenitic structure at high temperature shows a much greater undercooling is expected before nucleation occurs. Fredholm[77] developed a system of coefficients relating the concentration of alloying elements in Ni based superalloys to the lattice parameter. Calculations show that there is very little difference from alloy to alloy, the average of AM1 and MAR-M-200+Hf at their liquidus temperatures being a_0=3.66 Å. Following Bramfitt's method of rotating the lattices by 45° to obtain a better fit, the undercoolings of several refractory materials have been calculated with the results given in Table 2.1. Note that $MgAl_2O_4$ consists of an FCC superlattice with oxygen atoms lying on the sites of an FCC lattice with a parameter equal to half that of the superlattice. Table 2.1 shows that the most effective substrates of those examined are ZrN and $MgAl_2O_4$, which are predicted to nucleate at 7.6°C undercooling. These undercoolings serve as an

approximation only, but are useful in determining which materials are the more likely nucleation sites in Ni based superalloys.

2.5.2 Application of Dendrite Tip Growth Theory to Ni-Based Superalloys

The accuracy of using the pseudo binary approach to calculating the dendrite tip undercooling in alloys is dependent on using the correct values of the liquidus slopes m_i, and partition coefficients k_i for each element *i* in the alloys (ie. not from the binary phase diagrams). The correct partition coefficients are available for AM1[78] and MAR-M200+Hf[79] from planar front solidification experiments. Table 2.2 shows the values of the partition coefficients for the two alloys, as well as those taken from binary alloy phase diagrams for comparison. For Hf, only the value from the binary phase diagram is available, and is used as an approximation. In addition, liquidus slopes of various elements in Ni alloys are available from solidification studies by Willemin[80] and Cook and Guthrie[81] and are given in Table 2.3. These values were used in a calculation of dendrite tip undercooling and chemical supersaturation in the growth of AM1 dendrites by Siredey[82]. Direct WDX microprobe measurements of the chemical supersaturations at the dendrite cores compared well to calculated values.

Also required for the calculation of dendrite tip undercooling are the diffusion coefficient of solute elements in the liquid (D^l) and the Gibbs-Thompson coefficient(Γ). D^l has been reported[83] as $3.6 \cdot 10^{-5}$ cm^2/sec in a Ni-19.7 wt % Cr alloy at 1600°C. This value was already used in the pseudo binary modeling of equiaxed dendritic growth in Ni based

superalloy GTD-111[84]. The Gibbs-Thompson coefficient is available only as a approximation in the literature[57], and is taken as $2 \cdot 10^{-5}$ K/cm as used by Chehaibou[78] and Siredey[82] in their studies of AM1.

2.6 Summary

Determining the nature of the CET and gaining the ability to predict its occurrence have been the subject of many studies and models throughout the literature. However, despite the relative abundance of CET models available, there are no reports of systematic experimental thermal data on the CET apart from the low temperature Al-3%Cu and Pb-Sn alloys studied by Weinberg[53,54]. Weinberg found reasonable agreement between the Hunt analytical CET model and his results with Al-3%Cu. Moreover, the Hunt CET model offers a simple yet complete analysis of the CET in terms of the thermal gradient at the solid interface, growth rate and nucleation kinetics. Therefore, it will be used for the present determination of nucleation kinetics in AM1, EB refined AM1 and MAR-M200+Hf. The Hunt model may be applied to Ni-based superalloys by modifying the dendrite tip undercooling expression with the pseudo binary approximation of the KGT formulation. However, application of the Hunt model to experimental results is valid only if the unique source of equiaxed grains is nucleation in the constitutionally undercooled zone. The source of equiaxed grains leading to a CET in superalloys is unknown. Pollock et al.[56] have established that thermosolutal convection and dendrite arm remelting play a critical role as a source of equiaxed grains in their refractory element-rich alloys. Experimental evidence has also shown that the addition of TiN,

ZrN, NbC and NiAl favors the CET or leads to smaller equiaxed grains in typical equiaxed superalloy castings with high cooling rates. Therefore it would seem likely that heterogeneous nucleation plays an important role in the CET in superalloys. The present study will therefore provide knowledge of the nucleation kinetics of superalloys as well as contributing to the general understanding of the CET and providing systematic thermal data for the systems studied.

Table 2.1: Prediction of Undercooling of Nucleation in Ni-Based Superalloys of Several Refractory Materials by the Turnbull-Vonnegut Theory

Substrate	Lattice Parameter at 1360°C (Å)	% Lattice Mismatch With Ni-Based Superalloy	Undercooling of Nucleation in Ni Based Superalloy (°C)
MgO	4.295	16.9	19.8
TiN	4.308	16.7	19.3
NbC	4.511	12.7	11.3
ZrN	4.628	10.5	7.6
$MgAl_2O_4$	8.075	10.5	7.6

TABLE 2.2: Partition Coefficients of Alloying Elements in MAR-M200+Hf and AM1

Element	Partition Coefficient in Binary Alloy[93]	Partition Coefficient in MAR-M200+Hf[79]	Partition Coefficient in AM1[78]
Ta	0.97	----	0.76
Al	0.83	0.91	0.91
W	1.60	1.1	1.38
Mo	0.57	----	0.78
Cr	0.92	0.9	0.92
Co	1.10	1.1	1.09
Ti	0.89	0.69	0.58
Hf*	0.17	----	----

TABLE 2.3: Liquidus Slopes of Alloying Elements in MAR-M200+Hf and AM1

Elements	Liquidus Slope in System Ni-Al-Ta[78] (°C/wt%)	Liquidus Slope in System (Ni-Co-Cr-Al-W-Ti)[80] (°C/wt%)	Liquidus Slope in System IN-100[81] (°C/wt%)
Ta	-5	--	--
Al	-13	-15	--
W	--	0.8	--
Mo	--	--	-4.8
Cr	--	--	-3.0
Co	--	--	0.7
Ti	--	-16	--

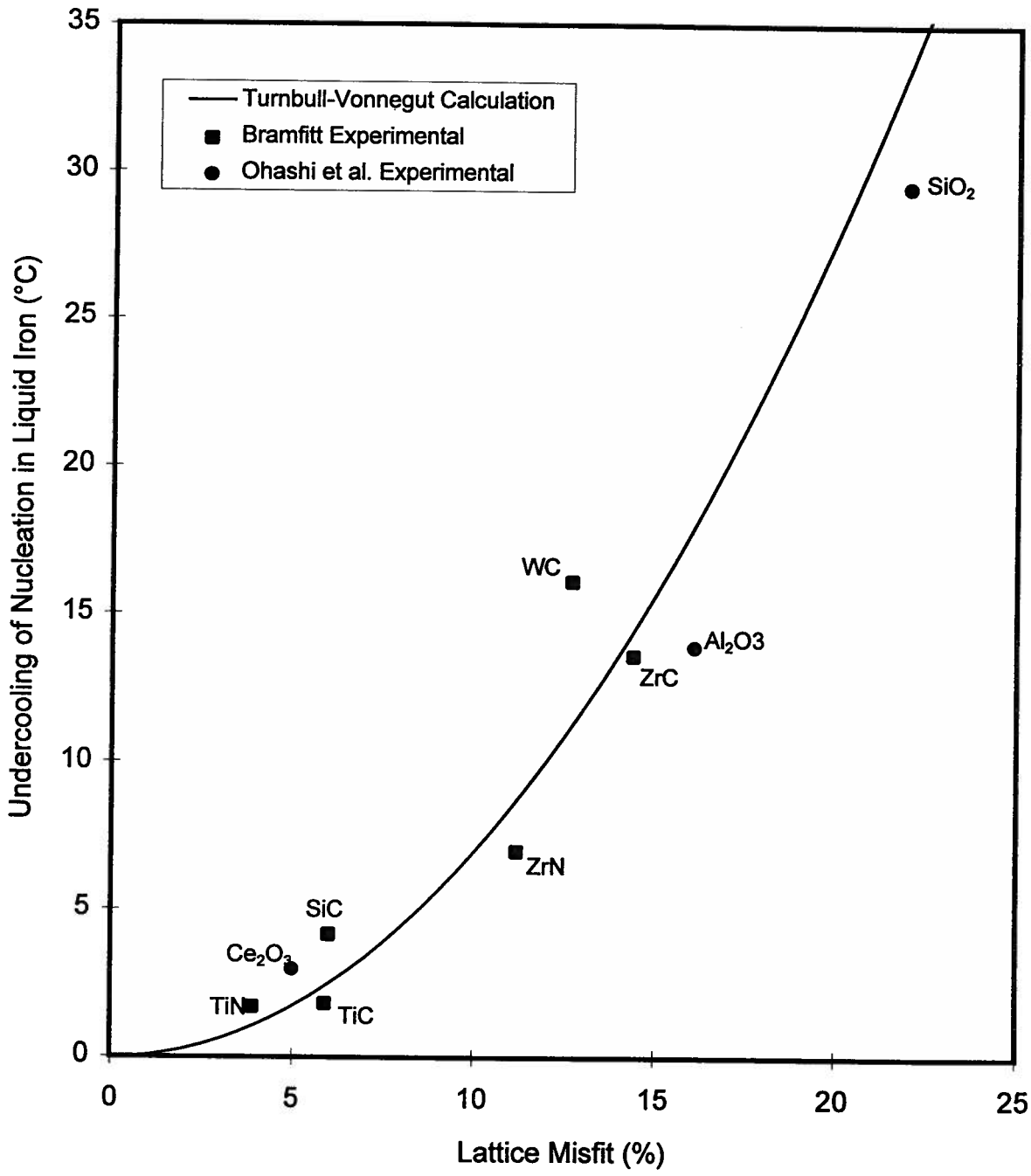

Figure 2.1:
Lattice Misfit vs. Nucleation Undercooling in Fe
of Various Oxides, Nitrides and Carbides

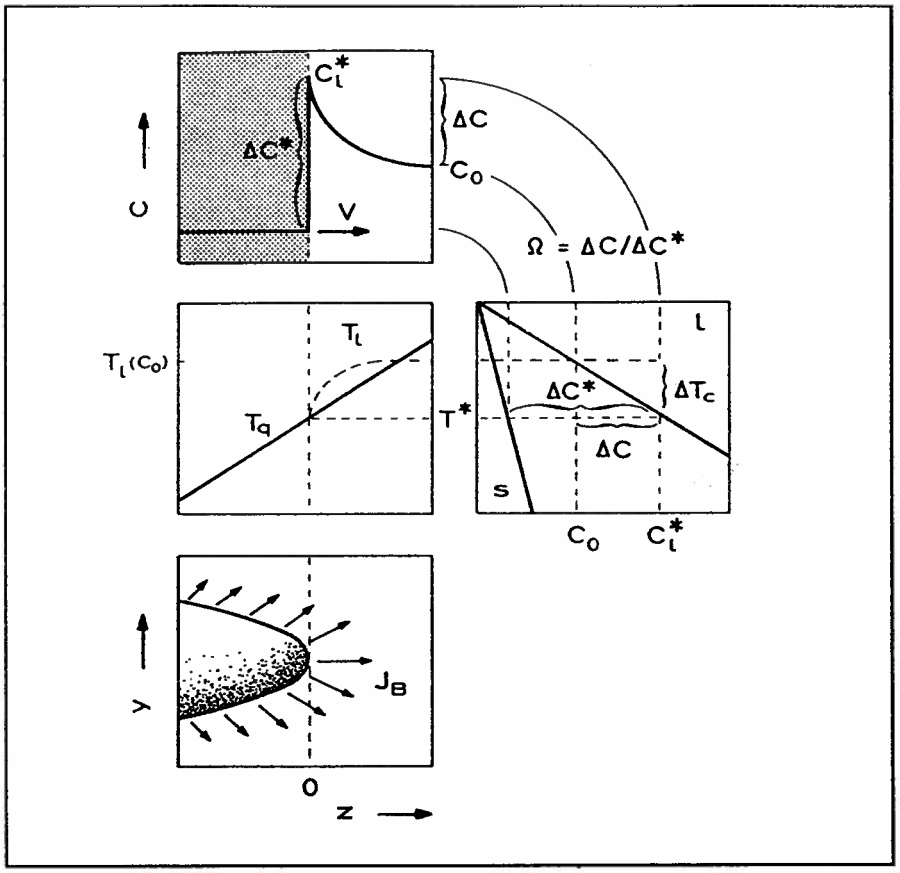

Figure 2.2: Solute Diffusion Field and Undercooling at the Tip of a Dendrite[26]

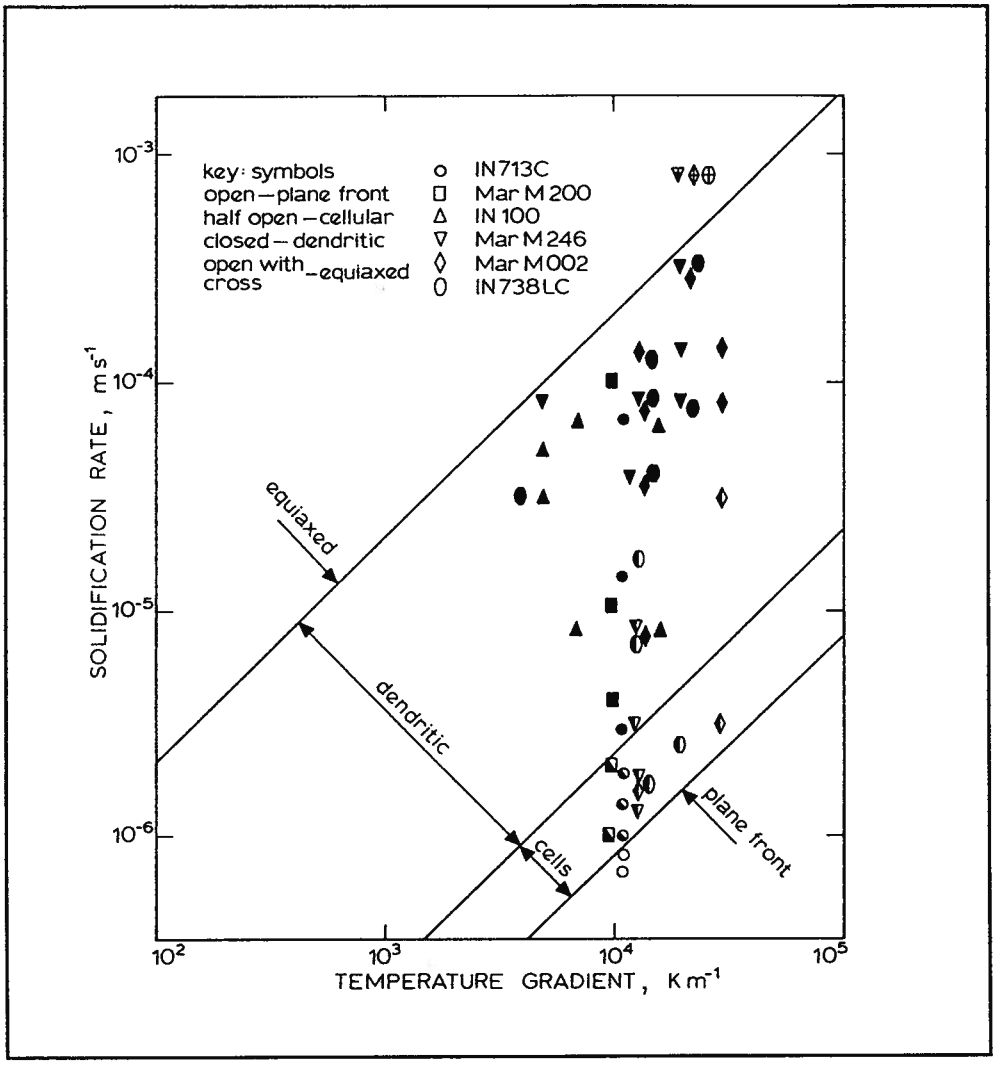

Figure 2.3 Morphologies of Directionally Solidified Nickel Based Superalloys Mapped on a Plot of Log R and Log G. (Ref. 57)

CHAPTER 3: Objectives

The objectives of the present work are to:

1. Experimentally reproduce a CET in AM1, EB refined AM1 and MAR-M200+Hf in which the only source of equiaxed grains is heterogeneous nucleation in the region of constitutionally undercooled liquid associated with the advancing columnar front.

2.. Measure the growth rate and thermal gradient at the solid front during these experiments.

3. Apply the modified Hunt CET model to analyze experimental results in order to determine the nucleation kinetics involved in the generation of equiaxed grains in each of the chosen alloys, and gain insight into the nature of the CET in Ni based superalloys.

CHAPTER 4: Experimental Methodology

Two sets of experiments were conducted during the course of the thesis work. The first set was performed in the solidification labs of the French aeroengine builder SNECMA located in Paris, and with the cooperation of the Paris School of Mines (ENSMP). The second set of experiments was performed at the University of British Columbia. The purpose of each set of experiments was to provoke a CET in AM1 and MAR-M200+Hf in the type of instrumented bar casting available, and measure the conditions under which the CET occurs. The objective in all cases was to directionally solidify the bars under changing thermal conditions which initially give rise to columnar growth, but eventually allow a CET to occur. The directional solidification was desired in order to ensure that the thermal gradients solid/liquid interface were horizontal and therefore measurable with thermocouples situated along the vertical cylinder axis.

4.1 Selection of Alloys

The alloys in the present study were selected in order to investigate the effects of alloy cleanliness and composition on the CET. In addition, they were chosen as representatives of the class of alloy from which they came. The Ni-based superalloys AM1, electron beam remelted (EB refined) AM1 and MAR-M200+Hf were used for the present study. AM1 is a typical "first generation" alloy designed in France for the manufacture of single crystal turbine blades, and does not differ appreciably in alloy content from the other first generation single crystal alloys. MAR-M200+Hf is a widely

used alloy for columnar grained turbine blades, and is typical of the compositions found in this class of alloys. The two alloys differ in their compositions primarily in that AM1 lacks substantial concentrations of the grain boundary strengthening elements found in MAR-M200+Hf such as Hf, Zr, B and C. Table 4.1 shows the compositions of the alloys used in the experiments. All alloys were from standard vacuum induction melted aircraft quality accepted heats. The liquidus temperature for AM1 was determined by DTA analysis at the experimental labs of SNECMA/Corbeil to be 1359 °C. The liquidus temperature for MAR-M200+Hf was determined to be 1358°C at Special Metals Corporation using a TA Instruments model 2910/1600 DTA machine.

The EB refined AM1 was processed in a small batch at the experimental Electron Beam Cold Hearth Remelting furnace at Leybold Durferrit in Frankfurt, Germany. During the EB refining process there may be significant losses of Cr and Al from the alloy due to the relatively high vapor pressures of these elements at the refining temperatures. The losses occur chiefly from the hearth region of the furnace, where the alloy experiences considerable dwell time as liquid before being poured into the copper chill ingot mold. However, during the refining procedure, large amounts of dross appeared on the surface of the melt in the hearth. According to the research engineer in charge of melting at Leybold, the amount of dross observed would reduce the evaporative losses to the extent that insignificant changes in alloy chemistry would result. Therefore the EB refined AM1 was not analyzed for Cr or Al content.

4.2 SNECMA Experiments

Cylindrical bars 20 mm in diameter and 160 mm in height were solidified for the experiments conducted at SNECMA. Cooling of the bars was accomplished by withdrawing them from the hot zone of a Bridgeman type furnace to the cold zone. Ceramic moulds for the bars were made using the lost wax process in which a wax model of the cast piece is made, then coated with successively thicker layers of ceramic slurry until a shell of 3-8 mm in thickness is built up around the wax model. The mold is then flash dewaxed in an autoclave to remove the wax from the original model, and the empty ceramic shell is dried, and then baked at high temperature to sinter the agglomerates together. The moulds include a pouring cup at the top and large flat base at the bottom which mechanically attaches to the water cooled copper chill plate in the furnace. A seed chamber is included at the base of each mould so that if desired, the bar could be grown as a single crystal.

4.2.1 Furnace and Equipment

Figure 4.1 shows a simplified schematic of the experimental Bridgeman furnace used at SNECMA. Details cannot be given due to the proprietary nature of the furnace. The main features of the furnace are the hot zone, the cold zone, the screens which separate the two, and water cooled copper chill plate. Heat transfer in the Bridgeman furnace is almost entirely by thermal radiation. The Bridgeman furnace is designed to solidify castings under controlled conditions of thermal gradient and solidification rate. In the

investment casting of turbine blades, it is desirable to maintain high thermal gradients at the solidification front and a controlled solidification rate of approximately 4 mm/min. The thermal gradient at the liquid/solid interface is kept high by maintaining an ambient temperature in the hot zone well above the liquidus temperature of the alloy. Also required to maintain a high gradient are effective radiation baffles, which minimize radiative heat transfer between the hot zone and cold zone of the furnace. This maximizes the difference in thermal environments experienced by the mold surface as it passes from the hot zone into the cold zone. This maximizes the thermal gradient across the solidification front, which is normally at a level in the casting near to that of the radiation baffles. Controlling the rate of solidification is accomplished by pulling the copper chill plate into the cold zone at a predetermined rate. Throughout each experiment, a vacuum of approximately 10^{-5} Torr was maintained.

4.2.2 Mould Instrumentation and Thermocouples

The bar moulds were instrumented with standard type "B" Pt-6%Rh//Pt-30%Rh thermocouple wire. The thermocouples were calibrated at the high temperature measurement labs of SNECMA (Corbeil) by making one thermocouple pair from the spool set and using it to measure a known temperature. Spool sets were accepted only when the measured temperature was within the specified ±5 °C of the known temperature.

Holes were drilled into the mould for placement of the thermocouples along the vertical axis of the cylinders and at intervals of between 1 and 2 cm. Thermocouple wires measuring 0.3 mm diameter were electrically welded end-to-end so that the junction was at the middle of a continuous length of wire. The entire length was slid down a 1 mm outer diameter high purity alumina tube until the junction was located at the middle of the tube, which was then glued into the drilled holes in the mould with a ceramic bonding agent. The thermocouple wires were then glued down the length of the mould, onto the flat bottom, and finally down the edge and off of the mould altogether. While on the mould the thermocouple wires were completely covered with the ceramic glue. Below the mould edge, fiberglass coverings were used to protect the wires and insulate them from contacting one another. The wire ends were fitted with connecting pins which fit into a vacuum tight assembly at the base of the Cu chill plate, leading to the outside of the furnace.

4.2.3 Data Acquisition Equipment

Two data acquisition systems were used to record thermal data during the SNECMA experiments. The simpler system was a Chessell model 4001 programmable multi channel chart recorder, set to read Type B thermocouples and directly plot temperature. The more sophisticated system was a high performance Hewlett Packard data acquisition center consisting of a data acquisition and control unit model HP3852A, mulitmeter model HP3458A, 20 channel multiplexer model 44710A and computer model

HP01420A. The Hewlett Packard computer data acquisition system was self calibrating and provided temperature data directly from the thermocouple EMF by using standard ASTM thermocouple conversion tables.

4.2.4 Experimental Procedure

A total of nine bar casting experiments were carried out at SNECMA - 7 with AM1 and 2 with MAR-M200+Hf. The conditions necessary to provoke a CET in the bars were unknown at the time of the experiments. Therefore, each experiment was fully analyzed before beginning the next, in order to make any changes to experimental design likely to improve results. A typical cycle in the furnace for the bar casting experiments consisted of a preheat of the mould to approximately 1550°C in the hot zone while a charge of metal was inductively heated to approximately the same temperature in a crucible above the casting. The average charge size was 650 g: enough to completely fill the bar section with enough excess to fill the pouring cup section to a depth of 2 cm. It was desirable to partially fill the pouring cups in order to avoid severe solidification shrinkage porosity in the top section of the bar. The molten metal was poured into the mould, and the mould was held in place while the temperature of the hot zone was lowered to a predetermined temperature near the liquidus of the alloy. Withdrawal of the Cu chill plate into the cold zone was then started at a predetermined rate. Table 4.2 shows the withdrawal rates and hot zone temperatures prior to the start of pulling for experiments with available thermal results.

The Hunt CET model predicts that the CET is favored under low thermal gradients and high growth rates. Therefore, furnace temperature and pull schedules were varied in order to maximize the velocity and minimize the thermal gradient at the liquid solid interface. Table 4.2 gives the schedules for those experiments with available thermal results. Thermal perturbations such as cutting furnace power or opening the radiation baffles were introduced in order to more drastically reduce the gradient and increase growth rates. Moreover, it was assumed that sudden changes in the thermal field would favor the CET. The solid cast bars were cut perpendicularly to the axis into 3 pieces approximately 5-6 cm long, which were themselves cut along their axes. The faces of the resulting pieces were polished to 6μm diamond and etched with Kalling's 2 reagent for 10 seconds to reveal the physical structure.

4.3 UBC Experiments

For reasons to be described later, a second set of CET experiments was carried out at UBC. The superalloys laboratory at UBC was equipped with a furnace designed specifically for producing a CET in high temperature alloys, in which the heat flow is governed primarily by conduction through the bottom of the sample into a water cooled copper chill plate. This offers considerably different heat flow conditions than the SNECMA Bridgman furnace.

4.3.1 CET Vacuum Induction Furnace and Power Supply

The furnace used for the experiments is a vacuum induction furnace as shown in Figure 4.2. The main vessel is a 53 cm tall, 9 cm diameter quartz tube fitted at top and bottom with screw-compressed O-rings. The furnace top consists of a circular steel plate fitted with a 1" diameter viewing window and an O-ring sealed sliding tube. The sliding tube contains thermocouple wires leading from the cold junction at the top to the thermocouple holding assembly at the bottom. Two sliding and locking brass fittings are on the outside of the sliding tube, which allow accurate positioning of the thermocouples during the experiments. Below the furnace lies the vacuum system consisting of reciprocating and diffusion vacuum pumps which allow steady state vacuums of $1\text{-}4\cdot10^{-3}$ Pa to be maintained during the experiments.

The sample was inductively heated by the coil seen wrapped in 5 turns outside of quartz tube as shown in Figure 4.3. The radio frequency power supply to the coil, visible behind the vacuum station, is a Radyne "ET" series 400 kHz RF generator rated at 25 kW. Standard heating power during the experiments was approximately 9 kW with a plate current of 1.5 A and a plate voltage of 6 kV.

The CET sample was contained in a 14 cm tall, high purity alumina tube of 2.5 cm inner diameter and a 3.0 mm wall thickness. This tube is wrapped around the outside with two complete turns of 0.005" thick Mo foil which is an efficient susceptor for the RF induction heating during the experiments. The tube is enclosed by three more

successively larger alumina tubes which act as radiation shields between the hot inner most tube and outer most quartz tube. Additional thermal protection for the quartz tube is provided by cooling fans directed towards the hot zone during the experiments. Figure 4.2 shows only the sample inside of the quartz tube, with thermocouples hanging above. Figure 4.4 shows a schematic diagram of the CET furnace as set up for a typical experiment. Directional cooling of CET samples was accomplished by a water cooled Cu chill plate upon which the alumina tubes rest. The metal charge in turn rests on a 1/2" inch thick circular steel plate which is screwed tightly onto the Cu chill plate. In an attempt to vary the heat flow conditions during different experiments with the same alloy, the steel plate on the Cu chill was varied from 1/2" to 1/4" thickness.

4.3.2 Thermocouples and Sheathing

The thermocouples chosen for the experiments were standard type "D" W-3%Re/W-25%Re due to their stability up to 2200°C and suitability for use in vacuum environments. The 0.005" wires were held in a 1mm O.D. alumina double bore tube, tightly twisted at the junction end and clipped so that about three full twists were left. The twisted end was then carefully bent so that it arced close to the end of the double bore tube and extended minimally in the vertical direction. Each thermocouple was then sheathed with a high purity alumina 2.3 mm O.D. single bore tube. The single bore tubes were previously melted closed at one end by using a propane/oxygen torch. Excess alumina at the end was then ground off on a polishing wheel so as to minimize the "thermal mass" for temperature measuring. The thickness of the alumina at the closed

end tip was consistently 0.5 mm or less, and often was thin enough to be transparent. The double bore tube was always slid down the single bore tubes until the thermocouple junction rested firmly against the closed end tip. Two thermocouples were used for each experiment. The sheathed thermocouples from closed end to top measured 21 and 22 cm ±2mm, and were held in place during the experiments with a steel collar fitted with holes and tension screws. The thermocouples were held so that they were parallel and adjacent to each other, with one tip resting approximately 12 mm below the other tip. The thermocouples were oriented to be coaxial with the tube containing the CET charge.

4.3.3 Data Acquisition Equipment

The millivoltage from the thermocouples was measured using a Kipp and Zonen model BD41 two channel chart recorder and an IBM 286-compatible computer equipped with an Advantech PCLD-789 12 bit voltage measuring board and an external PCL818 board for multiplexing and signal amplification. In order to minimize the bit-flip on the computerized system, a non-standard "user specified" amplification was obtained by inserting a predetermined resistance in the amplifying circuit. The resulting bit-flip was approximately 0.4 °C. The computer was also set to record data at 10 Hertz, so that a moving average technique could be used to further minimize the effective noise. Interference from the induction power supply was minimized with the use of grounded co-axial cables leading from the furnace to both units, however the computer was so sensitive to the noise that it could only be used during the solidification sequences when the power to the coil was completely cut. Measurements made with the chart recorder

during the heating cycles were verified by turning the coil power off for periods of 1 second, which was the only time an accurate reading was guaranteed.

4.3.4 Experimental Procedure

4.3.4.1 Charge Preparation

For each experiment 352 ±2 g of either AM1 or MAR-M200+Hf was placed in the 2.54 cm inner diameter Al_2O_3 tube. This produced a final CET sample approximately 8 cm in height. Alloy samples were generally received as standard 3" diameter casting stick, and had to be cut by an abrasive cutting wheel into small blocks or machined into cylinders. Because of the possible sensitivity of the CET to contaminants which might constitute nucleation sites, the machined cylinders were always surface ground with standard metallographic polishing discs to remove any tool bit debris. In either case, the polishing discs and abrasive cutting wheel are both based on SiC, which is not reported in the literature as being stable in Ni based superalloys[85].

For most experiments the charge was supported away from the steel chill plate by a small piece of alloy so that during melting the liquid alloy would flow onto the chill plate and form a smooth contact with the surface of the steel. For some charges this was impossible as the desired structure (single crystal) required the placement of a seed which would not completely melt away. Therefore, the charges for the series of five experiments involving normal AM1 were supported on 2.5 cm diameter flat bottomed

stubs which were posed directly on the steel chill plate. Two of the normal AM1 experiments (AMSX90 and AMSX45) were seeded with single crystals with the <100> orientations parallel to the direction of heat flow and at 45° to the direction of heat flow, respectively. These orientations would produce dendrites growing parallel to the flow of heat, and at 45° to the flow of heat, respectively, in order to observe the effects of orientation on the CET. A further two of the normal AM1 experiments had additions of TiN (AMTIN) and $MgAl_2O_3$ (AMMGAL) powders, which were placed on top of the charge of alloy in a shallow cavity which had been ground into the top. Enough TiN was added to the AMTIN sample to produce 1000 PPM of dissolved N after Painter[74], who observed that such additions produced marked decreases in the grain size of his equiaxed castings. Due to the Turnbull-Vonnegut calculations showing that $MgAl_2O_4$ nucleates at the lowest of all the calculated undercoolings, 1 gram each of $MgAl_2O_4$ and the similarly structured $CaAl_2O_4$ were added to the AMMGAL sample.

In order to insure a good vacuum during the experiment, the furnace was usually placed under primary vacuum over night. The following morning, after a secondary vacuum of less than 10^{-4} Torr was achieved in the furnace, the induction power supply was turned on and incrementally increased from zero power to about 9 kW during the first forty minutes of the experiment. The charge would melt at the top after approximately one hour, at which time the thermocouples were inserted to a depth of 35 mm to monitor the temperature using the chart recorder. The desired steady state temperature (1600°C - 1650°C) at the top of the sample was reached by fine tuning the power to the coil. Once

steady state had been reached the thermocouples were withdrawn completely from the liquid and slowly lowered again until they touched the liquid surface. This was marked as the "zero" point and provided the basis for the placement of thermocouples during the experiment in terms of immersion depth.

Each solidification cycle was started by switching the thermocouple leads from the chart recorder to the computerized data acquisition system and starting the acquisition while simultaneously cutting power to the induction coil. Each solidification sequence lasted about 350 - 400 seconds, after which power to the coil was restored for the next heating cycle. Each heating cycle consisted of two parts: 700-900 seconds of high power heating to bring the temperature in the range of the previous steady state temperature, followed by 600-800 seconds of steady state power to "fine-tune" the temperature to within 5°C of the target. Overheating during the high power reheat stage was carefully avoided to minimize evaporative losses. The heating cycles generally lasted 1500 seconds and were concluded by moving the thermocouples down for the next sequence by 5 mm if in the equiaxed zone, or 3mm if in the columnar zone. The steady state temperature at the new location was recorded and a new solidification cycle was started. Up to twelve sequences were performed for each casting, thereby simulating a single solidification experiment instrumented with 24 thermocouples.

After each experiment the CET sample and thermocouples were allowed to cool overnight under secondary vacuum. The furnace was then vented to air, disassembled

and re-assembled with none of the alumina insulating tubing to visually confirm that the thermocouples were centered over the top of the CET sample. The thermocouples were then lowered until they touched the solid surface of the sample, and the difference between this level and the "zero" position mark was recorded. The mass of the CET sample was recorded, as was the mass of any condensate on the inside upper portions of the alumina tube. Condensate was removed from the tubes and kept for future analysis. The thermocouple sheaths were also kept as they bore physical markings clearly indicating the last immersion depth in the experiment.

The CET samples were then cut in half along their axes with an abrasive cutting wheel, surface ground, polished to 6 micron diamond and etched with Kalling's 2 Reagent for approximately 10 seconds to reveal the physical structure. The grain size in the equiaxed zone was estimated by counting all the grains above the transition and below the solidification shrinkage cavity, and using the area of this section to give an average area per grain. Spherical grain shape is then assumed to yield the average grain diameter. The number of columnar grains intersecting the CET were also counted. The primary dendrite arm spacing was measured by sectioning the <100> seeded experiment with AM1 in four places in the columnar zone, ending just below the CET. A CET specimen from one of the MAR-M200+Hf experiments was also found to have a large grain oriented with the <100> direction nearly parallel to the axis of the cylinder, and was also sectioned in four places in the columnar zone to give primary dendrite arm spacing.

Finally, the position of the CET was measured as the position above the bottom of the specimen at which the first equiaxed grains is observed.

4.3.5 Calibration

High temperature measurements such as those made in the present study are subject to errors from several sources. It is the purpose of calibration exercises to minimize these errors, or to quantify them and later compensate for the known deviation in measured results. Possible sources of experimental error during the UBC experiments were the gain of the data acquisition system and the accuracy of the thermocouples. In addition, thermal results may be affected by heat loss from the thermocouples or by delayed thermocouple response due to a large response time. Hence, these factors must be quantified to avoid further errors.

4.3.5.1 Data Acquisition Systems

Before each series of experiments the chart recorder and computerized data acquisition system were calibrated using a PROMAC Series DHT 720 portable digital calibrator. The computerized system was fed a signal simulating the full thermocouple range and the resulting output was used to establish the gain of the amplifier on each of the two channels used for data acquisition.

4.3.5.2 Thermocouples

The thermocouples were calibrated with 99.9% pure Ni for each experiment, however due to breakage and the occasional formation of shrinkage cavities around the thermocouple tips, calibrations are available only for a limited number of experiments. Therefore, the calibrations are averaged and applied to each of the experiments using thermocouple wire from the same lot number. Each calibration experiment involved repeating the solidification cycle of pure Ni 5 or 6 times, from which the average plateau temperature was used for the calibration.

4.3.5.3 Thermocouple Response Time

An attempt was made to test the thermocouples for in-situ response time in pure Ni by allowing liquid Ni to supercool by various amounts (20°C - 130 °C) before solidification started. The solidification of a pure metal is rapid since the dendrites grow at a rate controlled by thermal diffusion rather than solute diffusion. Dendrite tip growth rates in pure Ni with an undercooling in the above range have been reported to range from 0.5 - 15 meters per second[86]. Therefore the recalescence during the start of solidification of undercooled pure Ni can be approximately viewed as an imposed Dirac function in the thermal field around the thermocouples. The response time of a thermocouple is defined as the time required to reach 63.2% of an instantaneous temperature change[91]. Therefore, the response time here is defined as the time from the start of recalescence taken by the thermocouples to increase in temperature by 63.2% of the recorded

undercooling. The response time is calculated using a polynomial fit by least squares to the raw data as a means of interpolating the temperature vs. time between data points. However, because the recalescence in pure Ni is in fact limited by the growth of the solid and conduction of latent heat into the liquid, the resulting response times represent an upper limit on the response time of the thermocouples as defined by the literature.

4.3.5.4 Thermocouple Immersion Depth

Temperature measurements in the range of the present study may be strongly affected by radiative heat losses from the thermocouples if they are not immersed sufficiently in the medium of interest. Because each CET sample is characterized by its thermal response at various positions, it is necessary to establish the minimum submergence depth required for accurate readings. In order to establish the suitable minimum immersion depth for the present experiments, pure Ni was used in an alumina tube of the same dimensions as those used in the experiments, except for a 3 cm tall alumina plug separating the pure Ni from the Cu chill to avoid directional freezing. The thermocouples were arranged as in the CET experiments, with one 12 mm longer than the other. The longest thermocouple was brought into contact with the surface of the pure liquid Ni and a solidification cycle was started. This was repeated at increasing depths to investigate the effect of thermocouple immersion depth on the apparent temperature at which the solidification plateau is observed.

TABLE 4.1: Compositions of Alloys Used in CET Experiments

Elements	Ni	Cr	Co	Mo	Al	Ti	W	Ta	Nb	Hf	C	B	Zr
AM1 wt% (*=PPM)	bal	7.52	6.64	2.06	5.34	1.25	5.59	7.80	0.01	.004	80*	3*	10*
MARM-200 +Hf wt%	bal	8.40	9.52	0.03	4.98	1.92	11.9	0.10	0.86	1.18	0.14	150*	400*

TABLE 4.2: Conditions During SNECMA Experiments

Experiment Designation and Alloy Used	Pull Rate (mm/sec)	Temperature of Hot Zone At Start of Pulling (°C)	Method of Thermal Perturbation	Time of Perturbation (sec)
CET#2 (AM1)	0.133	1390	Open Screens	486
CET#4 (AM1)	0.50	1390	------	
CET#5 (AM1)	0.25	1380	Furnace Off	300
CET#6 (AM1)	0.25	1375	------	
CET#8 (MAR-M200+Hf)	0.25	1370	------	
CET#9 (MAR-M200+Hf)	0.25	1370	Open Screens	210

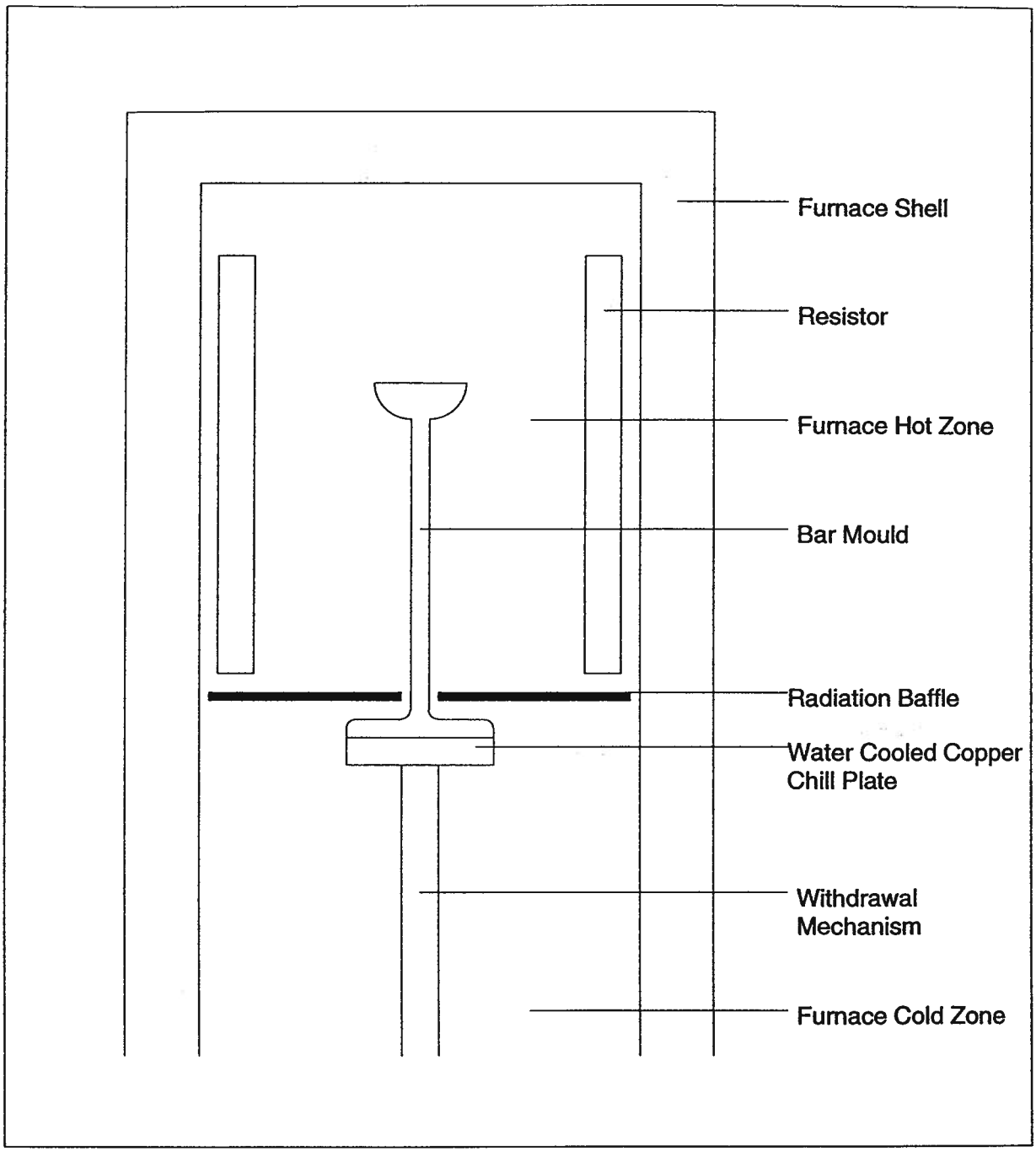

Figure 4.1 Schematic Diagram of Experimental Bridgeman Furnace as SNECMA

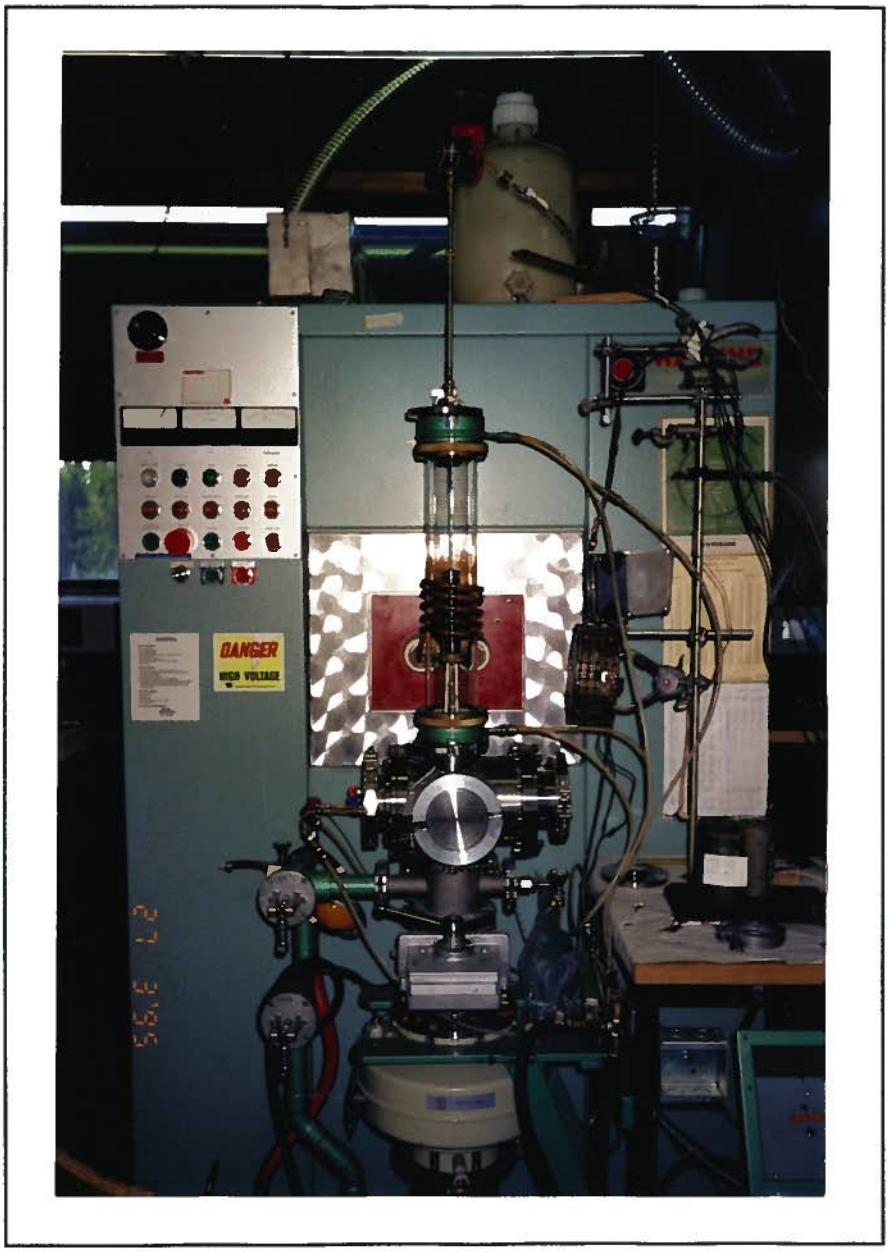

Figure 4.2: Vacuum Induction Furnace Used for CET Experiments at UBC

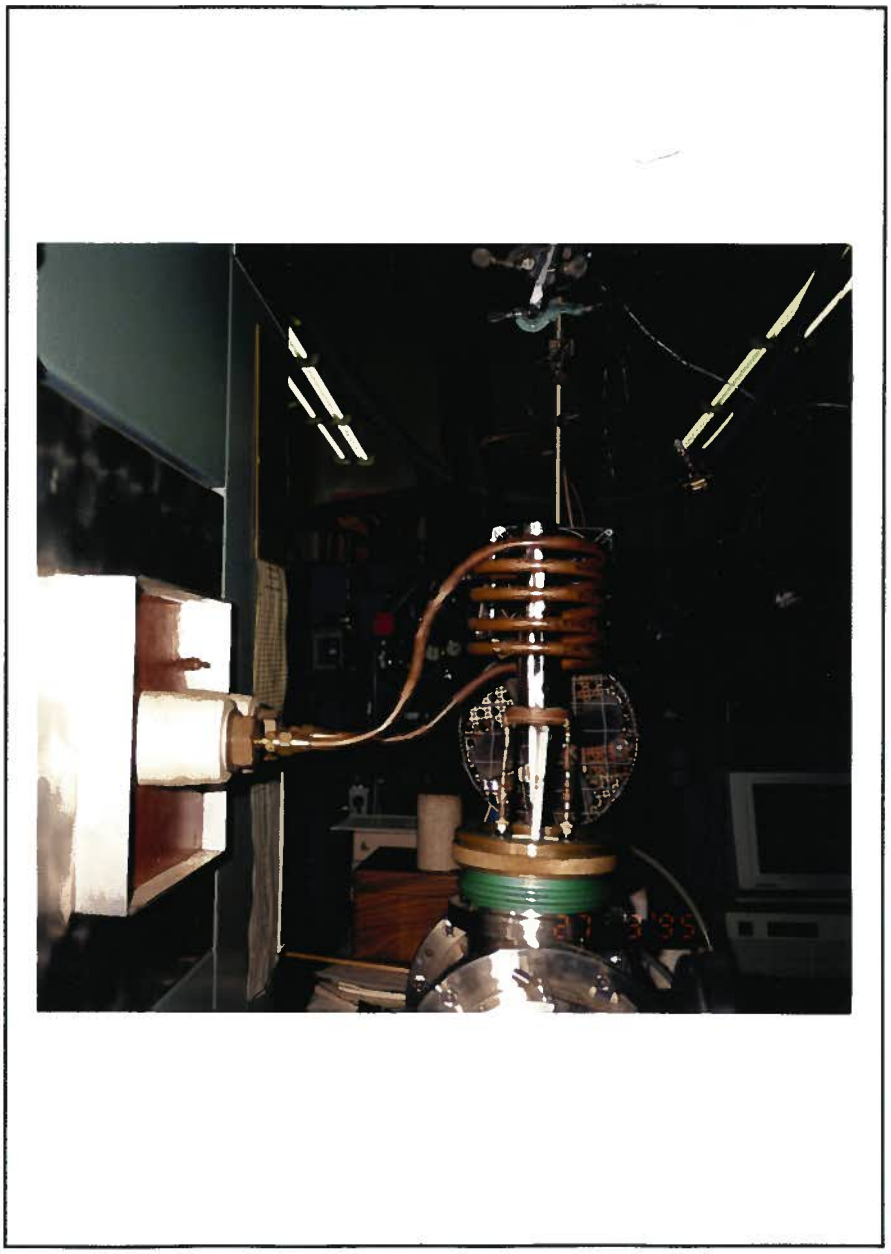

Figure 4.3: Induction Coil and CET Sample Mounted on Cu Chill Plate

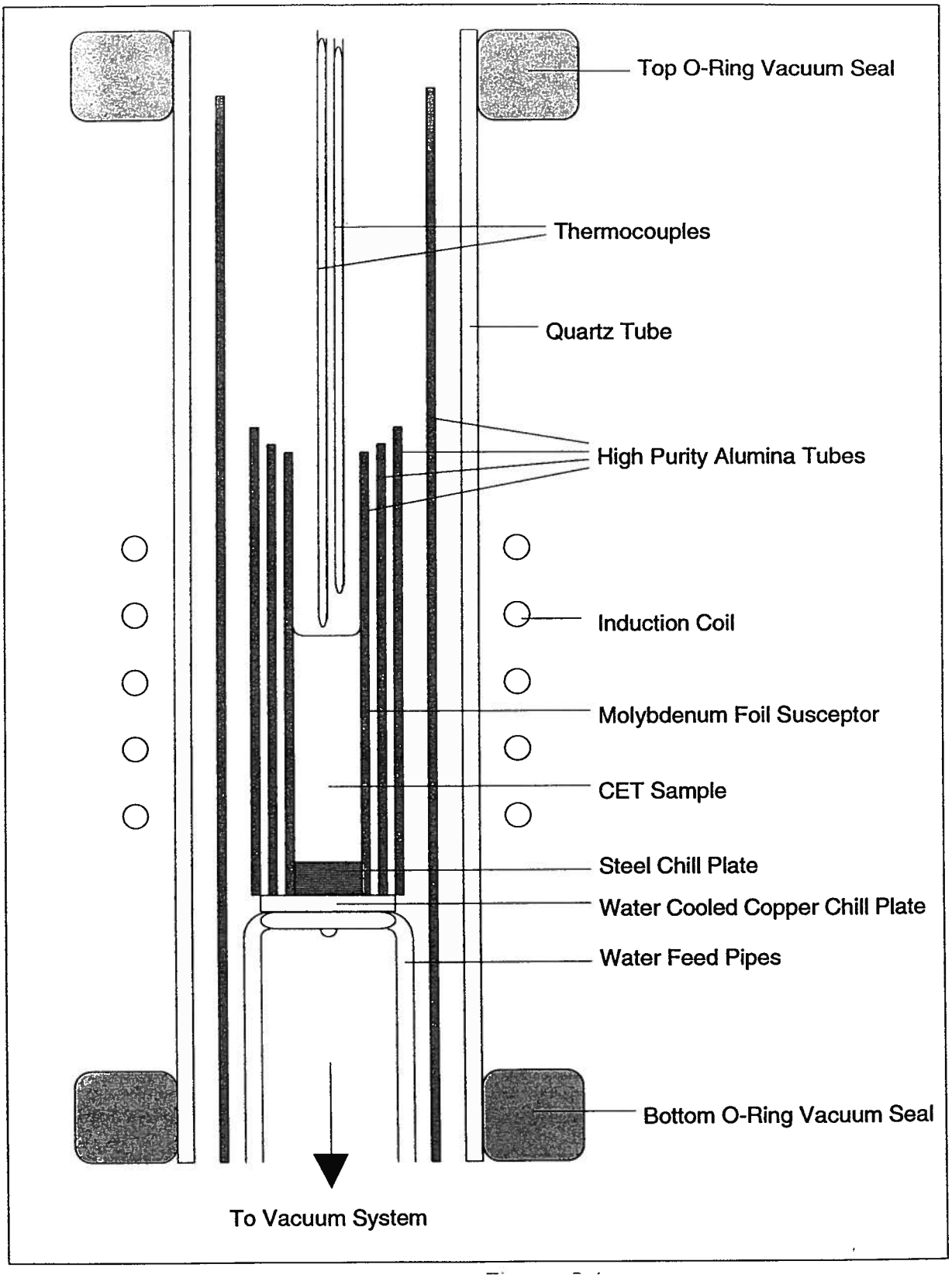

Figure 4.4 Schematic Diagram of Vacuum Induction Furnace Used for UBC Experiments

CHAPTER 5: Results and Discussion

5.1 SNECMA Experiments

During the bar casting experiments at SNECMA some problems were encountered with electromagnetic interference in the data acquisition systems. As a result, no thermal data are available for experiments CET# 1, 3 or 7. As it is desired to discuss the observed physical structure in light of the thermal data, these experiments will not be considered in this chapter. Nonetheless, the remaining experiments provide a wide range of solidification conditions to be studied in relation to the resulting structure. Referring to Table 4.2, experiments CET#2 and CET#4 represent the minimum pull rate (0.133 mm/sec) and maximum pull rate (0.50 mm/sec), respectively, of all the SNECMA experiments. The next four experiments all use the same pull rate of 0.25 mm/sec. Experiments CET#5 and CET#6 with AM1 provide similar conditions at the start of pulling into the cold zone, but the furnace power is shut off during CET#5 while power is maintained throughout CET#6. Similarly, experiments CET #8 and CET#9 with MAR-M200+Hf provide identical furnace operating conditions (in terms of pull rate and hot zone temperature) except that the radiation baffles are fully opened during CET#9 while left closed during CET#8.

5.1.1 Physical Structure

The SNECMA experiments were unsuccessful at provoking a classical CET, suitable for analysis with the Hunt model, in the bar section of the castings. The physical structures

of the bar sections obtained from the experiments with available thermal results are shown in Figures 5.1 - 5.6. Each figure consists of three parts, showing the three sections cut from the original bar. The sections are positioned with their highest ends towards the top of the page and in order of increasing height in the bar from left to right. The magnification in all of Figures 5.1-5.6 is 1.6X, except for Figure 5.1 which shows a high magnification photograph of the top part of the bar to show the dendritic structure. The holes visible along the centerline of each bar section are the alumina tubes in which the thermocouples were held. The indications of height above the copper chill plate given in the figure captions include the length of the seed chamber which has been cut off and is not shown. The seed chamber generally ends at a height of 55-65 mm above the copper chill plate.

Figures 5.1-5.6 show that for all experiments, the entire length of the bar is occupied by the grains originating from the bottom of the casting, with three minor exceptions. Figure 5.1 shows that experiment CET#2 had several equiaxed grains at the top of the bar and to one side only. Figure 5.6 shows that experiment CET#9 has several misoriented columnar grains along the bar axis and also near the top of the bar. Figure 5.3 shows the presence of a single misoriented columnar grain along the centerline and at the top of the bar from CET #5. None of these structures constitutes a classical CET which can be analyzed by the Hunt model. On the other hand, most of the pouring cup sections were equiaxed in structure. However, the sudden increase in cross sectional area where the bar section meets the pouring cup strongly affects the thermal field, creating

conditions far from unidirectional heat flow. As a result, a change in grain structure in this region is unsuitable for analysis with the Hunt CET model unless complex heat transfer modeling is also applied, which is beyond the scope of the present work. For this same reason, it is important to verify the nature of the heat transfer in the bar sections by more closely examining the morphology of the dendritic array found there.

Individual dendrites are visible in Figures 5.1 - 5.6. Figure 5.1a shows vertically oriented primary dendrite trunks, with little secondary growth, dominating the structure of the bottom most section of the bar from CET#2. However, Figure 5.1b shows a change in the morphology of the dendritic array beginning at the bottom thermocouple of this section. Secondary and tertiary growth become evident, and continue to dominate the dendritic structure until the top of the casting. The same morphological transition from primary growth to secondary and tertiary growth is also evident near the bar bottom in CET#6 as shown in Figure 5.4a, and at the top of the bottom section in CET#8 as shown in Figure 5.5a. For the experiments similar to CET#6 and CET#8 but with thermal perturbations applied, the morphological transition is even more evident. Figure 5.3 not only shows the transition for experiment CET#5 lower in the bar, but also a structure completely dominated by horizontal, secondary growth in the uppermost section of the bar. The same phenomena is also clearly shown in Figure 5.6 for CET#9, while CET#4 appears to be dominated by horizontal secondary growth throughout the entire length of the bar as shown in Figure 5.2. However, the nature of this secondary and tertiary growth is difficult interpret from sections cut along the bar axis.

Transverse sections of the bars from 3 of the SNECMA experiments were made in order to more clearly show the transition in morphology of the dendritic array. Three sections were taken from each bar: from the bottom, middle and near the top. Figures 5.7 - 5.9 show photographs of the polished and etched sections from experiments CET#2, 6 and 9, with indications of the positions in the bar from which they were taken. The dark bands visible in all but the bottom most sections result from the angle made between the polishing plane and the plane containing the horizontal dendrites as described by Weinberg[96]. In all cases the dendritic array near the bottom of the bar consists of ordered dendrites with relatively little secondary growth. However, all the middle and top sections shown in Figures 5.7 - 5.9 clearly indicate a structure dominated by the growth of horizontal, secondary dendrite arms. The same change in dendrite morphology is apparent in all other CET experiments performed at SNECMA. This morphology could result from a strongly inclined solidification interface due to the radial heat transfer in the bar.

A simple calculation of the local heat transfer from the mould surface just entering the cold zone shows the relative heat transfer at the surface compared to internally in the bar. Using values of ε, k_{metal} taken from Dominick[95], if the mould surface temperature just under the radiation baffles is assumed to vary from 1360°C to 1000°C as it enters a cold zone at 300°C, heat transfer rates of approximately 126 and 37 kW/m^2 would result at the bar surface. Equivalent rates of heat transfer across a horizontal solid/liquid interface would require thermal gradients in the metal of approximately 110 and 32°/cm, respectively. This indicates that radial heat transfer in the bar can represent significant

portion of the overall heat transfer, particularly at the low thermal gradients required to provoke a CET. As a result, the solid/liquid interface could become inclined in order to release latent heat in a manner which better accommodates the prevailing mode of heat transfer. This could explain the observed morphology of the dendritic array. Moreover, Figure 5.6c shows that equiaxed grains are found along the centerline for experiment CET#9 in the top portion of the bar. This strongly suggests that the front was almost vertical when the equiaxed grains nucleated. Such a front morphology would be expected to show initial dendrites growing vertically near the mould wall, from which secondary growth would occur inwards towards the bar center. This was observed in the top sections of experiments CET#2 and #5. Figure 5.1c shows an enlargement of the top section of CET#2, which shows a vertical dendrite adjacent to the mould wall from which secondary growth toward the bar center is seen.

Hence the thermal results are extremely difficult to interpret as a result of the complex heat flow conditions. Further, the thermocouple data can only indicate the vertical components of G and R along the centerline of the casting. Unfortunately this disallows analyzing the thermal results with Hunt's simple analytical CET model, which requires unidirectional heat flow and a flat, horizontal columnar front. Nonetheless, the thermal results are useful to review insofar as they provide a first approximation of thermal conditions in the bar during solidification.

5.1.2 Thermal Results

5.1.2.1 Recalescence in Pouring Cups

After the first observation of equiaxed structure in the pouring cup in CET#2, thermocouples were implanted in all the pouring cups to measure the recalescences associated with equiaxed solidification. Table 5.1 shows the structure and recalescence if applicable of pouring cup sections for experiments with thermal results.

Table 5.1 shows that the recalescences are relatively consistent and average 4.6°C. The recalescences in the pouring cup provide a first approximation of the undercooling required for heterogeneous nucleation in the superalloys studied. The average undercooling of 4.6°C is attained by the dendrite tips of these superalloys at a growth rate of 0.41 mm/sec according to the KGT calculation, using the pseudo-binary alloy method. Under this criterion, the CET should occur for growth rates higher than 0.41 mm/sec at low thermal gradients.

5.1.2.2 Thermal Gradients and Solidification Rates in Bar Sections

Referring to the discussion in 5.1.1, the thermal data collected for the SNECMA experiments only indicates the vertical components of G and R along the centerline of the bars.

For each experiment the minimum temperature before recalescence in the pouring cup was used as an approximation of dendrite tip temperature. The solid front was tracked in

the casting by observing the times at which each successive thermocouple registered this temperature. This provided data on the height of the solid front in the casting vs. time, which could be analyzed by regression techniques to yield the rate of growth of the solid front along the centerline. Thermal gradients at the solid front were calculated using curves which were regression fit to the thermal profiles in the bar at various times which corresponded to the arrival of the front at each successive thermocouple. Figures 5.10 - 5.15 show plots of the solid front position vs. time, solidification rate and thermal gradients for SNECMA experiments CET#2,4,5,6,8 and 9.

Figures 5.10b-5.15b show that the thermal gradients at the solid front are relatively high at the bottom of all castings (7-10 °C/cm) and progressively decrease to approximately 2-4 °C/cm at the top of the casting. An exception to this is experiment CET#2 which begins with the highest thermal gradient of 27 °C/cm and ends with a negative gradient at the top. A further exception is CET#4. Figure 5.11 b shows that in CET#4 the gradient is initially low and steadily increases towards the top of the bar. There is no explanation for this other than the very high pull rate of 0.5 mm/sec used for this experiment; which is why the following experiments were limited to pulling rates of 0.25 mm/sec.

Figures 5.10a-5.15a show that solidification rates varied considerably among the experiments. Figures 5.11a, 5.13a and 5.14a show that for the three experiments which were pulled under unchanging furnace conditions (CET#4, 6 and 8), the growth rates in the bar are constant and almost identical to the rates at which the bar was pulled into the

cold zone. Figures 5.10a, 5.12a and 5.15a show that rapid increases in growth rate result from cutting furnace power or opening the radiation baffles in experiments CET #2, 5 and 9. In all cases the vertical growth rates along the centerline eventually far exceed the estimated 0.41 mm/sec required to provoke a CET in these alloys. In light of this, the fact that no classical CET was produced in any of these three experiments indicates that the previously discussed lack of unidirectional heat flow in the bars has a profound effect on the generation of a CET.

This leaves the problem of the growth rate of the initial dendrites at the outer edge of the bar, which is indeterminate from the available thermal results. However, as a first approximation it may be assumed that they grow with the rates shown in Figures 5.10a, 5.12a, and 5.15a. The undercooling associated with these growth rates still exceeds the average 4.6°C undercooling observed to cause nucleation in the pouring cups, but the situation is very different than if a flat, horizontal front had been growing at the same rate. To understand how the difference between the two situations influences CET behavior, a consideration of the nucleation kinetics involved is necessary.

The initial dendrites growing up the perimeter of the bars were growing into a thin layer of undercooled liquid adjacent to the mould wall, caused by transverse heat transfer from the mould surface. An estimation of the thickness of this undercooled layer is provided by the dendrites visible in the top sections of experiments CET#2 and 5. Figure 5.1c shows a single dendrite situated 1.5 mm from the left edge of the bar from CET#2, and oriented parallel to the bar axis. Secondary growth from this dendrite towards the bar

center is apparent. Figure 5.3c shows two similar dendrites at the left edge of the bar from CET#5. Again, secondary growth originating from the innermost dendrite is apparent. The innermost dendrite is located 1.2 mm from the bar edge. Taking 1.5 mm as the maximum thickness of the layer of undercooled liquid at the bar perimeter, a cross sectional area of 0.87 cm^2 would be undercooled.

The vertical thermal gradients at the perimeter of the bars are unknown. Therefore it is impossible to estimate the volume of liquid supercooled during growth of the initial peripheral dendrites. However, the cross sectional area of undercooled liquid estimated represents 25% of the total cross sectional area of the bar. Hence the chances of finding a nucleation site in the undercooled layer are 25% of what they would be for a horizontal front growing at the same rate. However, the average grain size calculated from all of the equiaxed pouring cups was 0.6 cm in diameter, equivalent to 7.5 nucleation sites per cc. Even a one cm high column of supercooled liquid around the bar perimeter would represent a volume of 0.87 cc. This would indicate a strong likelihood that a nucleation site would be located in the undercooled layer of liquid at the bar perimeter, even for relatively high gradients. However, these calculations can only be viewed as estimates, and serve to show the mechanism by which the reduction in volume of undercooled liquid due to transverse heat flow in the bars could have prevented the CET from occurring.

5.2 UBC Experiments

5.2.1 Calibrations

5.2.1.1 Thermocouple Calibration

Results of the calibration with 99.9% pure Ni are shown in Table 5.2. Each calibration experiment consisted of 4 or 5 repetitions of the solidification cycle, during each of which a thermal plateau was measured. Therefore Table 5.2 represents the results of 68 individual plateau measurements. The average plateau temperature measured during each calibration experiment is given in Table 5.2. The standard deviations of the plateau temperatures measured in each experiment are also given as an indication of the noise experienced from measurement to measurement. Two sets of spools of thermocouple wire were used for the UBC experiments. Therefore the average of all the calibration experiments using wire from a particular spool set was applied as the calibration to the CET experiments using the same spool set. Average plateau temperatures for each spool set are given in Table 5.2, as well as their standard deviations. The standard deviations of the measured plateau temperatures for each spool of 2.17°C and 2.00°C are taken to represent the minimum error with which any individual measurement may be made. The average plateau temperatures are 1437.4°C and 1437.3°C for spool set 1 and 2, respectively. This falls short of the expected solidification temperature of pure Ni (1453°C) by 16°C. No explanation is offered for the observed deviation, other than that it falls close to the 1% error inherent in the thermocouple as specified by the manufacturer.

5.2.1.2 Thermocouple Response Time

Figure 5.16 shows the recalescences measured during the experiment to determine approximate thermocouple response time in pure Ni. For the purpose of more easily comparing all the cooling and recalescence curves plotted on the same graph, the thermal histories were normalized so that the initial cooling curve passes through the solidification temperature of pure Ni at time = 100 seconds. The results of the response time calculations described in 4.3.5.3 are shown in Table 5.3. Response time varies significantly according to the initial undercooling and position of the thermocouple tip relative to the other thermocouple. As the two thermocouples are in very close proximity, the thermal field surrounding the shorter thermocouple's tip is modified by the shaft of the longer thermocouple, leading to an increase in the apparent response time. The time constants at smaller undercoolings are taken to be more relevant to the CET experiments which show small or no recalescences during cooling. These response times may be considered as an upper limit of the true thermocouple response times due to the assumption that the temperature of the melt rises infinitely quickly to the melting point of pure Ni during recalescence.

5.2.1.3 Thermocouple Immersion Depth

Figure 5.17 shows the effect of the immersion depth in liquid Ni of the thermocouple tip upon the apparent temperature at which the thermal plateau of solidification occurred.

Figure 5.17 shows that measured plateau temperatures are highly sensitive to the immersion depth of the thermocouple. This is due solely to the conduction of heat up the shaft of the thermocouple, which is driven by the lower ambient temperature above the surface of the melt. The flow of heat up the thermocouple shaft cools the tip relative to the medium surrounding it, to an extent determined by the thermal environment of the system. This causes an underestimation of the temperature measured. In this case, Figure 5.17 shows that the solidification temperature of Ni is underestimated by up to 50°C at a thermocouple immersion depth of 2 mm. However, the effects of the heat flow up the thermocouple shaft are highly localized to a region near the surface of the liquid. Therefore, the underestimation rapidly decreases as the immersion depth of the thermocouples is increased. Figure 5.17 indicates that increasing the immersion depth beyond 15-20 mm does not produce any further increase in the measured plateau temperature of solidification. Therefore the minimum immersion depth of the shortest thermocouple used to start each CET experiment was set to 18 mm.

5.2.2 Physical Structure

The polished and etched cross sections of the CET samples are shown in Figures 5.18 - 5.32. Figures 5.18 - 5.32 show that the transition between equiaxed and columnar grained structure is clearly visible in most samples and is in nearly all cases a sharp horizontal transition. The position of the CET is indicated by an arrow in each figure. No zone of mixed columnar and equiaxed grains at the transition is visible, which is in agreement with the findings of Weinberg et al.[53,54] and the observations of Hunt[5]. The

lack of a mixed columnar and equiaxed zone differs the findings of Pollock et al.[56], and therefore suggests that in these experiments a mechanism other than the thermo-solutal convection reported by Pollock et al. is responsible for the CET. Moreover, Pollock reported a transition in the morphology of the dendritic array from being dominated by primary growth to being dominated by secondary and tertiary growth preceding the CET. This transition is not observed in any of the CET specimens solidified during the present study. Figures 5.18 - 5.32 clearly show that the dendritic arrays remain completely dominated by primary growth right up until the CET, with consistently small secondary arms and no tertiary growth at all.

Figures 5.18 - 5.32 show that the equiaxed grains are usually dispersed randomly in their size distributions, although some inhomogeneities are apparent in several specimens showing smaller grains concentrated to one side of the equiaxed zone. However, there are no indications that nucleation took place on the alumina tube wall with growth occurring inwards into the equiaxed zone. This indicates that alumina is not an effective nucleating agent in the alloys investigated in the present study, and that the nucleation of equiaxed grains observed may be attributed to other materials already present in the alloys.

Figures 5.18 - 5.32 also show that near the bottom of each specimen is a flat, horizontal transition from a homogeneous appearing region to a fully developed dendritic structure. This marks the position of the solid/liquid interface during the steady state conditions

prior to each solidification cycle and will be referred to as the "steady state base". The flatness of the steady state base in all cases, even in those samples which did not melt down completely to form a uniform contact with the steel chill plate, shows the heat flow to be completely perpendicular to Cu chill plate underlying the casting. Moreover, the typical flatness of the CET interface indicates that the heat transfer remains unidirectional higher up in the bar. Therefore, these experiments satisfy the requirement for unidirectional heat flow necessary for the analysis using the Hunt CET model.

Table 5.4 shows a summary of the physical features of the CET specimens, including positions of the steady state base and the CET above the steel chill plate, the average equiaxed grain size and the number of columnar grains intersecting the CET. The position of the CET above the steel chill plate was measured using the lowest positioned equiaxed grain found at the CET. This is taken to be the best indication of the position of the front during recalescence.

5.2.2.1 Single Crystal Seeded Experiments

Figure 5.28 shows that the <100> seeded experiment (AMSX90) was successfully grown as a single crystal until the CET. The excess alloy extending as a fin on the right side of the sample is from a small crack in the alumina crucible formed during the experiment. In practice, such cracks allow liquid alloy to contact the molybdenum susceptor which leads to its rapid deterioration. Therefore it is assumed that the crack formed in the last or second to last solidification trial, and did not affect the thermal results as a whole.

The equiaxed grain associated with the crack begins to grow significantly below the CET, but because it is isolated to the rightmost few mm of the casting, it is assumed not to affect the position of the CET in the rest of the casting. This observation would suggest that spurious grains in platforms could be nucleated in cracks in the mould, however such an event would be obvious from the excess alloy which filled the crack, as is apparent on the AMSX90 specimen.

Figure 5.29 shows that the experiment seeded to give dendrites growing at 45° to the vertical (AMSX45) had extraneous grains growing at the start of solidification, from the center and edge of the seed. The extraneous grains originating from the seed center cannot be explained, as the same single crystal bar from SNECMA was used to produce both seeds, and no such extraneous grains were visible in AMSX90. The extraneous grains originating from the edge are more easily explained, as it was impossible to perfectly size the seed to the alumina tube, which left a gap around the seed edge. In the case of the <100> seeded experiment, extraneous grains from the sides were overgrown by the <100> grain, which produced dendrites perfectly oriented with the direction of heat flow. However, the misoriented seeded crystal produces dendrites oriented at 45° to the heat flow direction, which is the worst possible orientation. The overgrowth of the 45° oriented grains shows the sensitivity of success in competitive growth to the orientation of the grains. This process can be illustrated by considering the steady state growth under unidirectional heat flow of two dendrites, one of which is perfectly oriented and the other misoriented by θ° to the direction of heat flow. If all isotherms

travel vertically through the system at X mm/sec, the dendrites are also constrained to grow at X mm/sec in the vertical direction. Thus, while the perfectly oriented dendrite grows at X mm/sec in the vertical direction, the misoriented dendrite is constrained to grow at X/cosθ mm/sec along its growth direction. This increase in the real growth rate of the misoriented dendrite leads to a higher undercooling at its dendrite tip. As a result, the misoriented tip is located below that of the perfectly oriented tip by a distance which depends on the thermal gradient present. This distance provides an opportunity for the secondary arms of neighboring, better oriented dendrites to grow in front of the advancing misoriented dendrite and block further growth. Due to the failure of the 45° oriented seed to produce a single misoriented grain leading to the CET, AMSX45 may be considered as a normal AM1 CET experiment.

5.2.2.2 Modified Alloy Chemistry Experiments

The CET specimens with added TiN (AMTIN) and (Ca)(Mg)Al_2O_3 (AMMGAL) do not exhibit smaller than average grain sizes nor show a CET to occur significantly lower in the casting than with the other specimens. Enough TiN was added to the metal in AMTIN to produce a level of 1000 PPM of dissolved N. Samples of the normal AM1 and TiN polluted AM1 taken from the region of the CET were analyzed for N content, with results averaging 2 PPM and 11 PPM, respectively. The analysis was performed at Special Metals Corporation on a Leco Oxygen/Nitrogen Analyzer Model 436. The lack of appreciable nitrogen in the AMNTIN sample could result from the violent offgassing observed during the first three heating cycles, and the fact that a splash zone found to be

rich in TiN was found lining the upper inner wall of the innermost alumina tube after the experiment. In addition, almost all of the oxide powder added to AMMGAL (1 g $MgAl_2O_4$ and 1 g $CaAl_2O_4$) was found sticking to the thermocouple shaft at the end of the experiment. In both cases therefore, the additions made were ineffective in significantly altering the content of the alloy. Moreover, the lack of significantly smaller equiaxed grains in these samples indicates that any effect the additions did have on alloy chemistry were ineffective in changing the nucleation kinetics under the conditions of the present experiments. Hence, AMNTIN and AMMGAL may be considered as normal AM1 experiments.

5.2.2.3 Primary Dendrite Arm Spacing

Table 5.5 shows the results of the primary dendrite arm spacing (PDAS) measurements performed for the AMSX90 and MRCETD experiments. Dendrite arm spacing was calculated assuming that the dendrites are in a square array. Table 5.5 shows that there was a slight increase in the PDAS as the CET was approached, which is expected because of the continually decreasing thermal gradient. Pollock et al. reported a critical PDAS of 320 μm preceding the appearance of randomly nucleated columnar grains, and 600 μm preceding a complete CET. It is significant that immediately prior to the CET, the measured PDAS in this study (256μm for AMSX90 and 239μm for MRCETD) is well below both of these critical values. Figure 5.33 and 5.34 show microphotographs of the dendritic structure from the cross sections of the AM1 single crystal AMSX90

experiment and the MAR-M200+Hf MRCETD experiment, respectively. Each figure shows a microphotograph of the structure at the bottom of the columnar zone and one at the top, just prior to the CET. In each case the columnar zone is approximately 20 mm long. Both figures show a significant increase in PDAS from the bottom to the top of the columnar zone. However, the basic morphology of the dendrites remains the same.

5.2.2.5 Evaporative Losses

The inside of the tube containing the CET specimens is found to show two types of condensate. Immediately above the liquid surface and extending for about three cm in height is a band of condensate in the form of discrete droplets ranging in size from 0.5 mm to 3.0 mm in diameter. Further above and extending to the top of the tube lies a thin solid ring of "shelf" condensate. Both types of condensate were collected from several experiments, mounted, and polished to 1μ diamond, and analyzed for all elements found in the parent alloy using the EDX analysis tool on the SEM at UBC. Results of the analysis are shown in Table 5.6. Only those elements are shown for which amounts exceeding 1 weight percent were detected. The average total evaporative losses from each series of experiments are shown in Table 5.7.

The average mass lost from each specimen was 16.1 g, which represents 4.6% of the original sample mass of 352 g. Table 5.7 shows that only about 84% of the total mass lost from each experiment was recovered as condensate. It is assumed that the remaining

lost mass has the same composition as the shelf condensate. A mass balance performed on each series of experiments shows that the average change in composition due to evaporative losses is from 7.55 wt% Cr to 5.66 wt% Cr for AM1, and from 8.40 wt% Cr to 6.28 wt % Cr for MAR-M200+Hf. The analysis for Co remains the same, and all the other elements are enriched by approximately 4.5% of their initial concentrations.

5.2.3 Thermal Data

The first purpose of analyzing the thermal data is to verify the suitability of the experiments for analysis with the Hunt model. The requirement of unidirectional heat flow has already been satisfied as indicated by the flat, horizontal steady state base and CET interface found on each sample. In addition, the Hunt model requires that equiaxed grains be nucleated exclusively in the zone of constitutional undercooling associated with the dendrite tips of the advancing columnar front. The possibility that dendrite arm remelting acts as a source of equiaxed grains in these experiments has already been dismissed, which leaves nucleation at the top of the casting as the only other likely source. Whether this occurs in the present experiments can be tested by examining the thermal profiles for negative gradients at the top of the casting. Also, as the Hunt model is based on steady state growth, thermal profiles in the casting must be linear. While this is unimportant in the solid, it becomes critical in the liquid as the gradient determines the volume of undercooled liquid and the length of time which equiaxed grains have to grow

at a given columnar front growth rate. Therefore the nature of the thermal profile in the liquid prior to the CET will be examined with this criteria in mind. Finally, once the suitability of the present experiments has been established, analysis with the Hunt model requires that the solidification rate and thermal gradient at the solid front at the CET be calculated.

5.2.3.1 Thermal Profiles

Nucleation at the top of the sample prior to the CET would require supercooling which could be detected by negative thermal gradients near the top of the sample. The thermal profile of the CET sample may be constructed by combining the temperatures recorded in all the solidification cycles at the same time after time = 0, when power to the induction coil was cut. Since the thermocouples were at different positions in the casting for each solidification cycle, this produces a complete profile of temperatures within the measured region of the casting. Figure 5.35 shows the typical resulting thermal profiles taken every 25 seconds, from experiment MRCETF with MAR-M200+Hf. Figure 5.35 shows that the top of the casting remains hotter than the center (equiaxed zone) at all times during the solidification cycle until after the CET occurs. This insures that equiaxed grains do not nucleate at the top surface and fall down during the solidification cycle, insofar as the measured region indicates. For reasons previously indicated, the minimum thermocouple immersion depth chosen for these experiments was 18 mm. Hence, complete certainty as to the thermal profile of the top 18 mm of the sample is not

possible. However, the nature of the recalescences resulting from equiaxed growth also provide indications as the source of nucleation, and are useful to review for this purpose.

5.2.3.2 Magnitude and Duration of Recalescence

When a casting solidifies with an equiaxed structure, the appearance of solid is marked by a sudden rise in temperature, or recalescence. Recalescence occurs because the equiaxed grains nucleate at a finite undercooling below the liquidus temperature of the alloy, and then release heat into the surrounding liquid as they grow. However, as the liquid temperature rises, the driving force for heat transfer from the grains into the liquid decreases, which decreases growth rate. Hence the rate of recalescence slows down as the liquidus temperature is approached, and eventually the temperature begins to fall again (recovery). The magnitude and duration of recalescence depend on the undercooling of nucleation and the rate at which latent heat from the equiaxed grains is conducted away. Higher rates of the removal of latent heat lead to smaller magnitudes of recalescence accompanied by quicker recoveries from the rise in temperature. Therefore, regions of a casting showing trends towards smaller recalescences and faster recoveries indicate a higher local rate of heat removal.

Table 5.8 shows a summary of recalescence data for all CET experiments performed, including average magnitude and duration of recalescences, and their standard deviations. Figure 5.36 shows a plot of the magnitude of all recalescences measured in the 5 MAR-

M200+Hf series of experiments against distance from the CET. In this case the magnitude of recalescence is defined as the difference between the highest and lowest temperatures recorded during recalescence. Figure 5.36 shows that there is a significant trend towards smaller recalescences as the CET is approached. Figure 5.37 shows a plot of the time duration for the recalescences in the same series of experiments. In this case, the time duration of recalescence is defined as the time between the minimum and maximum temperatures recorded during the recalescence. It is noteworthy that the shortest recalescence near the CET was 11 seconds in duration, which is more than an order of magnitude larger than the thermocouple response times measured at low Ni undercooling (0.5 and 0.9 seconds). Therefore it is unlikely that thermocouple response time significantly alters the thermal results.

Figure 5.37 shows a significant trend towards smaller durations of recalescence as the CET is approached. The trend is obvious until a height of 20 mm above the CET, at which point the duration of recalescence remains approximately constant. An exception to this is the group of five points located at 30 to 40 mm above the CET, which show a slight decrease in recalescence duration. Each of these points represent the measurement taken at the smallest thermocouple immersion depth (18 mm) for the 5 experiments analyzed here. These points are included for completeness of the data, but cannot be considered as accurate due to the fact that the solidification shrinkage cavities in these experiments extended to depths of 18 to 23 mm below the surface of the sample. Direct visual inspection of the CET sample during the experiments confirmed the appearance of

solid and sucking of liquid from the surface into the shrinkage cavity during or very shortly after recalescence. It is assumed that this affected the nature of recalescence measured in this region.

As indicated above, the trends toward shorter recalescence durations and smaller magnitudes as the CET is approached from above in the equiaxed zone indicate that the removal of heat from the equiaxed zone was almost entirely from below, into the columnar zone. This also indicates that nucleation of the equiaxed grains initially occurred towards the bottom of the equiaxed zone, in the region of constitutionally undercooled liquid above the advancing columnar front. In addition to providing information on heat flow during solidification, recalescence (by its presence or absence) can also be used to indicate the position of the CET. This allows comparison with the physically measured CET position, as well as confirmation of the relationship between thermal response and structure.

5.2.3.3 Equiaxed Vs. Columnar Thermal Response

If a thermocouple is held at a fixed position in an alloy melt during solidification, different thermal histories will be recorded depending on the nature of the solidification taking place. Figure 5.38 illustrates the typical temperature vs. time curves which would be recorded for the two types of growth considered here: directional solidification and equiaxed growth. In the case of directional solidification, or constrained growth, a continuous descent in temperature is recorded as the dendrites overgrow the

thermocouple tip. The only indication that solid is present is a slight decrease in the cooling rate due to the generation of the latent heat of solidification through the solid part of the casting. In the case of equiaxed or unconstrained growth, the appearance of solid is marked by recalescence as previously discussed. The typical thermal histories resulting from directional and equiaxed growth as shown in Figure 5.38 are useful for interpreting grain structure in the CET samples because the transition from columnar to equiaxed growth should correspond to a transition from directional to equiaxed thermal response.

Figure 5.39 shows a typical thermal response of the longer thermocouple in experiment MRCETF as it is lowered into the casting during several solidification cycles. Each cooling curve represents the thermal history of a different solidification cycle, at successively smaller distances from the steel chill plate at the bottom of the casting. Figure 5.39 shows that as the thermocouple moves closer to the steel chill from above, the thermal response changes from the classic equiaxed response to the classic directionally solidified columnar response. The recalescence becomes noticeably shorter in duration and smaller in magnitude and eventually disappears as the thermocouple enters the columnar zone from above. Figure 5.40a-d shows a comparison of the thermal responses from the long and short thermocouples in the same experiment. For the cycles shown, the longer thermocouple is entering the columnar zone while the shorter thermocouple remains in the equiaxed zone. Again, the change in recalescence behavior of the longer thermocouple is obvious compared to that of the shorter, which remains in the equiaxed zone. More importantly, Figure 5.40a-d shows that as the longer

thermocouple is lowered towards the CET, it measures a recalescence while the shorter thermocouple continues to measure a drop in temperature. This is direct evidence that nucleation and growth of equiaxed grains occur first at the CET, and is observed consistently in all the UBC experiments.

The position of the CET is therefore taken as being between the lowest position in the casting at which a cooling curve showing recalescence is recorded, and the highest position at which the classical directional solidification response is recorded. The physical distance in the casting between these positions was generally 3 mm. Therefore the range of uncertainty in the position of the CET determined from the thermal data is 3 mm. Table 5.9 shows a comparison of the physically measured CET positions and the ranges of positions taken from the thermal data.

In order to more accurately compare the positions of the CET predicted using thermal response with the physically measured positions, thermal expansion must be taken into account. The physically measured CET positions must be corrected for the thermal expansion of the thermocouples and of the underlying columnar zone at high temperature. The thermal expansion of the thermocouples was calculated by considering the case of the maximum immersion depth of 70mm, where the immersed thermocouple would be at 1360°C at the time of the CET. Also assumed was a linear decrease in temperature of the non-immersed thermocouple shafts, from the melt surface at 1360°C to the thermocouple holding assembly at 200°C. Previous measurements confirmed the

temperature at the holding assembly. Using a temperature dependent linear expansion coefficient[92] ranging from $7.35 \cdot 10^{-6}$ °C-1 to $9.4 \cdot 10^{-6}$ °C^{-1}, a total lengthening of 1.7 mm was calculated. This was applied to the measurements in order to establish their true distance from the casting bottom. Variations in the thermal expansion from cycle to cycle at different immersion depths were small (<0.1 mm between successive cycles) and had no significant effect on the calculation of solidification rate or thermal gradient. The thermal expansion of the columnar base at the time of the CET was estimated using the recorded thermal profiles in the columnar zone, and extrapolating the thermal field down to the sample bottom. Thermal expansivity data from the SNECMA labs was used in this calculation.

Table 5.9 shows that the CET positions corrected for thermal expansion correspond very well with the ranges predicted by the thermal response. This shows that the thermal response may be used as a reliable indicator of the position of the CET, and that the time at which the CET occurs is shortly after or during recalescence. This hypothesis may be verified by referring to the equiaxed solidification model of Rappaz and Thevoz[87]. Rappaz and Thevoz determined in their model that the peak of recalescence is associated with impingement of the equiaxed grains (ie. a volume fraction of equiaxed grains of 100%) for the relatively large equiaxed grain sizes observed here. Moreover, the volume fraction of equiaxed grains was approximately a linear function of time. Figure 5.37 shows a range of recalescence durations of 11 - 17 seconds near the CET. Therefore, according to this approximation, the grains would reach their half-volume sizes after 5.5

- 8.5 seconds of growth and block the columnar front. Although not critical to the analysis with the Hunt model, this information helps to fix the time of the CET as occurring very shortly after the beginning of recalescence.

5.2.3.4 Growth Rates and Thermal Gradients

Growth rates and thermal gradients at the solid front in the columnar zone were calculated following similar procedures used in the analysis of the SNECMA thermal data. However, the resolution of thermal data in the UBC experiments was much greater owing to the increased number of positions at which thermal results were recorded. The temperature of the solid front was estimated by considering the thermal histories shown in Figure 5.39. The lowest position in the casting showing an equiaxed thermal response defines the upper limit of the position of the columnar dendrites before the CET. In order to be located below this position, the temperature at which the tips were growing must have been less than the minimum temperature recorded in the equiaxed thermal response. Therefore, the minimum temperature recorded in the equiaxed response positioned closest to the CET was used as a first approximation of the temperature of the dendrite tips throughout the columnar region. The columnar front was tracked by observing the times at which each successive thermocouple position recorded the tip temperature. For comparison, the appearance of solid in the equiaxed region was also tracked by observing the time at which cooling rate fell to zero prior to recalescence. The front position vs. time data was then regression fit with a polynomial whose

derivative provided the rate growth in the columnar zone. The polynomial which best fit the position vs. time data was found to be of the form:

$$T = A + Bx + Cx^{1/2} + Dx^2 + Ex^3 \qquad (21)$$

Figure 5.41 shows a typical plot of the columnar front vs. time data (from MRCETF) with the regression fit curve and solidification rate given as well. Also plotted are the times at which solid appeared in the equiaxed zone. The solid data points indicate the separation between equiaxed and thermal responses, and define the limits of the predicted CET position. Note that as the CET position is approached, the rate of solidification rapidly increases. This rapid increase is inherent to the heat flow conditions which give rise to the CET, and results in a considerable variation in the calculated growth rate within the range of predicted CET positions. Hence, the precision with which the raw thermal data may be used to yield growth rates at the onset of the CET is limited.

The thermal gradient at the solid front at the time of the CET was calculated by considering the thermal profile in the casting at the time of recalescence. It was found that equation (21) was also suitable for regression fitting to the thermal profiles. Hence, the derivative of the resulting polynomial provided the thermal gradient throughout the columnar zone. Figure 5.42 shows the thermal profile in the MRCETF casting at the time of recalescence, with regression fit curve and gradient also plotted. Solid data points indicate the limits of the ranges predicted for the CET from thermal responses. As with solidification rate, the thermal gradient changes significantly within the limits of the

predicted CET position. However, the Hunt model requires the presence of an unchanging gradient in the liquid ahead of the dendrite tips. The CET is predicted in the Hunt model by considering nucleation and growth of the equiaxed grains in the liquid ahead of the solid/liquid interface. Therefore, it is the thermal profile in the liquid ahead of the dendrite tips rather than at the dendrite tips which plays a role in equiaxed grain growth. Figure 5.42 shows that beyond the region of the CET, the typical thermal profile is very close to linear, and is always lower than the gradient at the columnar front. Hence, while the values of G at the dendrite tip are usually quoted for CET analysis, they are not applicable to the Hunt model in this case. Therefore, linear regressions were applied to the region of liquid above the CET (in the equiaxed zone) for all castings in order to determine the G applicable to the Hunt model.

The results of the above calculations of R, G at the dendrite tip (G_{TIP}) and G in the liquid (G_{LIQ}) ahead of the columnar zone using regression fit polynomials to the thermal data are shown in Table 5.10. The ranges given for R and G_{TIP} correspond to the maximum and minimum gradient and growth rate calculated within the range of predicted CET positions. The results given in Table 5.10 show a considerable range of values calculated for each CET experiment, representing an uncertainty of about 0.15 mm/sec for R and 4 °C/cm for G_{TIP}. This is equivalent to approximately 50% of the calculated values. The physically measured positions could also be used to calculate G_{TIP} and R. However, the physically measured positions fall randomly within the full ranges of positions predicted

by thermal response. Hence, the fundamental uncertainty in the data would remain unchanged and no consistency would be added to the results.

Nonetheless, the ranges of values calculated for G_{TIP}, G_{LIQ} and R are consistent from experiment to experiment. As observed by Weinberg in his experiments with directionally solidified Al-3%Cu and Pb-Sn alloys, the CET occurs within a well defined band of both G and R. Therefore, the G/R criterion for the CET in superalloys can be neither confirmed or denied. In addition, the average minimum cooling rate from all experiments, taken from $G_{TIP} \cdot R$ prior to the CET, was 0.17 °C/sec. This is well above the 0.1°C/sec cooling rate below which Pollock et al. found that equiaxed grain nucleation began in their experiments. Moreover, the average maximum of $G^{-0.5}R^{-0.25}$ ($cm^{0.25}s^{0.25}°C^{-0.5}$) was found to be 1.04 in the present experiments, whereas Pollock et al. reported a critical minimum of 0.95 in their study. Hence, the present findings are not in contradiction to those of Pollock et al. Rather, they confirm that different conditions of solidification may give rise to different sources of equiaxed grains which cause a CET.

No significant differences in G and R at the CET are noted for 45° oriented seeded or chemistry altered experiments, which is expected as these experiments failed to produce the desired change in alloy chemistry or crystal orientation. Experiment AMSX90 showed results similar to the normal samples. This is due to the competitive growth process at work in all experiments which naturally favors the growth of dendrites oriented close to the direction of heat flow.

TABLE 5.1: Pouring Cup Structure and Recalescence for SNECMA CET Experiments

Experiment Designation	Pouring Cup Structure	Average Grain Dia. (mm)	Average Grains Per cm^3	Recalescence (°C)
SNECMA CET#2	Equiaxed	6.0	9.1	5.0
SNECMA CET#4	Columnar	----	----	----
SNECMA CET#5	Equiaxed	6.8	5.9	4.5
SNECMA CET#6	Columnar/Equiaxed	----	----	4.0
SNECMA CET#8	Equiaxed	6.2	8.2	5.5
SNECMA CET#9	Equiaxed	6.6	6.8	4.0

TABLE 5.2: Results of Thermocouple Calibration to 99.9% Pure Ni

Calibration Experiment Designation	Average Temperature of Thermal Plateau (°C)	Standard Deviation of Plateau Temperatures (°C)
Spool 1 A	1434.1	0.77
Spool 1 B	1435.9	0.32
Spool 1 C	1436.1	0.88
Spool 1 D	1435.6	0.29
Spool 1 E	1438.7	0.65
Spool 1 F	1440.2	1.68
Spool 1 G	1438.2	0.41
Spool 1 H	1439.6	0.44
Average Spool 1	**1437.3**	**2.17**
Spool 2 A	1439.7	2.19
Spool 2 B	1438.1	2.56
Spool 2 C	1435.4	0.37
Spool 2 D	1434.5	0.13
Spool 2 E	1438.6	0.87
Spool 2 F	1438.0	1.77
Average Spool 2	**1437.4**	**2.00**

TABLE 5.3: Time Constants of Thermocouples in Pure Ni

Trial Number	Average Thermal Recalescence (°C)	Short Thermocouple Response Time (seconds)	Long Thermocouple Response Time (seconds)
1	15.4	0.589	0.939
2	18.0	0.528	1.48
3	44.4	0.958	1.86
4	67.2	1.13	1.72
5	40.4	1.19	1.85
6	35.1	1.16	1.55
7	117.0	1.20	1.82
8	132.4	1.20	1.70

TABLE 5.4: Summary of Physical Features of CET Specimens

Experiment Designation	Position of Steady State Base Above Steel Chill (mm)	Position of CET Above Steel Chill (mm)	Columnar Grains Intersecting The CET	Average Equiaxed Grain Diam. (mm)
AMCETB	17.5	38.5	9	4.5
AMCETC	9.0	31.5	6	5.4
AMCETD	15.5	36.0	10	4.2
AMCETE	21.5	42.0	11	4.8
AMCETF	17.0	41.0	11	4.8
MRCETB	11.5	37.0	11	7.1
MRCETC	23.5	47.5	8	6.8
MRCETD	24.5	49.5	6	6.1
MRCETE	19.5	45.0	10	7.9
MRCETF	20.0	43.0	12	4.7
AMSX90	17.5	39.0	1	4.3
AMSX45	19.5	43.5	9	8.0
AMTIN	20.5	42.0	6	5.3
AMMGAL	15.0	40.0	8	4.5
AMNORM	16.5	38.0	11	4.4

TABLE 5.5: Primary Dendrite Arm Spacings in CET Experiments

Distance Above the Steel Chill Plate (mm)	AMSX90 Primary Dendrite Arm Spacing (μm)	Distance Above the Steel Chill Plate (mm)	MRCETD Primary Dendrite Arm Spacing (μm)
20	209	28.5	215
24	214	35	219
31	221	44	223
37.5	256	49.5	239

TABLE 5.6: Compositions of Condensates Collected After CET Experiments

	Al (wt%)	Cr (wt%)	Co (wt%)	Ni (wt%)
Average AM1 Droplet Condensate	5.14	24.9	10.2	59.8
Average AM1 Shelf Condensate	3.32	61.1	5.95	29.7
Average MAR-M200+Hf Droplet Condensate	3.47	27.0	13.9	55.4
Average MAR-M200+Hf Shelf Condensate	1.01	64.5	8.06	26.3

TABLE 5.7: Average Amounts of Evaporative Losses During CET Experiments

Experimental Series	Average Total Mass Lost (grams)	Average Droplet Condensate (grams)	Average Shelf Condensate (grams)	Percent of Total Mass Loss Left as Condensate
EB Refined AM1	15.8	6.1	6.9	83
Normal AM1	16.7	5.9	8.3	85
MAR-M200+Hf	15.9	4.8	8.6	84

TABLE 5.8: Summary of Recalescence Data for CET Experiments

Experiment Designation	Average Peak Temperature (°C)	Average Low Temperature (°C)	Average Recalescence (°C)	Standard Deviation in Peaks (°C)	Standard Deviation in Lows (°C)	Standard Deviation in Recalescence (°C)
AMCETB	1353.0	1351.2	1.8	0.74	1.43	1.24
AMCETC	1354.3	1352.1	2.3	0.75	1.20	1.38
AMCETD	1355.8	1354.2	1.7	0.69	0.91	0.73
AMCETE	1353.6	1351.0	2.6	1.5	2.11	1.10
AMCETF	1354.5	1353.2	1.3	1.70	1.64	0.63
MRCETB	1359.4	1357.6	1.5	1.64	2.25	1.01
MRCETC	1357.6	1355.7	1.9	1.02	0.98	0.79
MRCETD	1355.3	1354.5	0.8	1.54	1.72	0.56
MRCETE	1357.0	1354.2	2.8	0.83	1.87	2.11
MRCETF	1358.4	1356.4	2.0	1.66	1.63	0.79
AMSX90	1353.2	1351.9	1.3	0.91	0.97	0.44
AMSX45	1354.8	1352.8	2.0	1.77	1.47	0.89
AMNORM	1355.7	1354.5	1.2	1.59	1.42	0.65
AMTIN	1354.9	1353.4	1.4	1.45	1.49	0.73
AMMGAL	1355.6	1352.4	3.2	1.66	2.46	2.02

TABLE 5.9: Comparison of CET Positions From Direct Physical Measurement and From Thermal Histories

Experiment Designation	Physically Measured CET Position Above Steady State Base (mm)	CET Position Corrected For Thermal Expansion (mm)	CET Position Predicted By Thermal Response (mm)
AMCETB	21.0	22.6	21.0-22.0
AMCETC	22.5	24.0	25.5-28.5
AMCETD	20.5	22.0	22.0-25.0
AMCETE	20.5	22.0	23.0-28.0
AMCETF	24.0	25.5	24.0-27.5
MRCETB	25.5	27.0	25.5-28.5
MRCETC	24.0	25.6	24.0-27.0
MRCETD	25.0	26.5	24.5-27.5
MRCETE	25.5	27.2	27.0-30.0
MRCETF	23.0	24.5	21.0-24.0
AMSX90	21.5	22.9	25.5-28.5
AMSX45	24.0	25.5	24.5-27.0
AMNTIN	21.5	23.0	20.5-23.0
AMMGAL	25.0	26.5	25.0-27.5
AMNORM	21.5	22.9	23.0-25.5

TABLE 5.10: Growth Rates and Thermal Gradients from Regression Calculations Based on Thermal Data

Experiment Designation	Growth Rate R (mm/sec)	Gradient G_{TIP} (°C/cm)	Gradient G_{LIQ} (°C/cm)
AMCETB	0.33-0.44	2.6-4.0	0.79 ± 0.29
AMCETC	0.19-0.33	6.4-10.8	2.11 ± 0.27
AMCETD	0.22-0.40	3.8-9.1	0.67 ± 0.24
AMCETE	0.45-0.15	0.0-2.7	0.42 ± 0.57
AMCETF	0.22-0.46	4.1-9.0	0.67 ± 0.55
MRCETB	0.33-0.60	4.7-7.2	0.87 ± 0.54
MRCETC	0.33-0.50	4.7-7.2	1.76 ± 0.23
MRCETD	0.32-0.49	4.5-7.9	2.15 ± 0.58
MRCETE	0.34-0.50	0.07-2.8	1.00 ± 0.33
MRCETF	0.28-0.45	3.3-8.1	1.58 ± 0.28
AMSX90	0.35-0.50	3.7-8.0	1.34 ± 0.47
AMNORM	0.24-0.35	4.1-8.9	1.74 ± 0.58
AMTIN	0.28-0.38	8.86-13.5	2.48 ± 0.34
AMSX45	0.31-0.48	2.6-6.3	1.56 ± 0.81
AMMGAL	0.50-1.10	0.2-3.9	0.87 ± 0.75

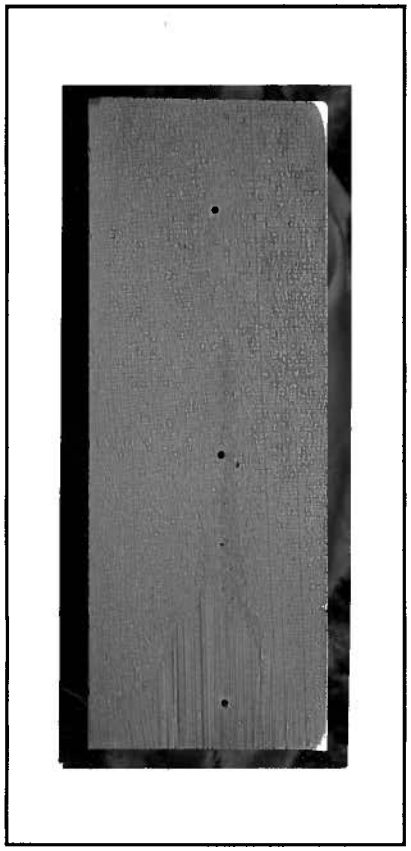

FIGURE 5.1a: SNECMA CET #2
Middle Bar Section: From 113 mm
to 165 mm Above Copper Chill Plate

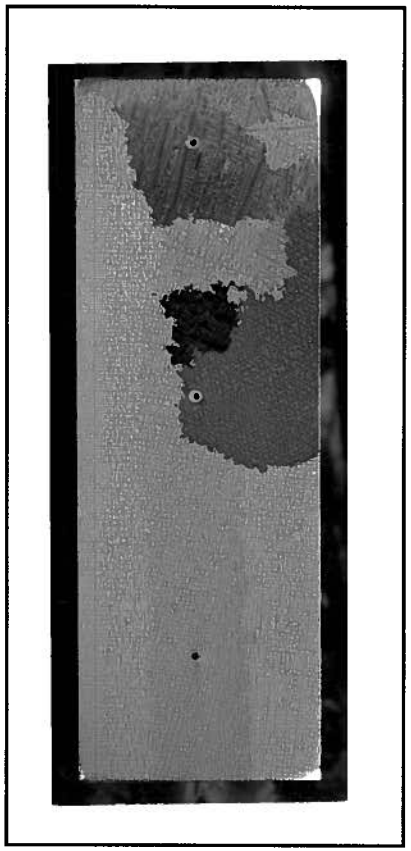

FIGURE 5.1b: SNECMA CET #2
Top Bar Section: From 166 mm
to 221 mm Above Copper Chill Plate

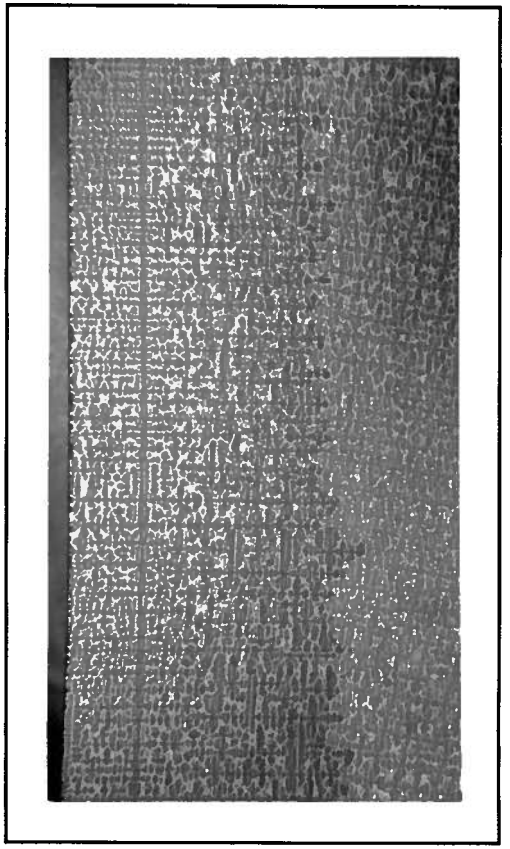

FIGURE 5.1c: SNECMA CET #2
Top Bar Section: Magnification 20X

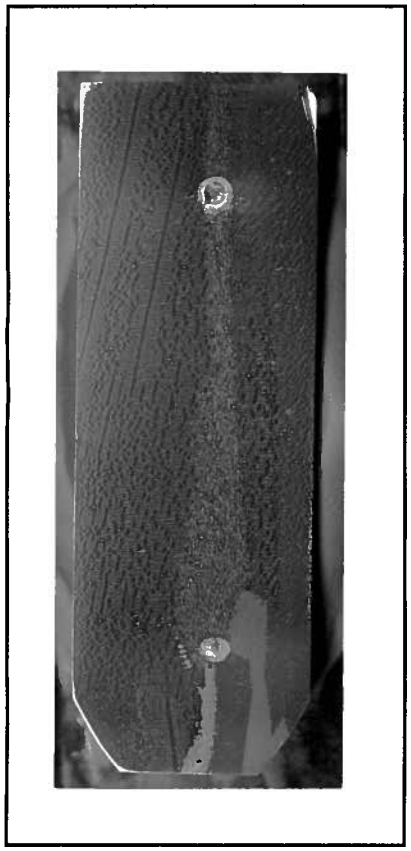

FIGURE 5.2a: SNECMA CET #4
Bottom Bar Section: From 57 mm
to 113 mm Above Copper Chill Plate

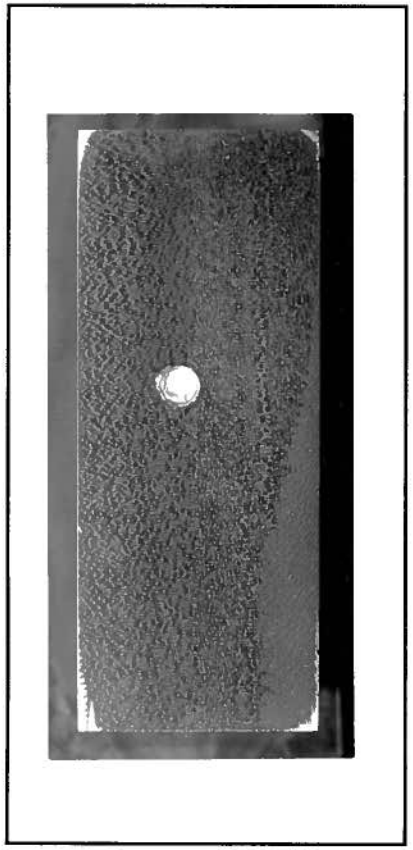

FIGURE 5.2b: SNECMA CET #4
Middle Bar Section: From 114 mm
to 162 mm Above Copper Chill Plate

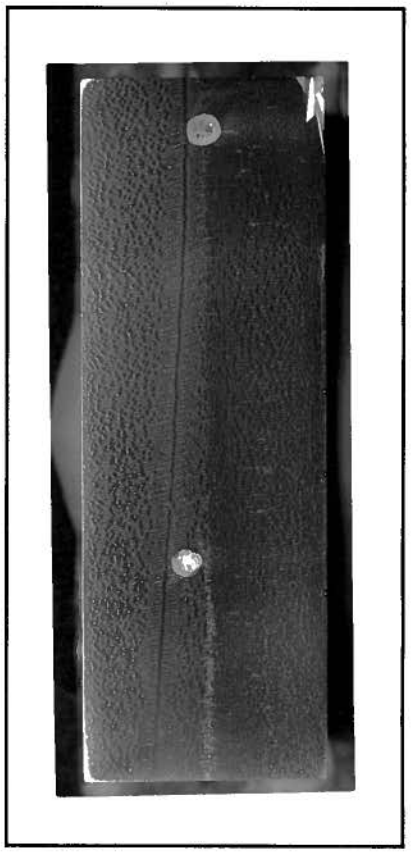

FIGURE 5.2c: SNECMA CET #4
Top Bar Section: From 163 mm
to 219 mm Above Copper Chill Plate

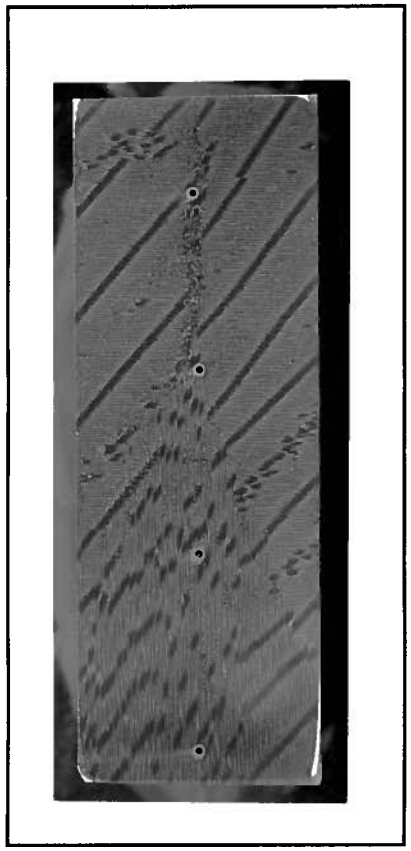

FIGURE 5.3a: SNECMA CET #5
Bottom Bar Section: From 54 mm
to 112 mm Above Copper Chill Plate

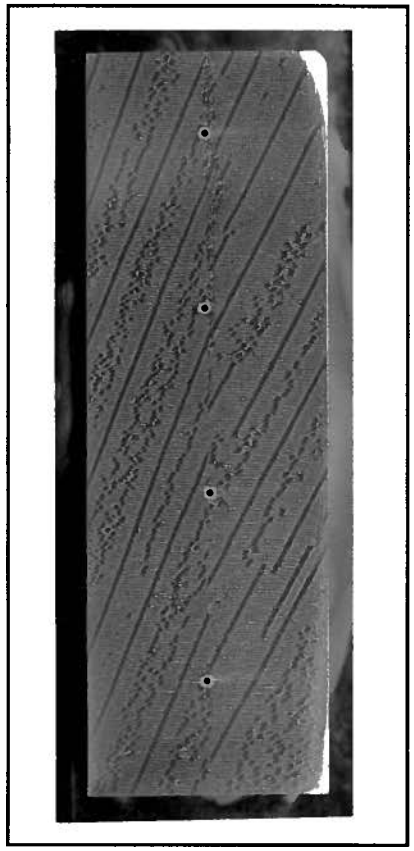

FIGURE 5.3b: SNECMA CET #5
Middle Bar Section: From 113 mm
to 171 mm Above Copper Chill Plate

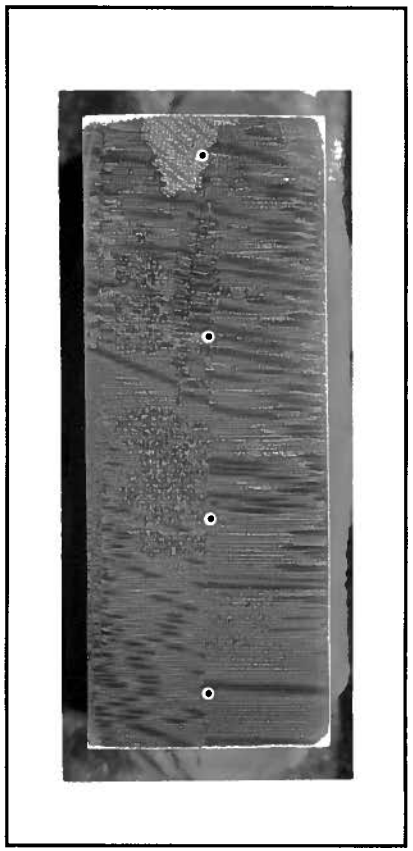

FIGURE 5.3c: SNECMA CET #5
Top Bar Section: From 172 mm
to 220 mm Above Copper Chill Plate

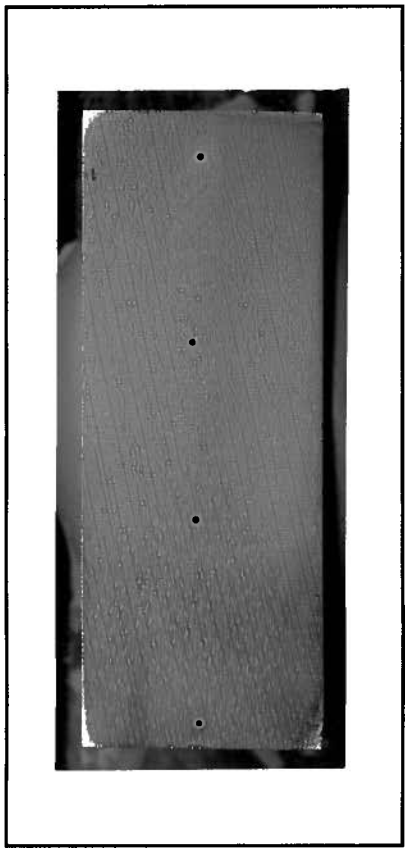

FIGURE 5.4a: SNECMA CET #6
Bottom Bar Section: From 65 mm
to 116 mm Above Copper Chill Plate

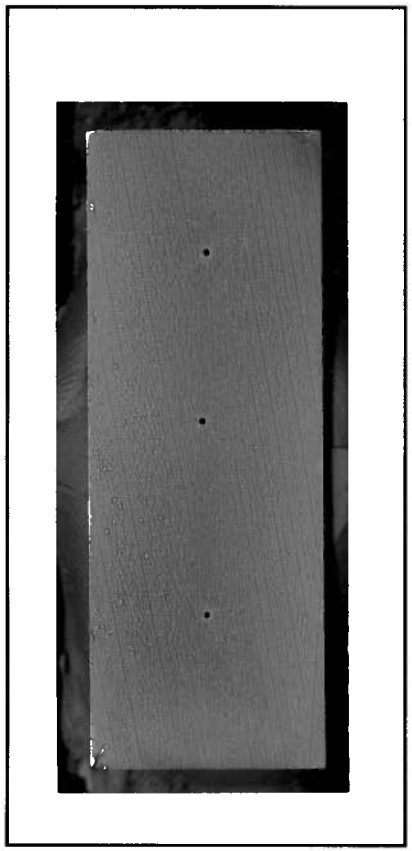

FIGURE 5.4b: SNECMA CET #6
Middle Bar Section: From 117 mm
to 169 mm Above Copper Chill Plate

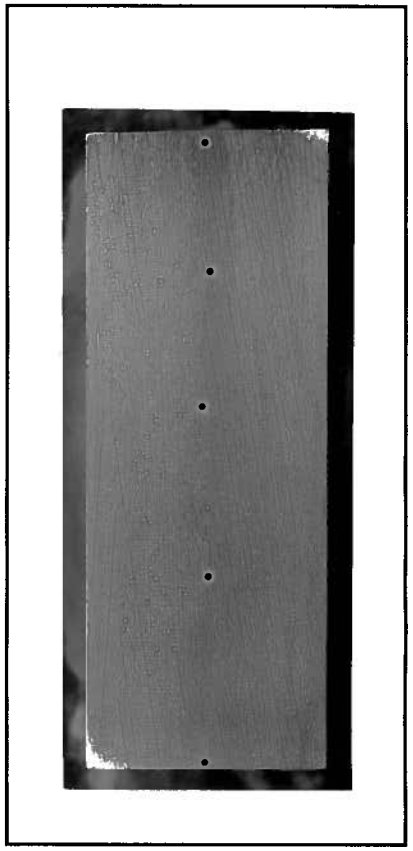

FIGURE 5.4c: SNECMA CET #6
Top Bar Section: From 170 mm
to 221 mm Above Copper Chill Plate

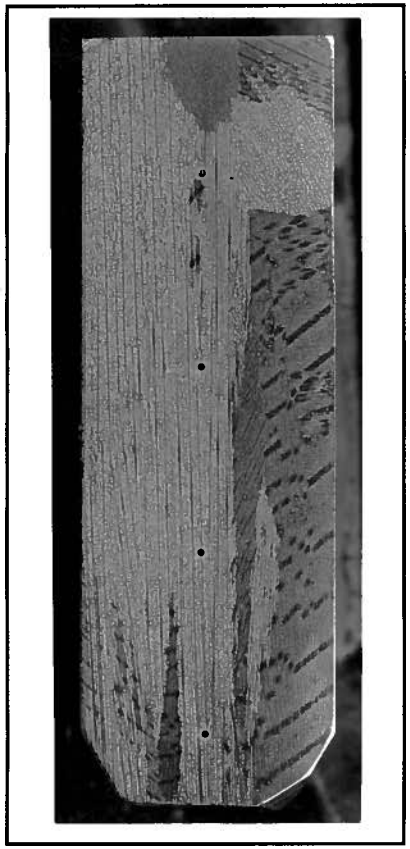

FIGURE 5.5a: SNECMA CET #8
Bottom Bar Section: From 58 mm
to 118 mm Above Copper Chill Plate

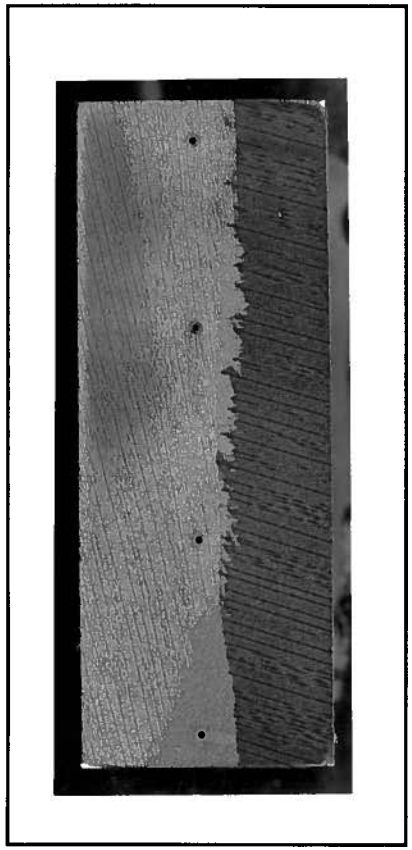

FIGURE 5.5b: SNECMA CET #8
Middle Bar Section: From 119 mm
to 171 mm Above Copper Chill Plate

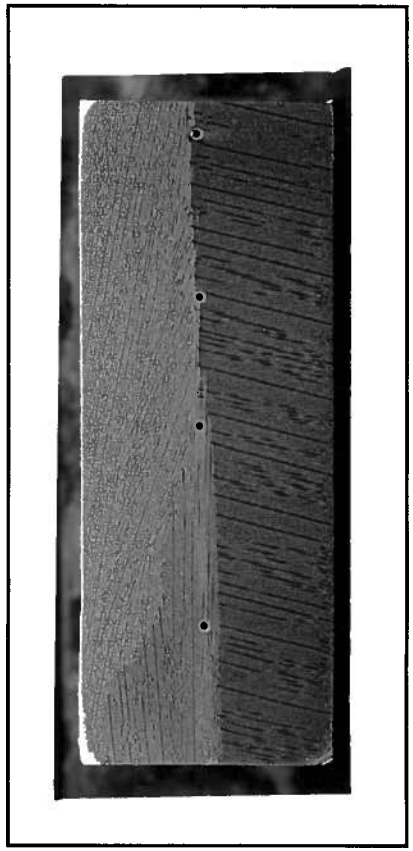

FIGURE 5.5c: SNECMA CET #8
Top Bar Section: From 172 mm
to 223 mm Above Copper Chill Plate

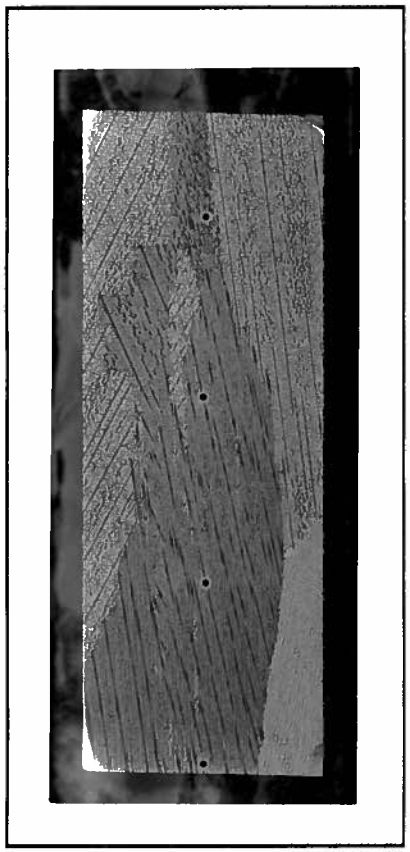

FIGURE 5.6a: SNECMA CET #9
Bottom Bar Section: From 64 mm
to 117 mm Above Copper Chill Plate

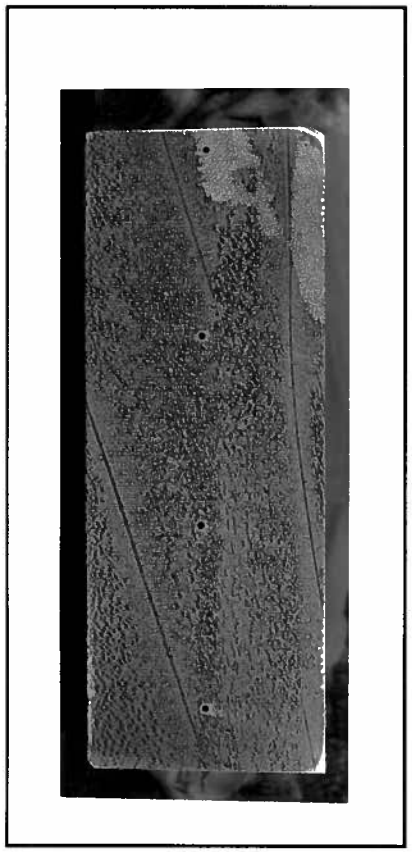

FIGURE 5.6b: SNECMA CET #9
Middle Bar Section: From 118 mm
to 170 mm Above Copper Chill Plate

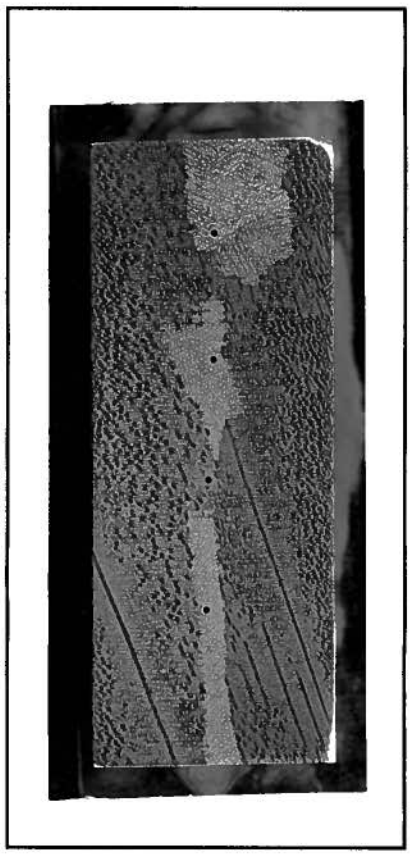

FIGURE 5.6c: SNECMA CET #9
Top Bar Section: From 171 mm
to 121 mm Above Copper Chill Plate

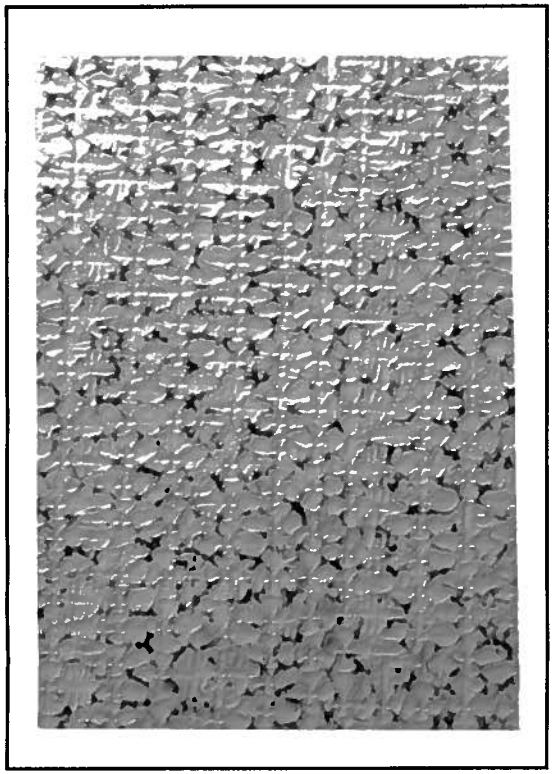

FIGURE 5.7a: SNECMA CET #2
Cross Section View of Bar at 72 mm
Above Copper Chill Plate
Magnification: 50 X

FIGURE 5.7b: SNECMA CET #2
Cross Section View of Bar at 118 mm
Above Copper Chill Plate
Magnification: 6.6 X

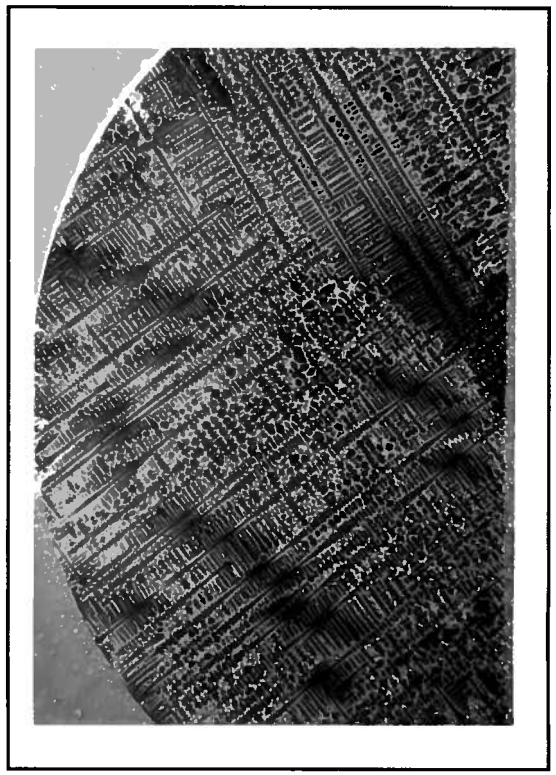

FIGURE 5.7c: SNECMA CET #2
Cross Section View of Bar at 178 mm
Above Copper Chill Plate
Magnification: 6.6 X

FIGURE 5.8a: SNECMA CET #6
Cross Section View of Bar at 71 mm
Above Copper Chill Plate
Magnification: 6.6 X

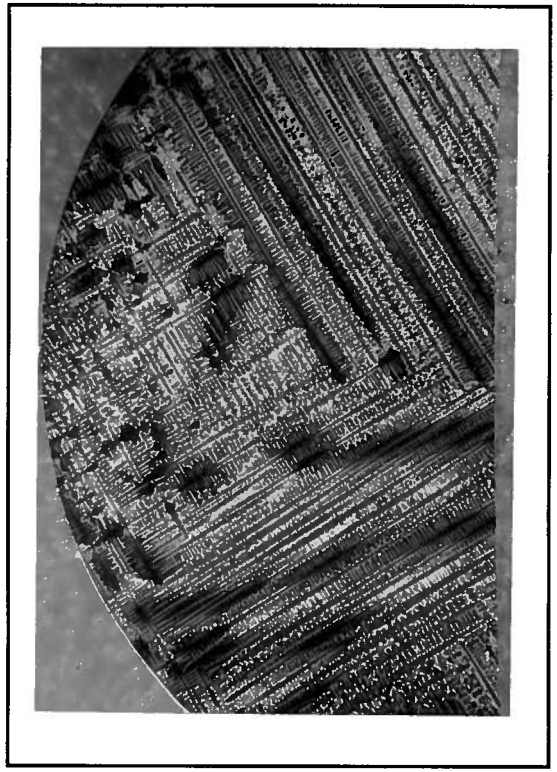

FIGURE 5.8b: SNECMA CET #6
Cross Section View of Bar at 129 mm
Above Copper Chill Plate
Magnification: 6.6 X

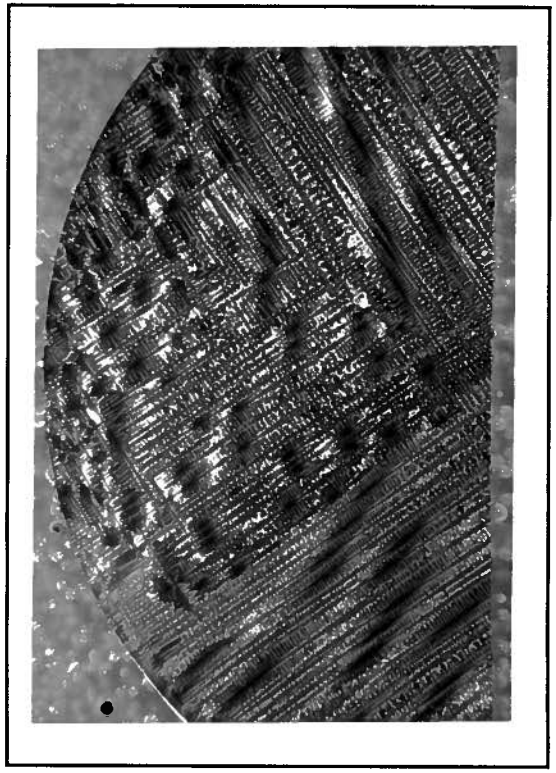

FIGURE 5.8c: SNECMA CET #6
Cross Section View of Bar at 182 mm
Above Copper Chill Plate
Magnification: 6.6 X

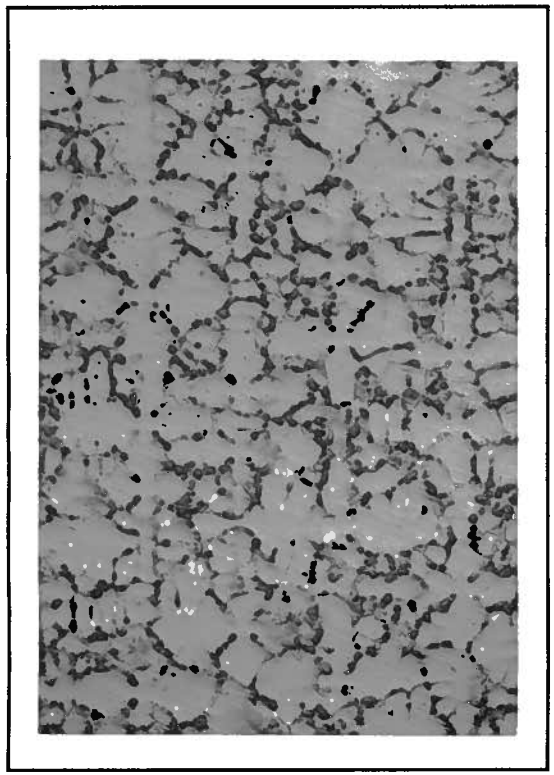

FIGURE 5.9a: SNECMA CET #9
Cross Section View of Bar at 71 mm
Above Copper Chill Plate
Magnification: 50 X

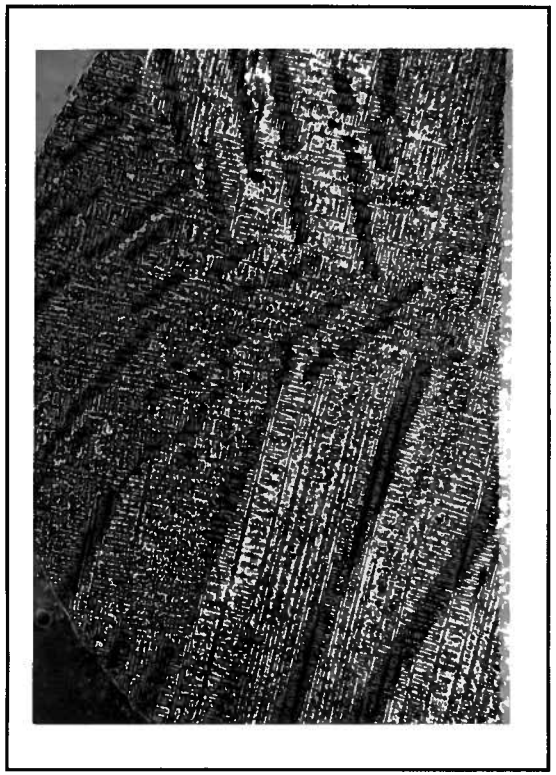

FIGURE 5.9b: SNECMA CET #9
Cross Section View of Bar at 125 mm
Above Copper Chill Plate
Magnification: 6.6 X

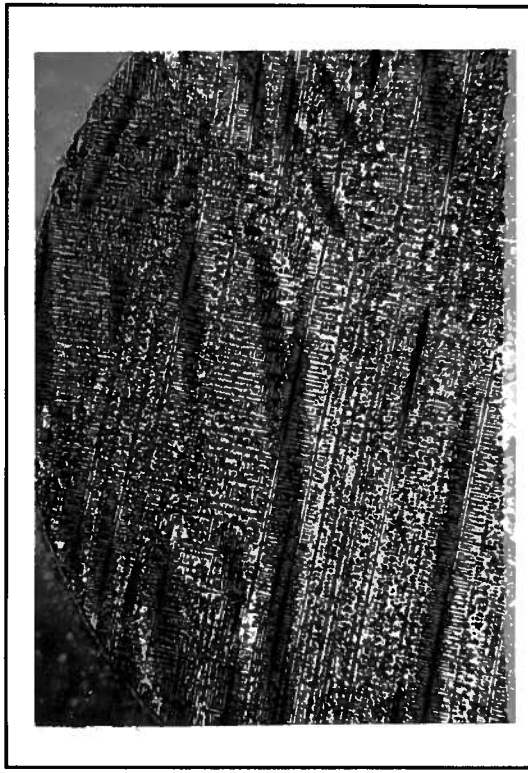

FIGURE 5.9c: SNECMA CET #9
Cross Section View of Bar at 179 mm
Above Copper Chill Plate
Magnification: 6.6 X

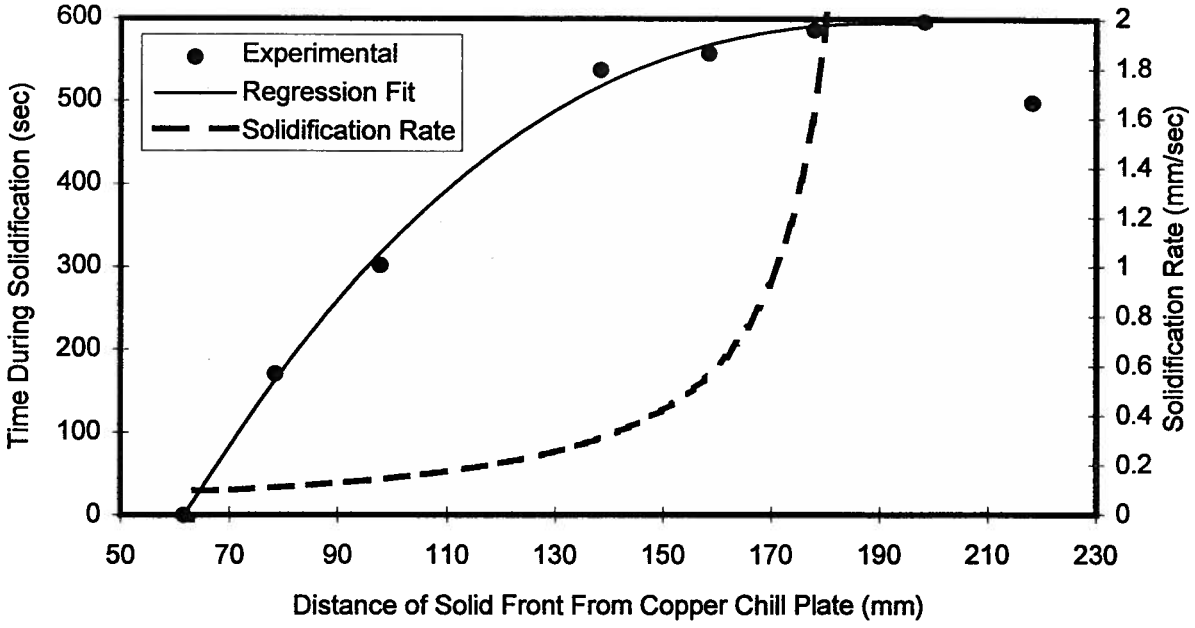

Figure 5.10a: Solid Front Position and Solidification Rate During SNECMA CET#5 With AM1

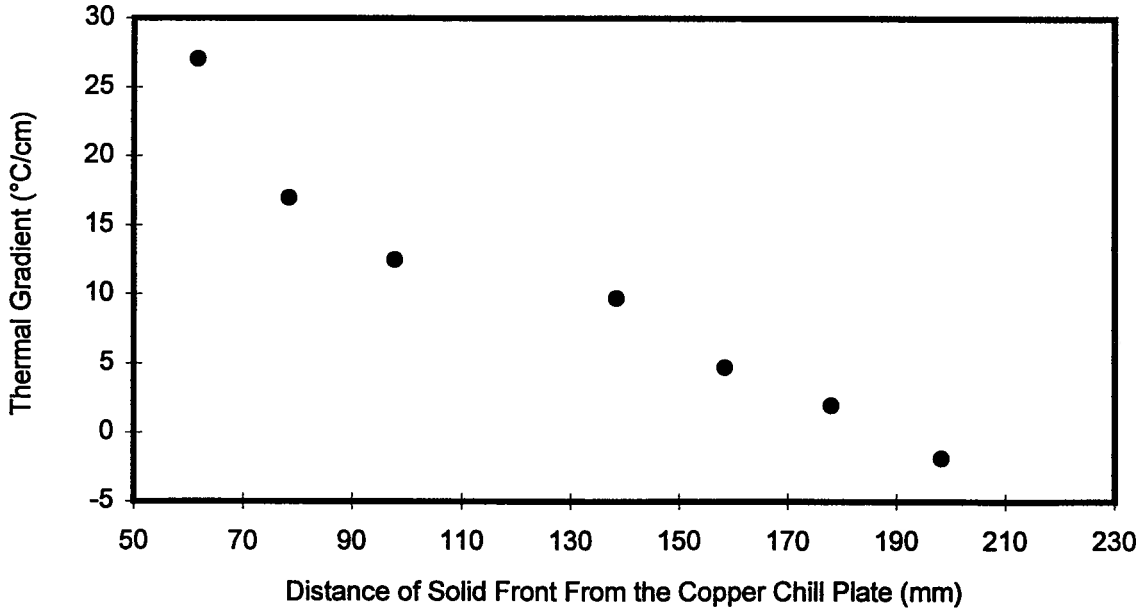

Figure 5.10b: Thermal Gradient at Solid Front During SNECMA CET#2 With AM1

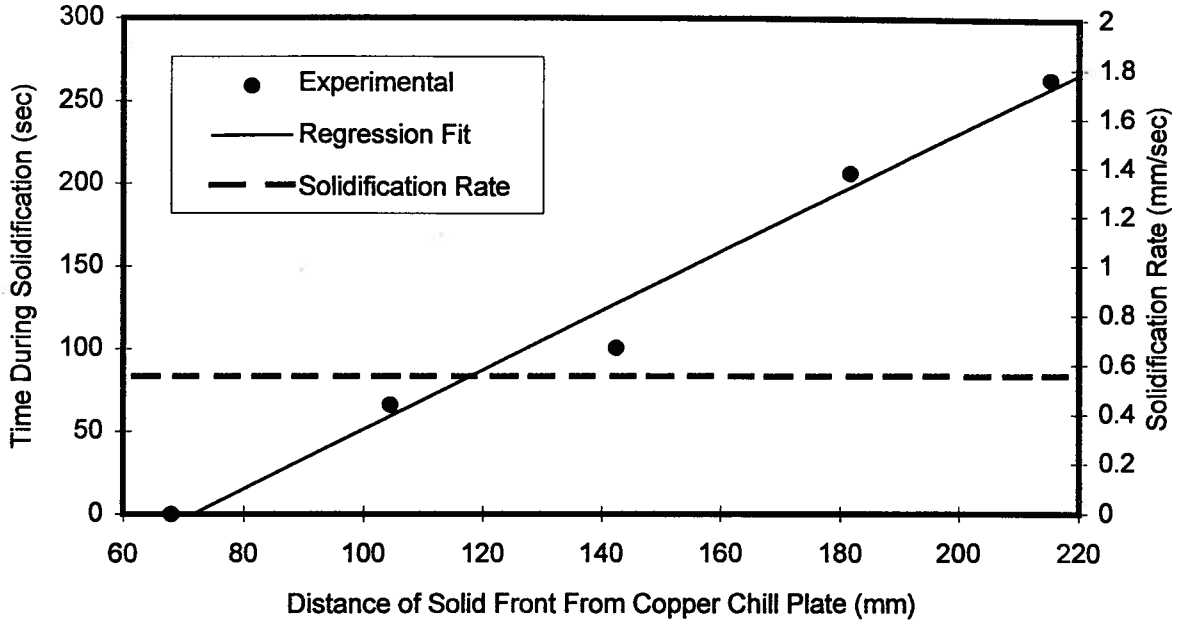

Figure 5.11a: Solid Front Position and Solidification Rate During SNECMA CET#4 With AM1

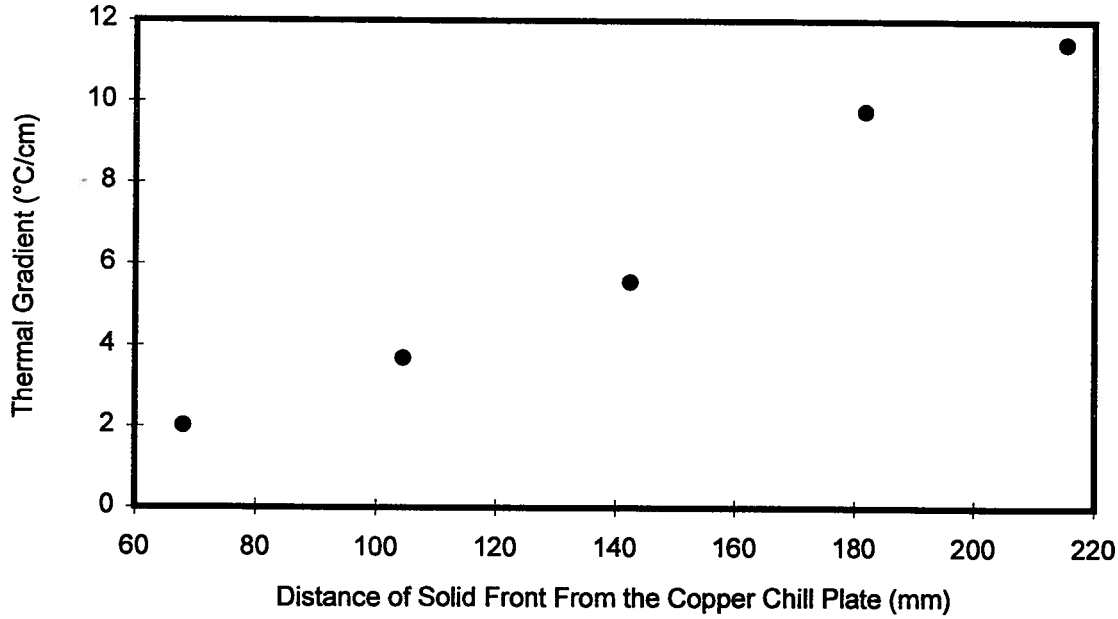

Figure 5.11b: Thermal Gradient at Solid Front During SNECMA CET#4 With AM1

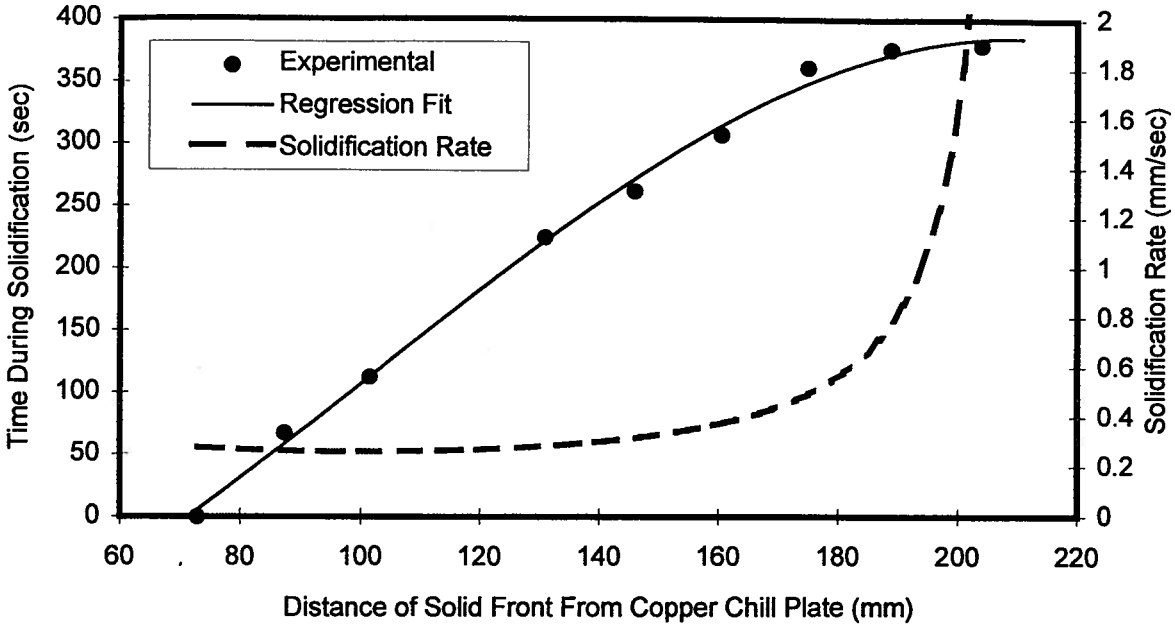

Figure 5.12a: Solid Front Position and Solidification Rate During SNECMA CET#5 With AM1

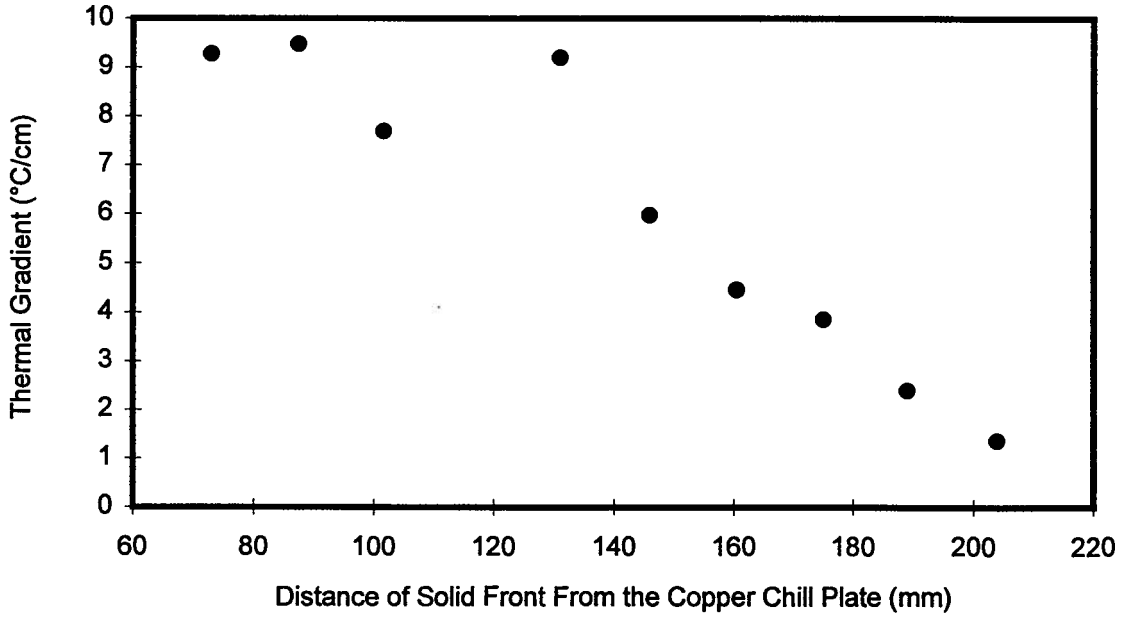

Figure 5.12b: Thermal Gradient at Solid Front During SNECMA CET#5 With AM1

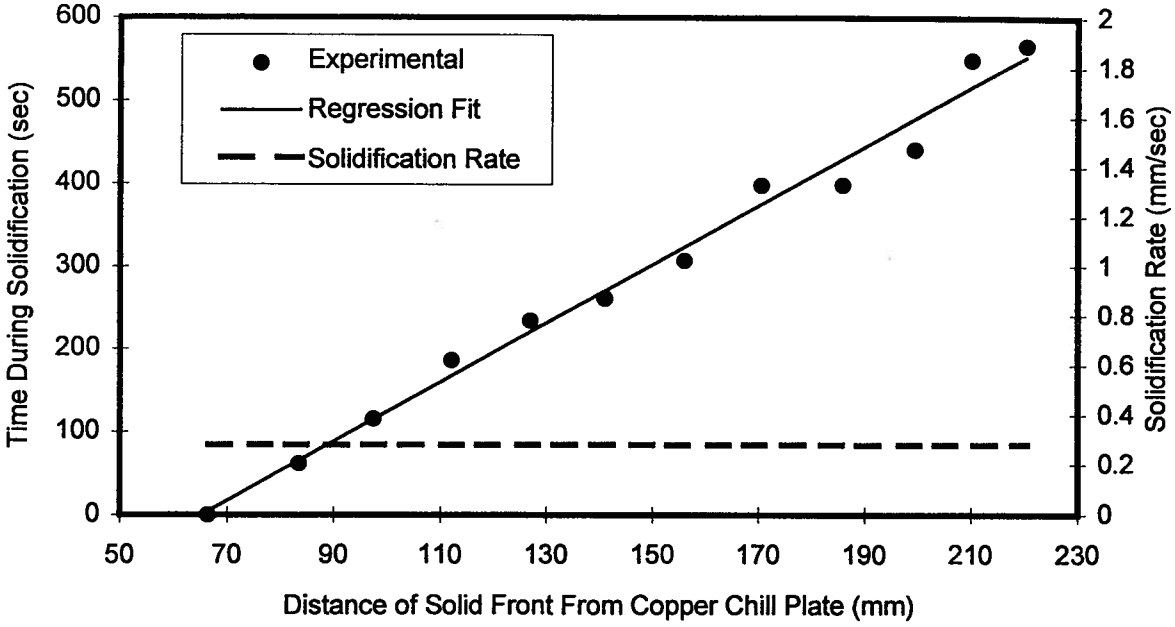

Figure 5.13a: Solid Front Position and Solidification Rate During SNECMA CET#6 With AM1

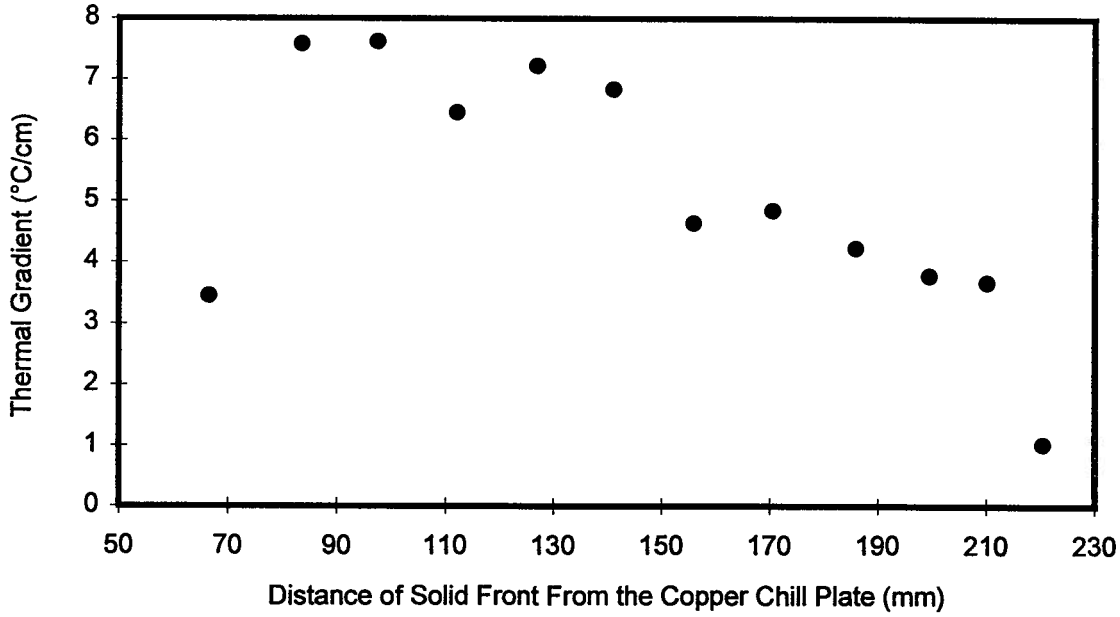

Figure 5.13b: Thermal Gradient at Solid Front During SNECMA CET#6 With AM1

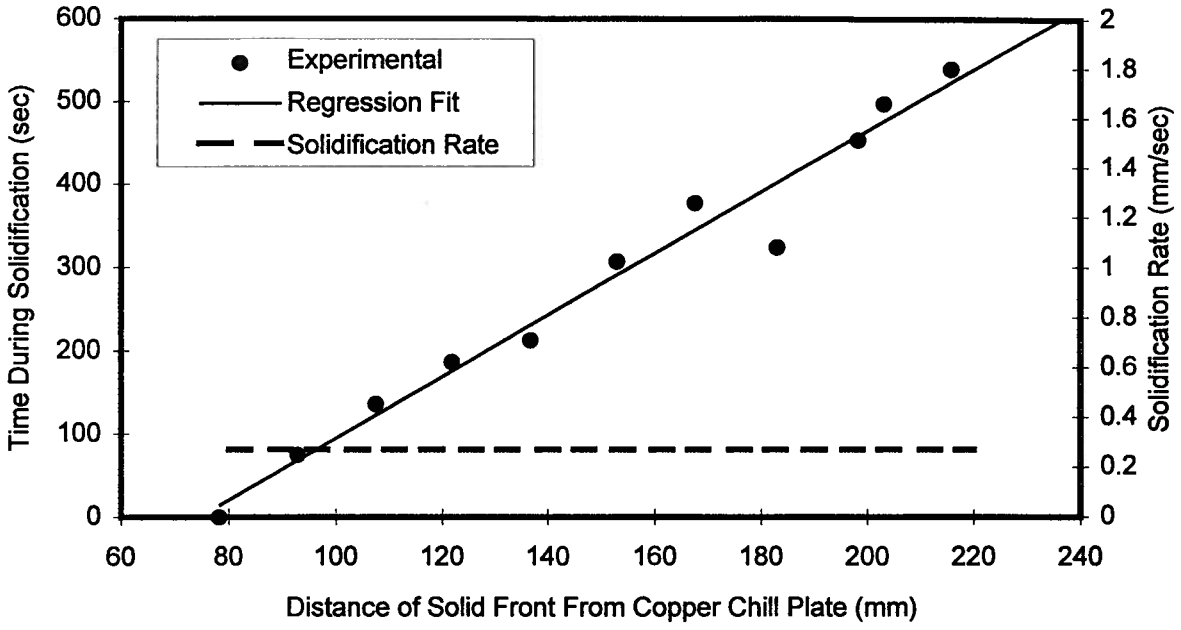

Figure 5.14a: Solid Front Position and Solidification Rate During SNECMA CET#8 With MAR-M200+Hf

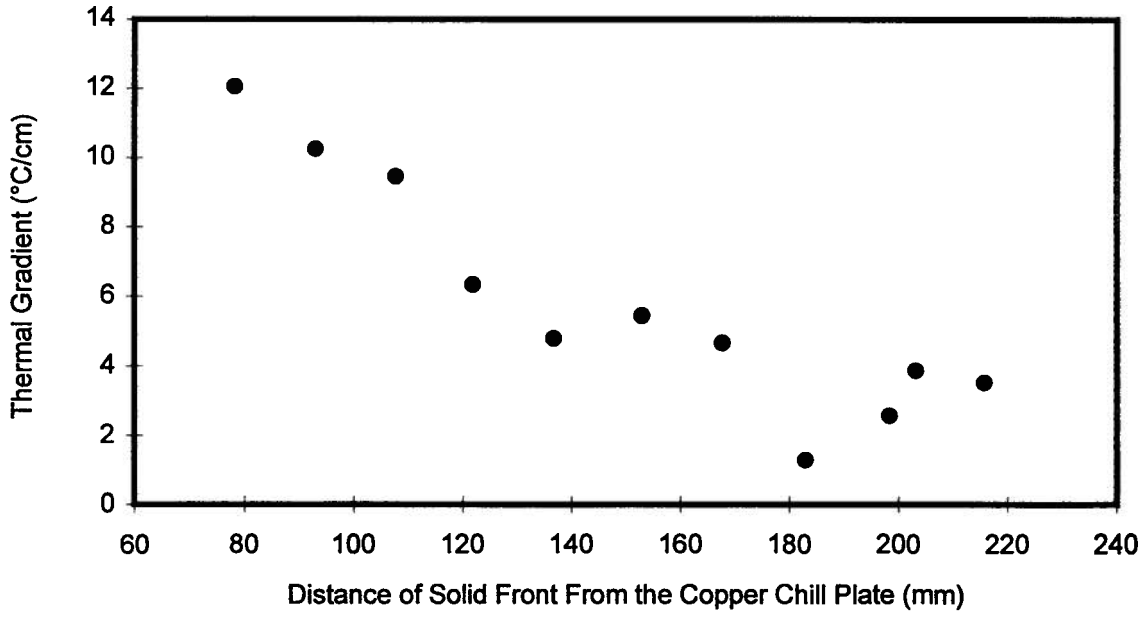

Figure 5.14b: Thermal Gradient at Solid Front During SNECMA CET#8 With MAR-M200+Hf

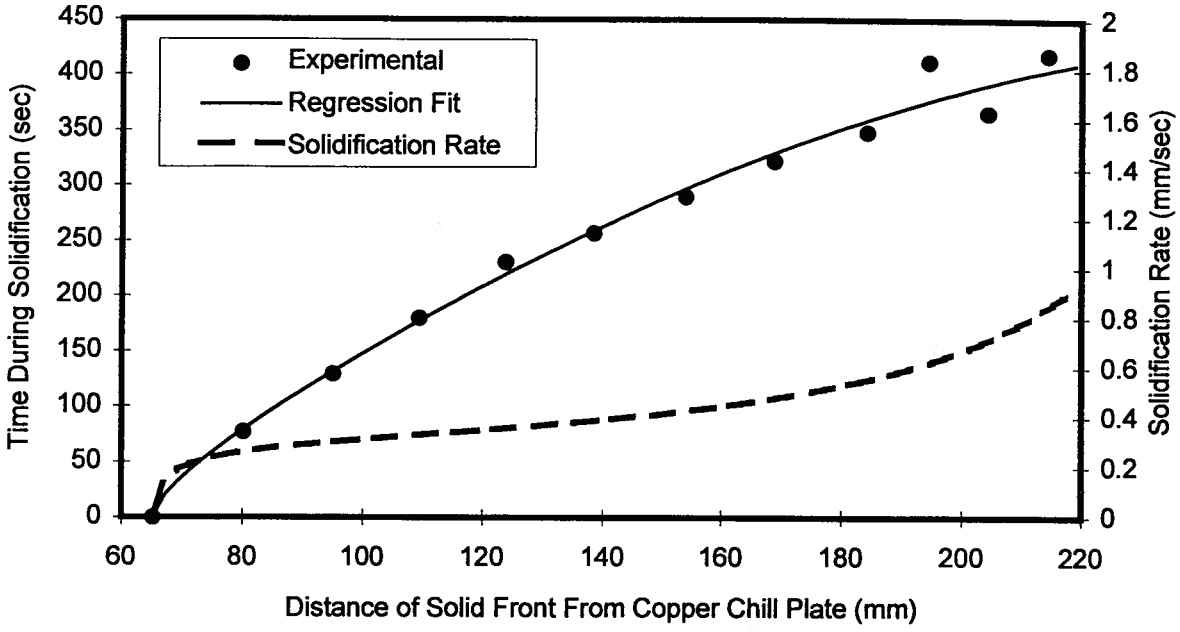

Figure 5.15a: Solid Front Position and Solidification Rate During SNECMA CET#9 With MAR-M200+Hf

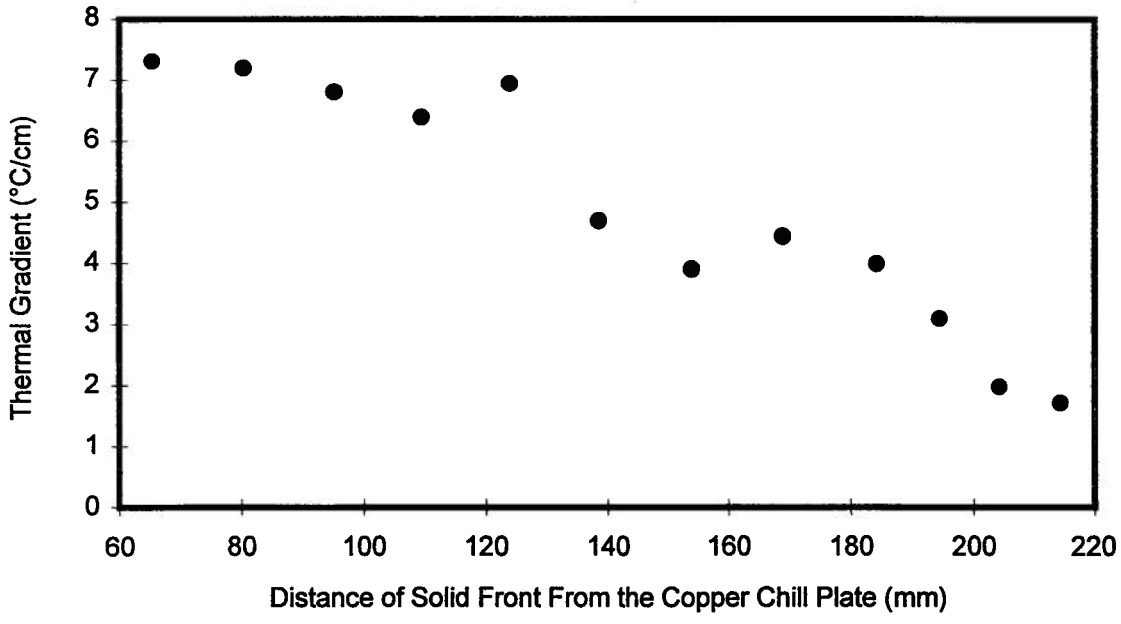

Figure 5.15b: Thermal Gradient at Solid Front During SNECMA CET#9 With MAR-M200+Hf

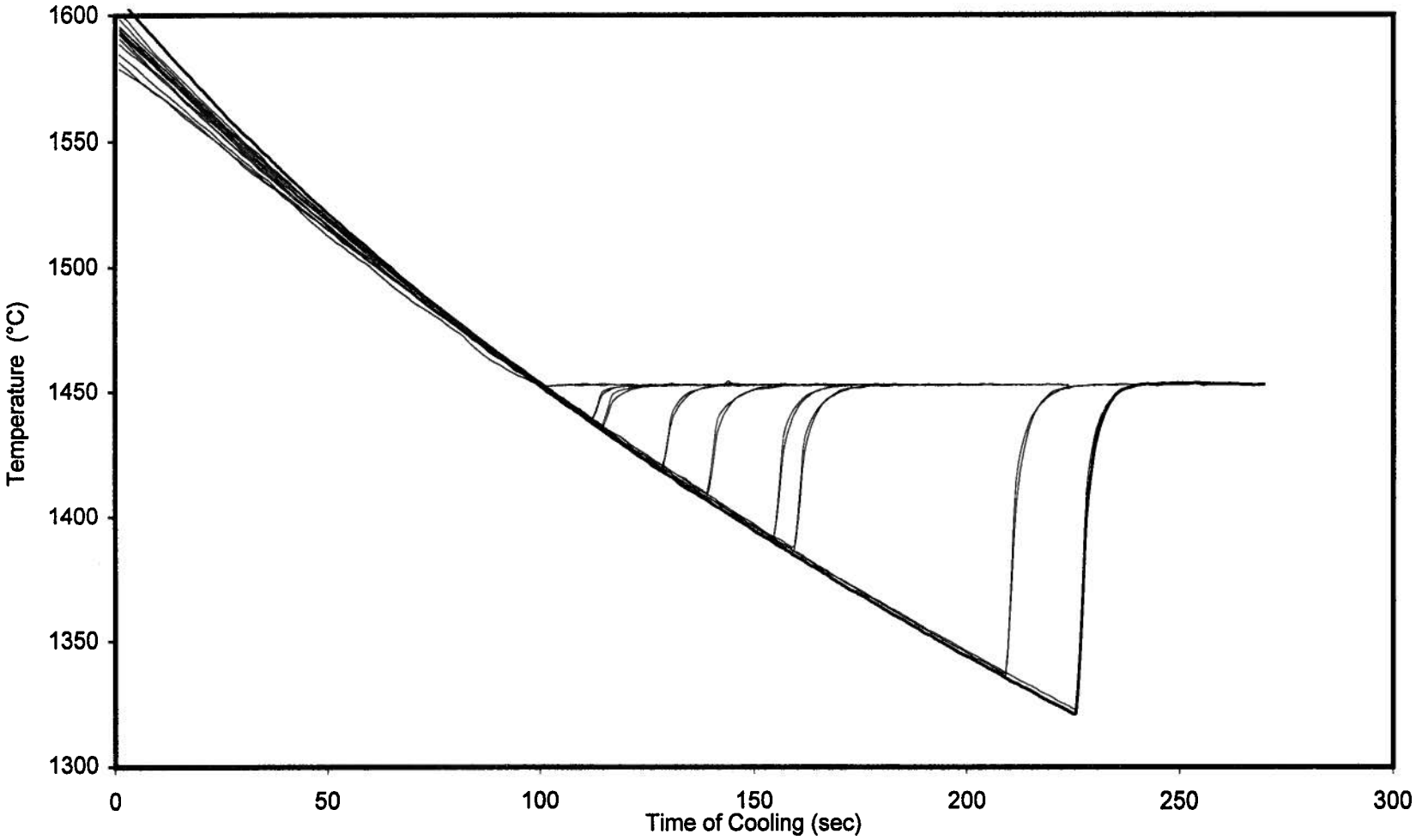

Figure 5.16
Thermocouple Response
to Recalescence in Undercooled Pure Nickel

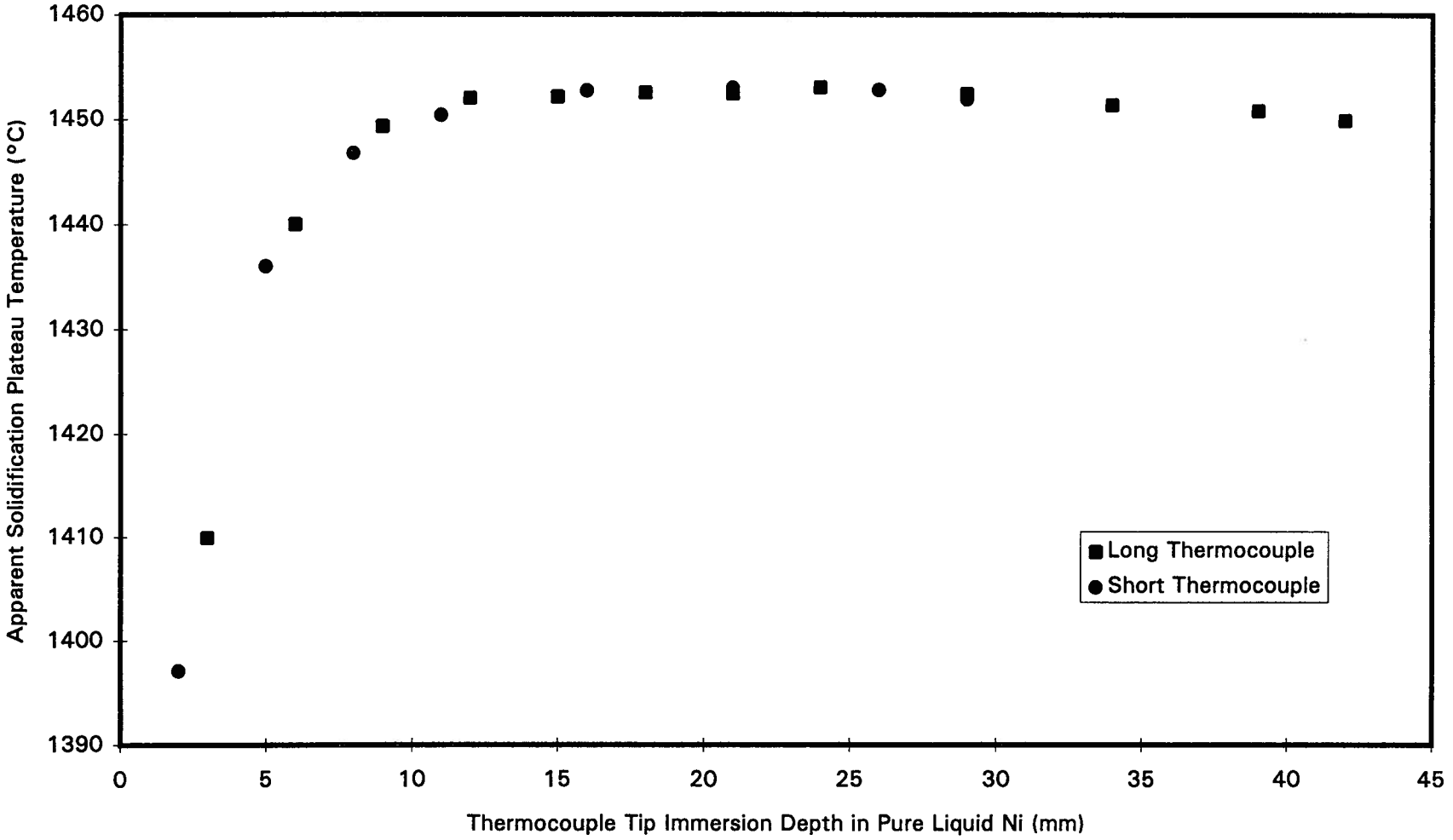

Figure 5.17
Effect of Thermocouple Tip Immersion Depth on
Apparent Solidification Plateau Temperature of Pure Ni

FIGURE 5.18

Experiment AMCETB With EB Refined AM1

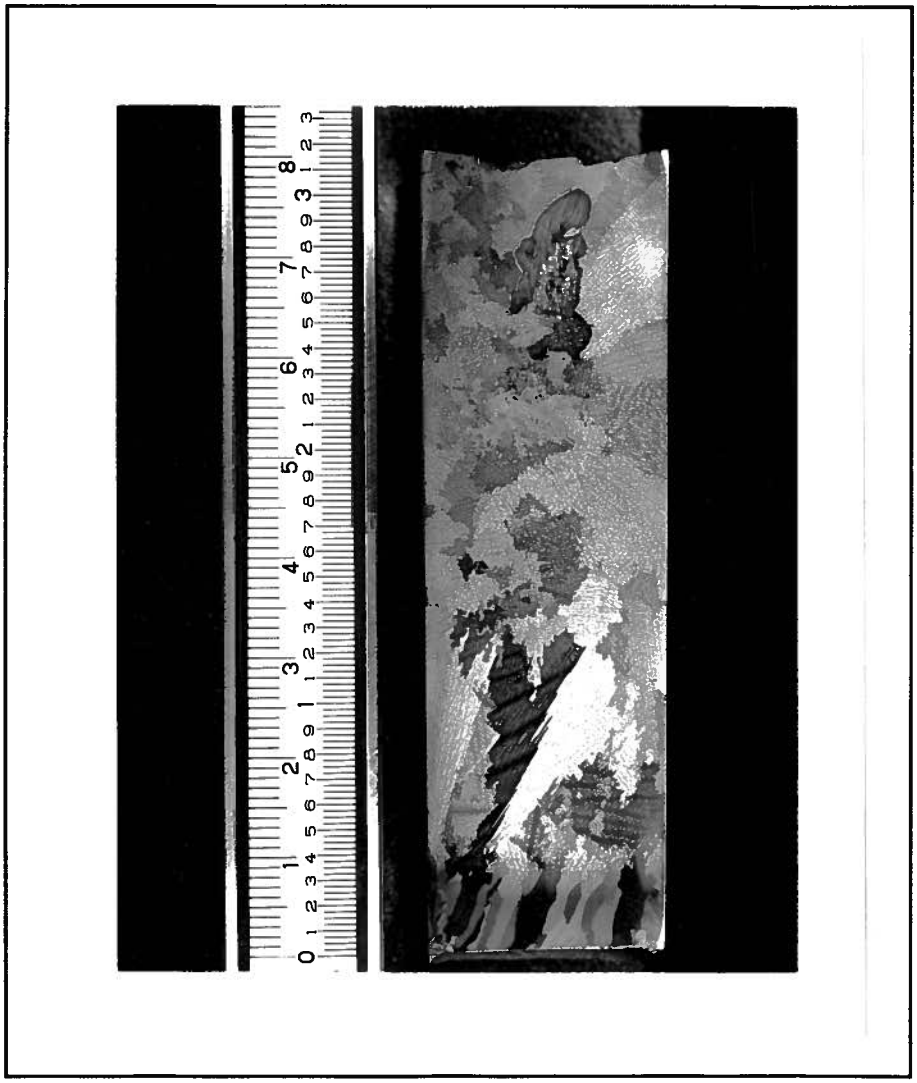

FIGURE 5.19

Experiment AMCETC With EB Refined AM1

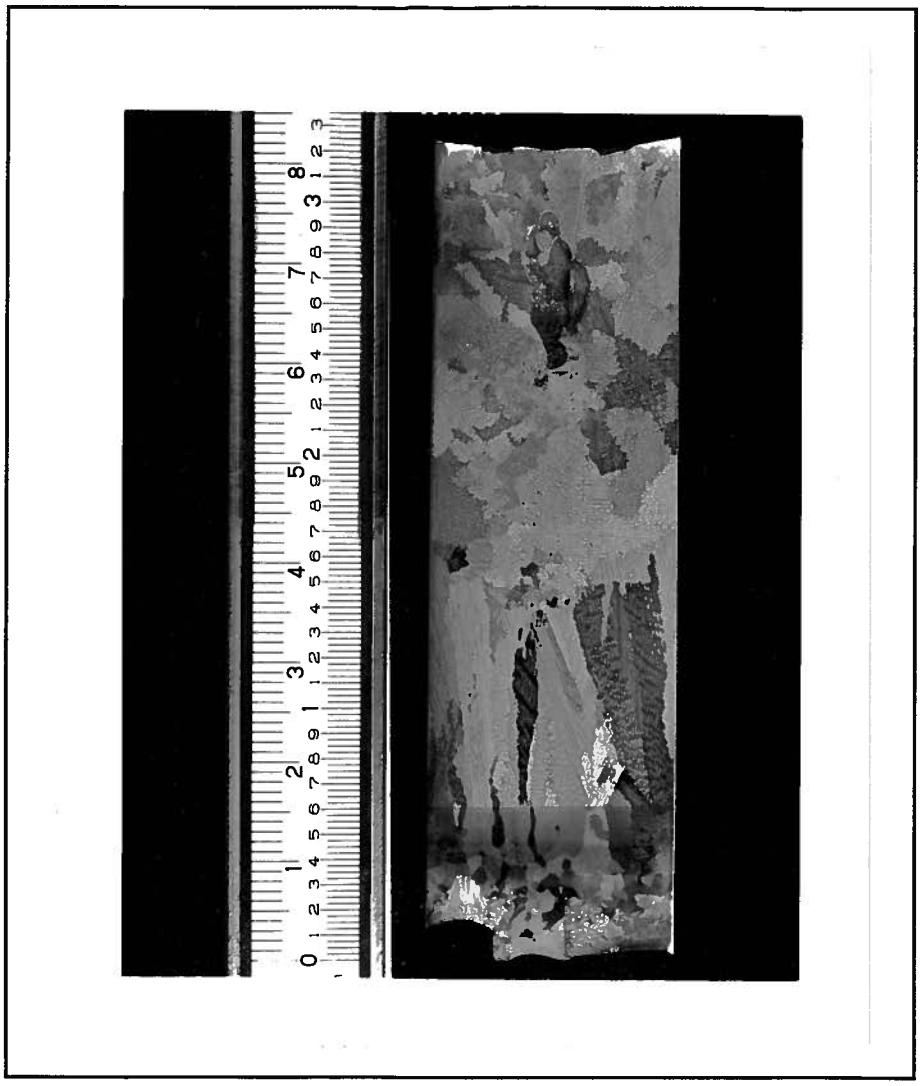

FIGURE 5.20

Experiment AMCETD With EB Refined AM1

FIGURE 5.21

Experiment AMCETE With EB Refined AM1

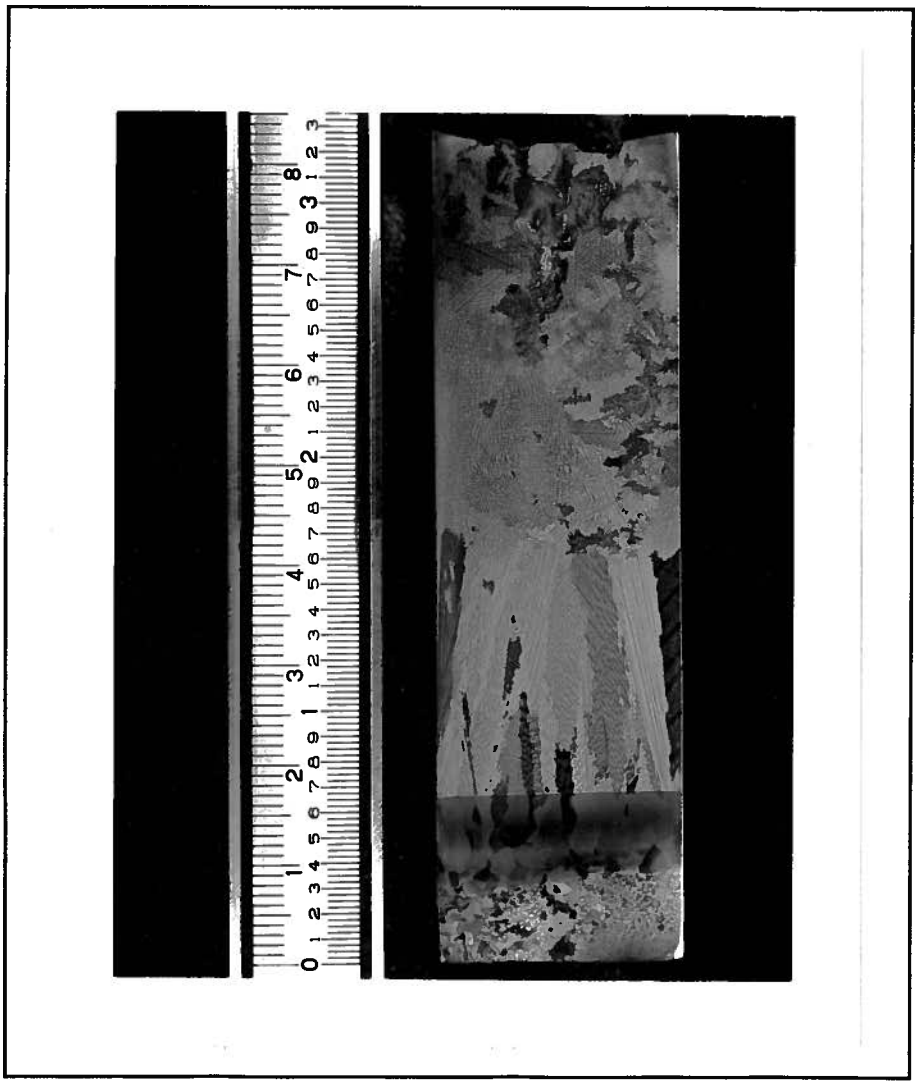

FIGURE 5.22

Experiment AMCETF With EB Refined AM1

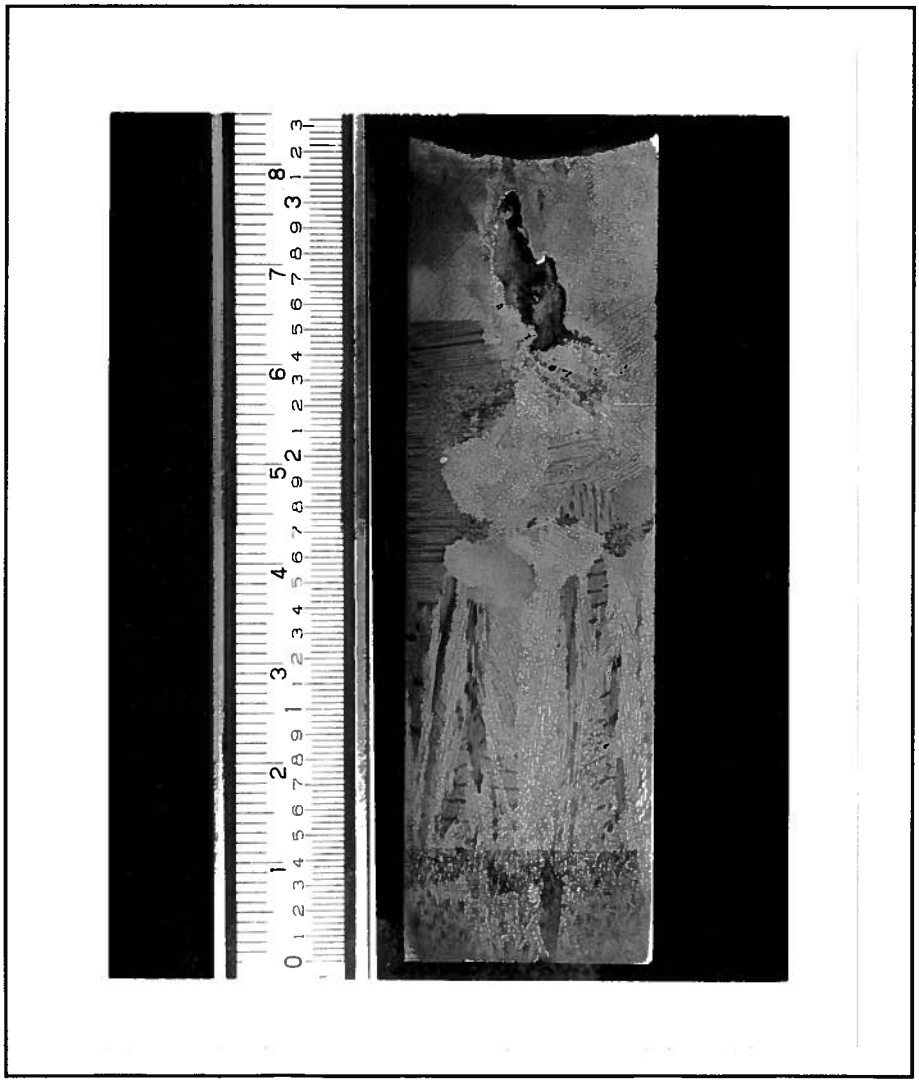

FIGURE 5.23

Experiment MRCETB With MAR-M200+Hf

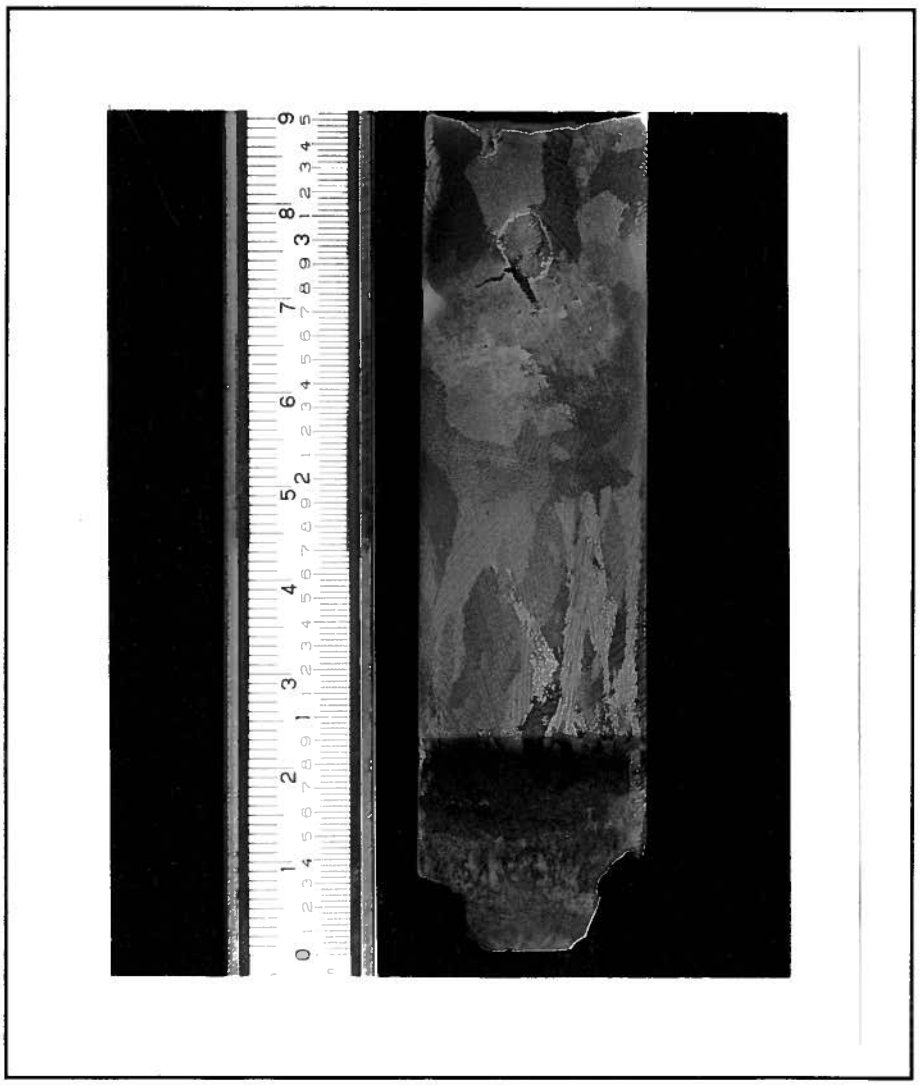

FIGURE 5.24

Experiment MRCETC With MAR-M200+Hf

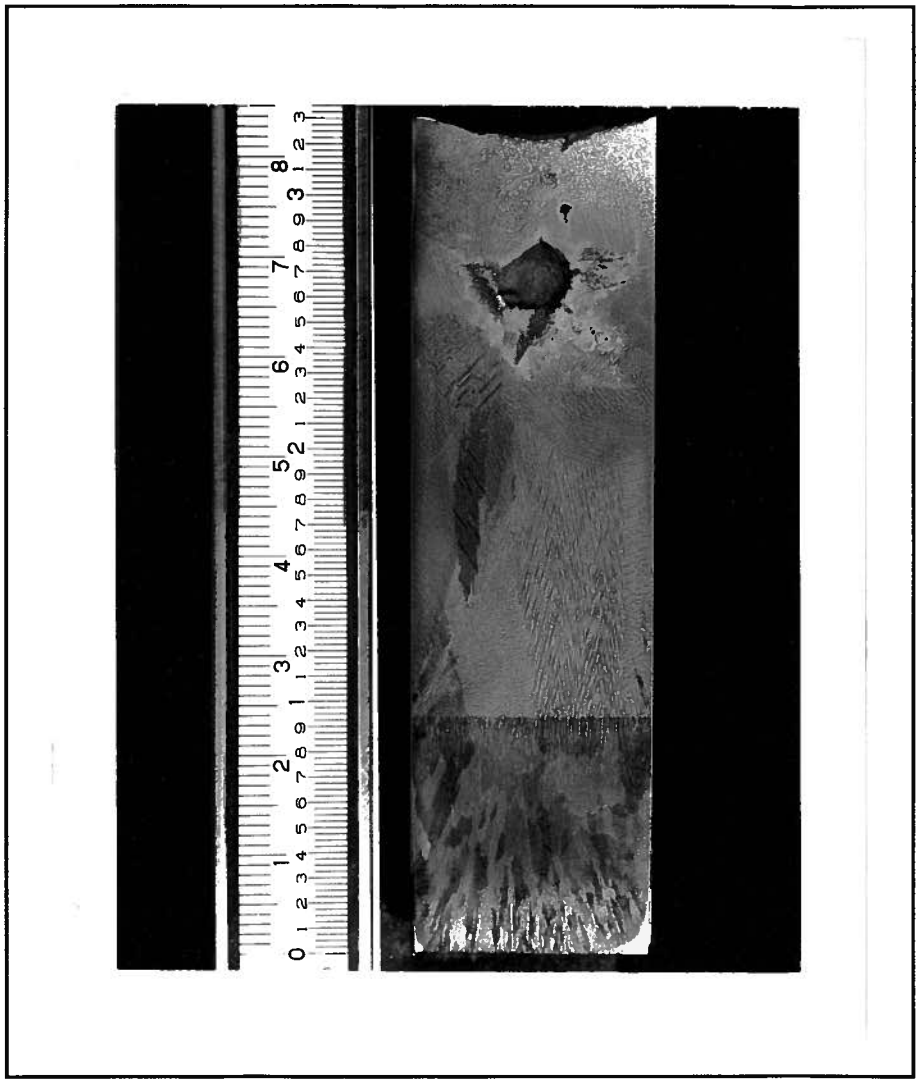

FIGURE 5.25

Experiment MRCETD With MAR-M200+Hf

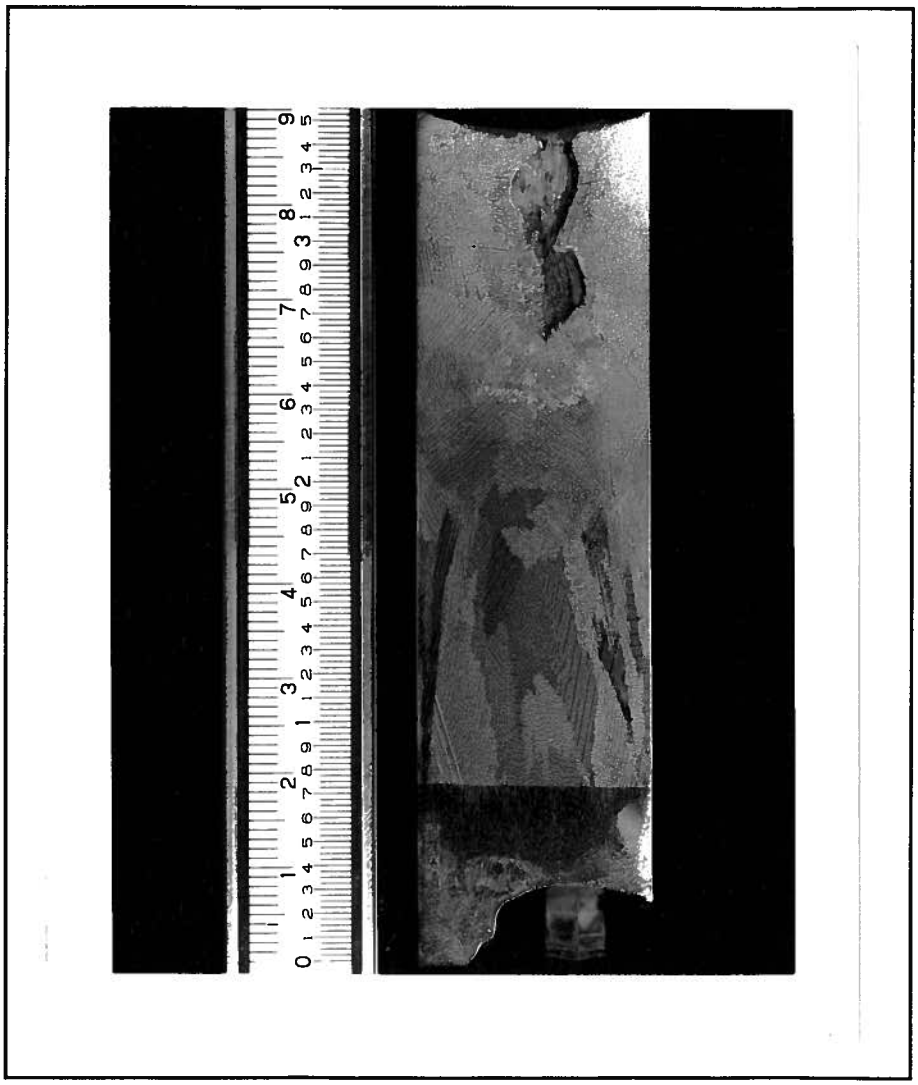

FIGURE 5.26

Experiment MRCETE With MAR-M200+Hf

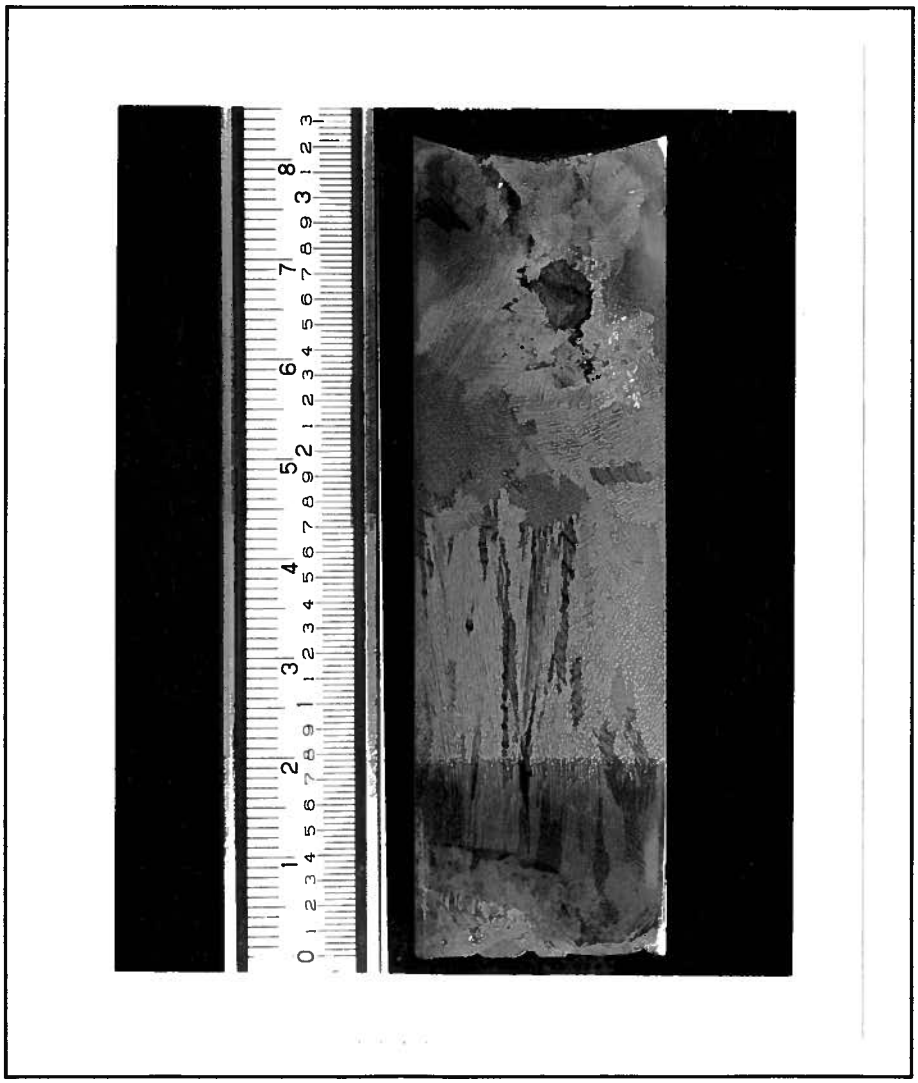

FIGURE 5.27

Experiment MRCETF With MAR-M200+Hf

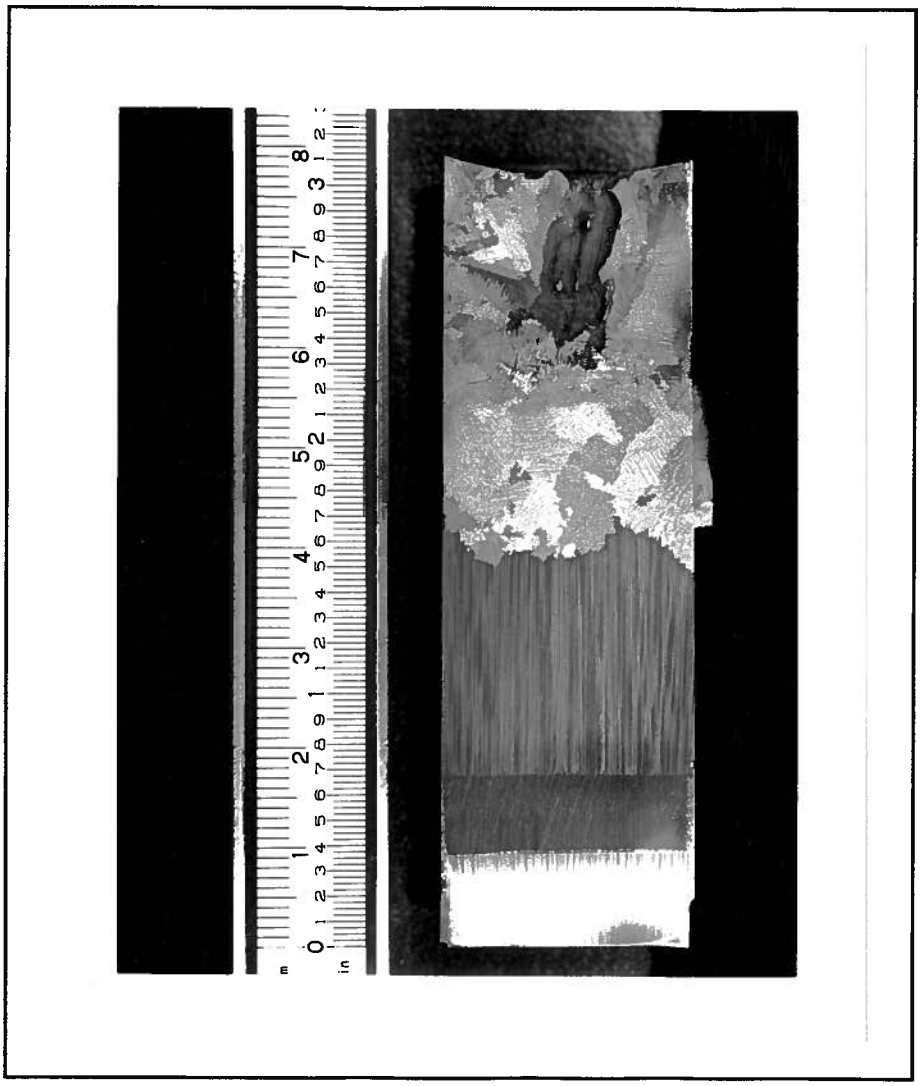

FIGURE 5.28

Experiment AMSX90 With Normal AM1
and Seed in (100) Direction

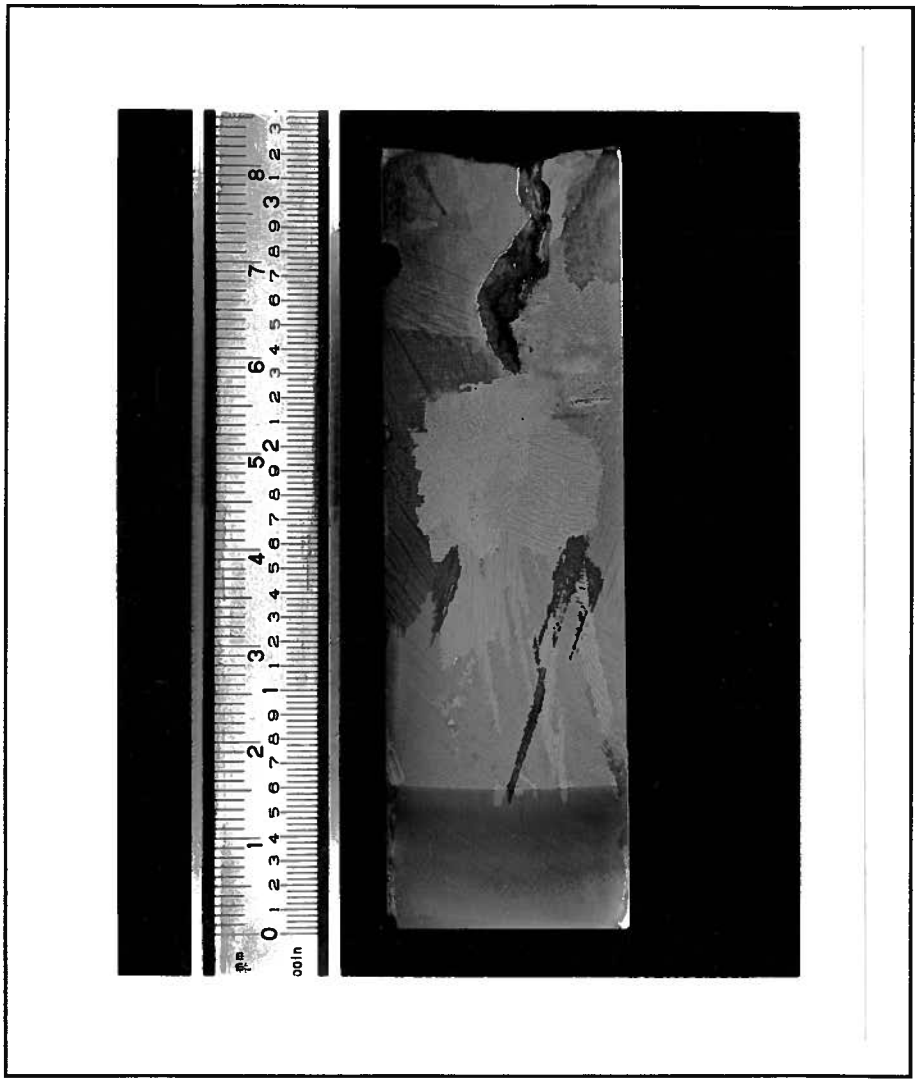

FIGURE 5.29

Experiment AMSX45 With Normal AM1
and Seed With <100> at 45° to the Vertical

FIGURE 5.30

Experiment AMNORM With Normal AM1

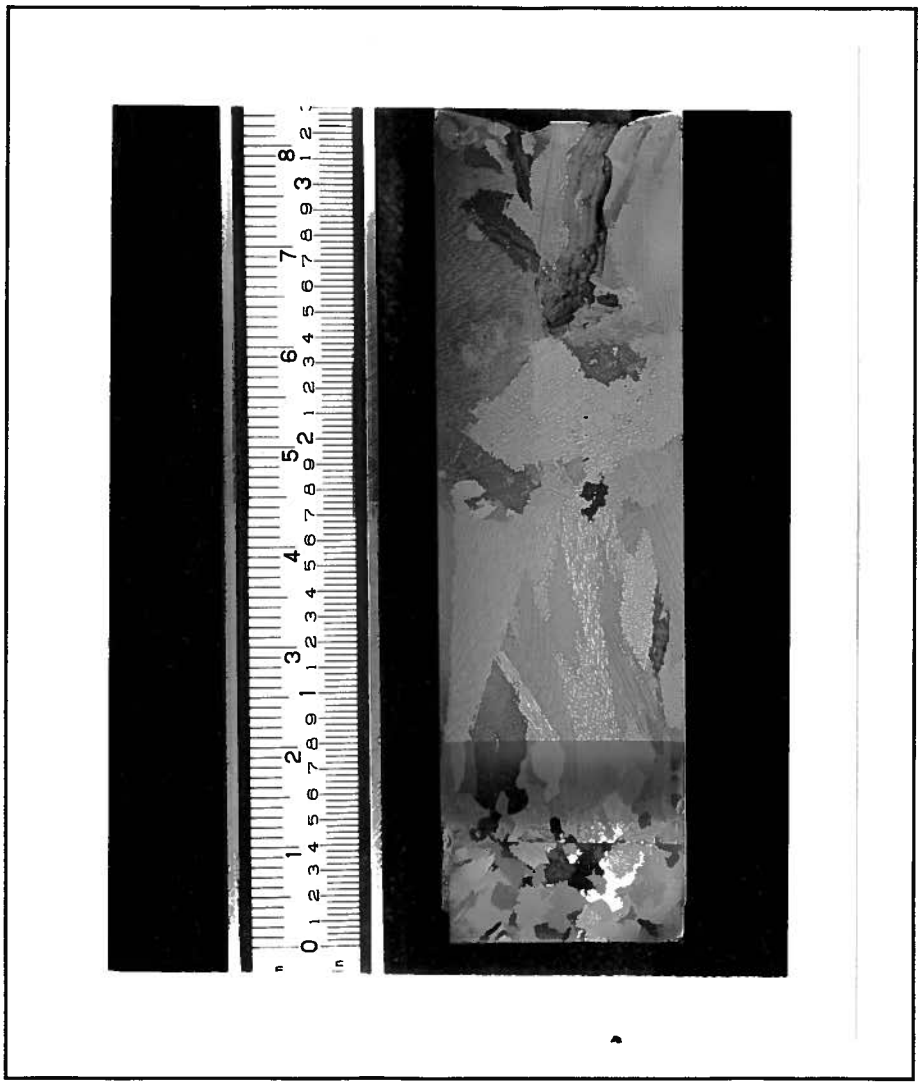

FIGURE 5.31

Experiment AMTIN With Normal AM1
and 1.3 g TiN Powder Added

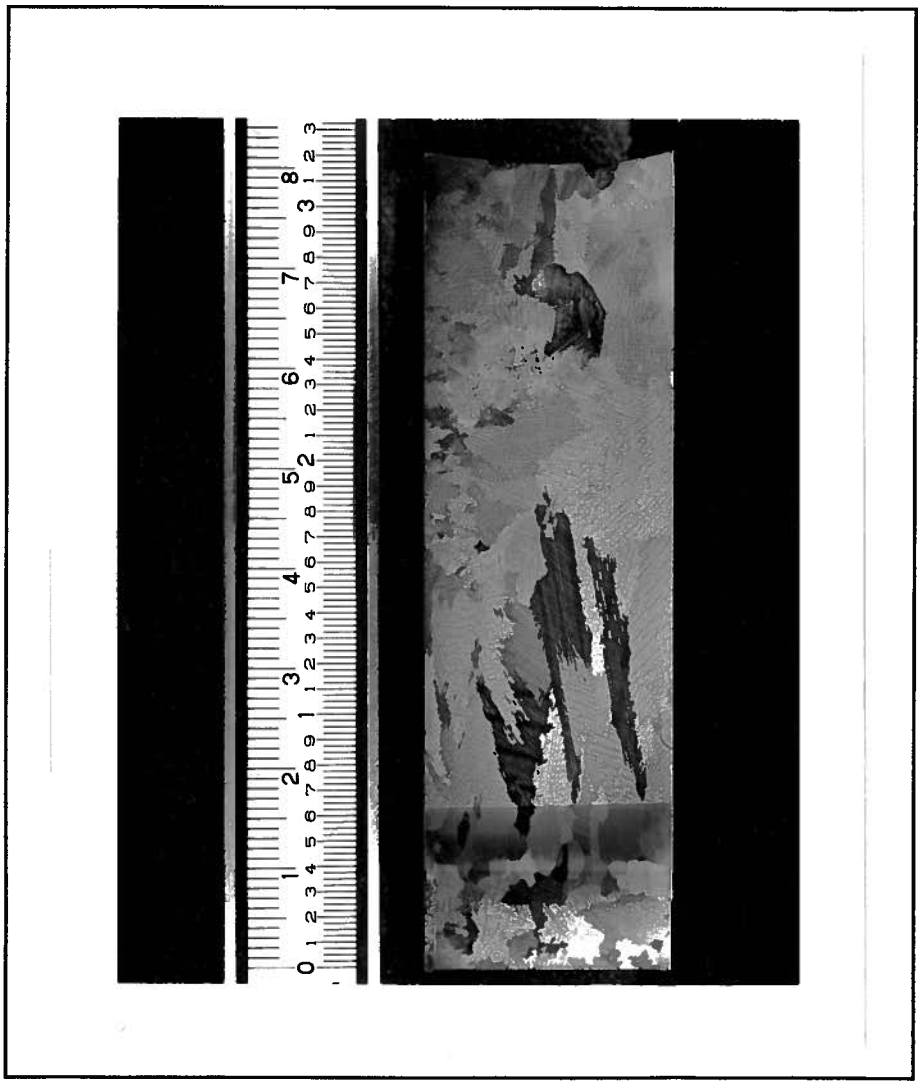

FIGURE 5.32

Experiment AMMGAL With Normal AM1
and 1.0 g $MgAl_2O_4$ + 1.0 g $CaAl_2O_4$ Added

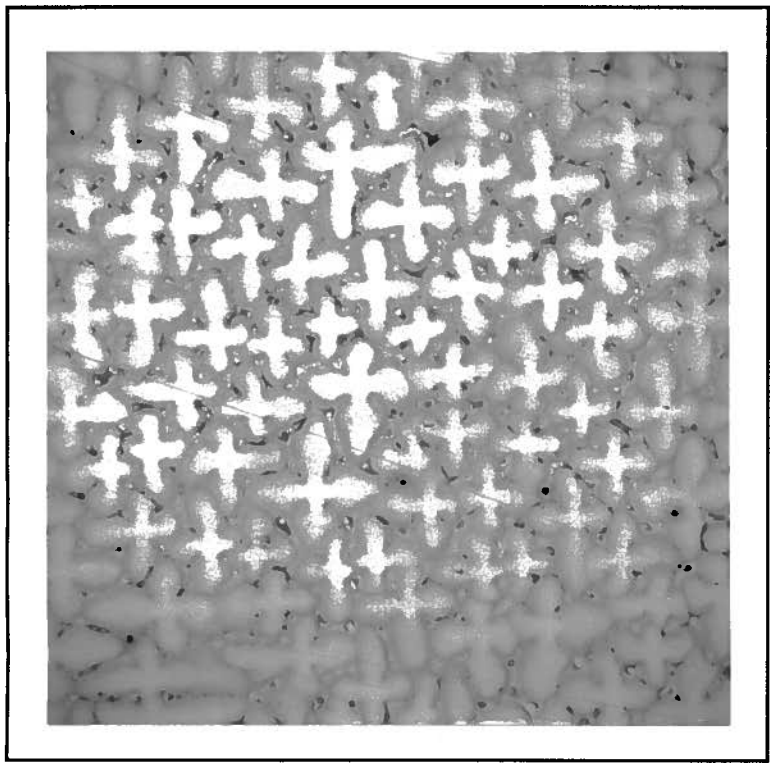

FIGURE 5.33a
Cross Section of Sample AMSX90
at 20 mm From the Steel Chill Plate
Magnification 50X

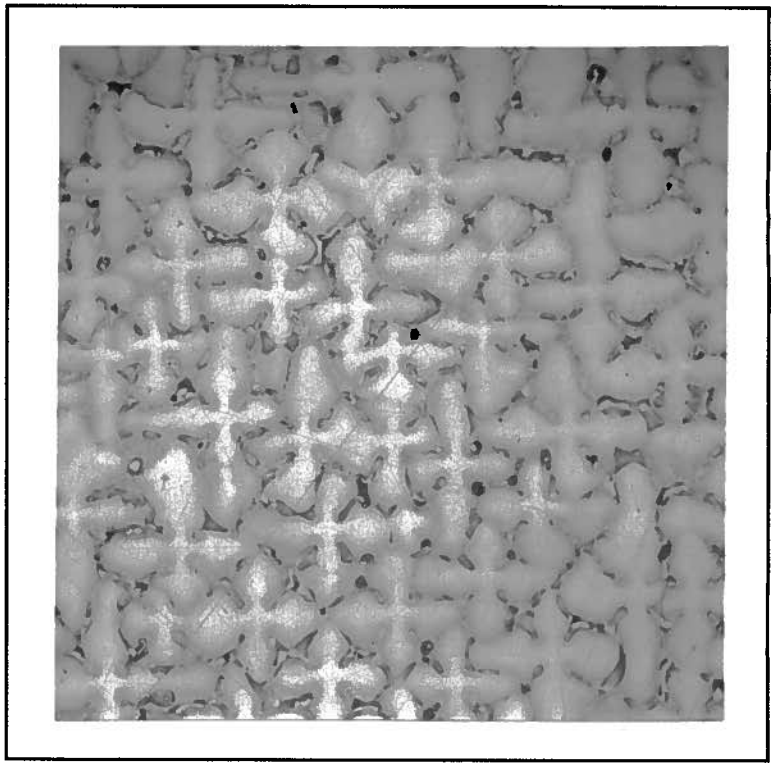

FIGURE 5.33b
Cross Section of Sample AMSX90
at 37.5 mm From the Steel Chill Plate
Magnification 50X

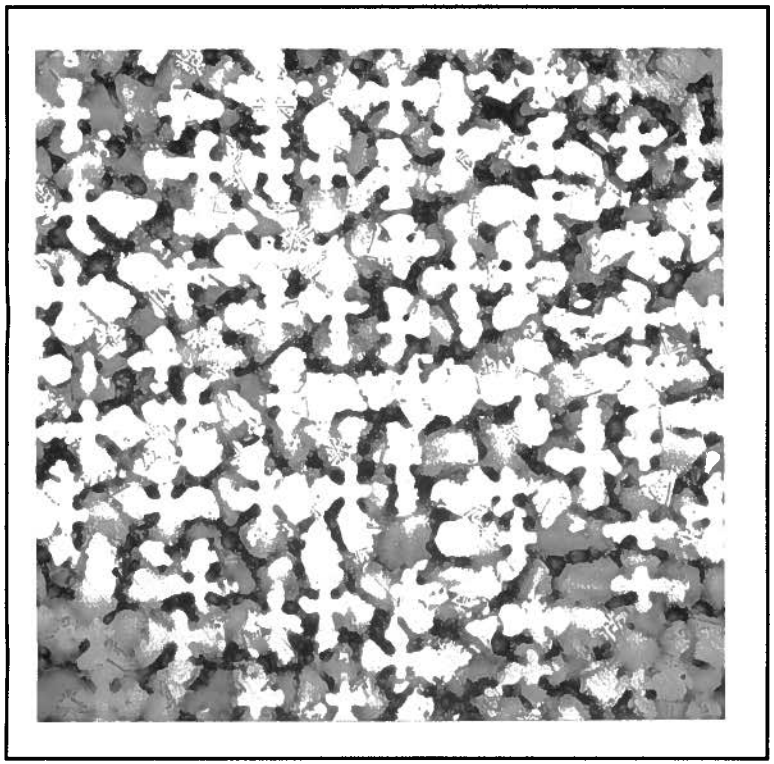

FIGURE 5.34a
Cross Section of Sample MRCETD
at 28.5 mm From the Steel Chill Plate
Magnification 50X

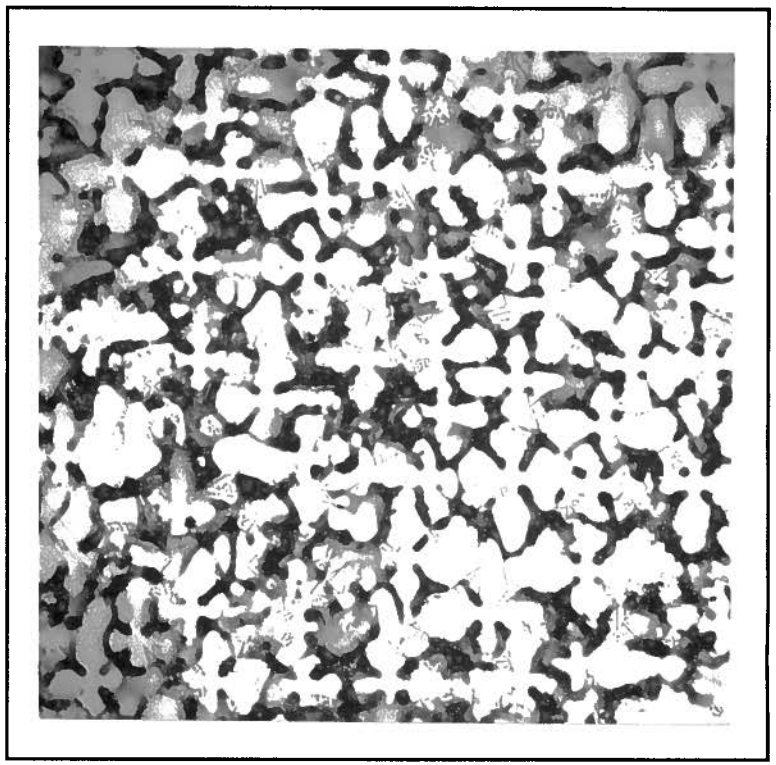

FIGURE 5.34b
Cross Section of Sample MRCETD
at 49.5 mm From the Steel Chill Plate
Magnification 50X

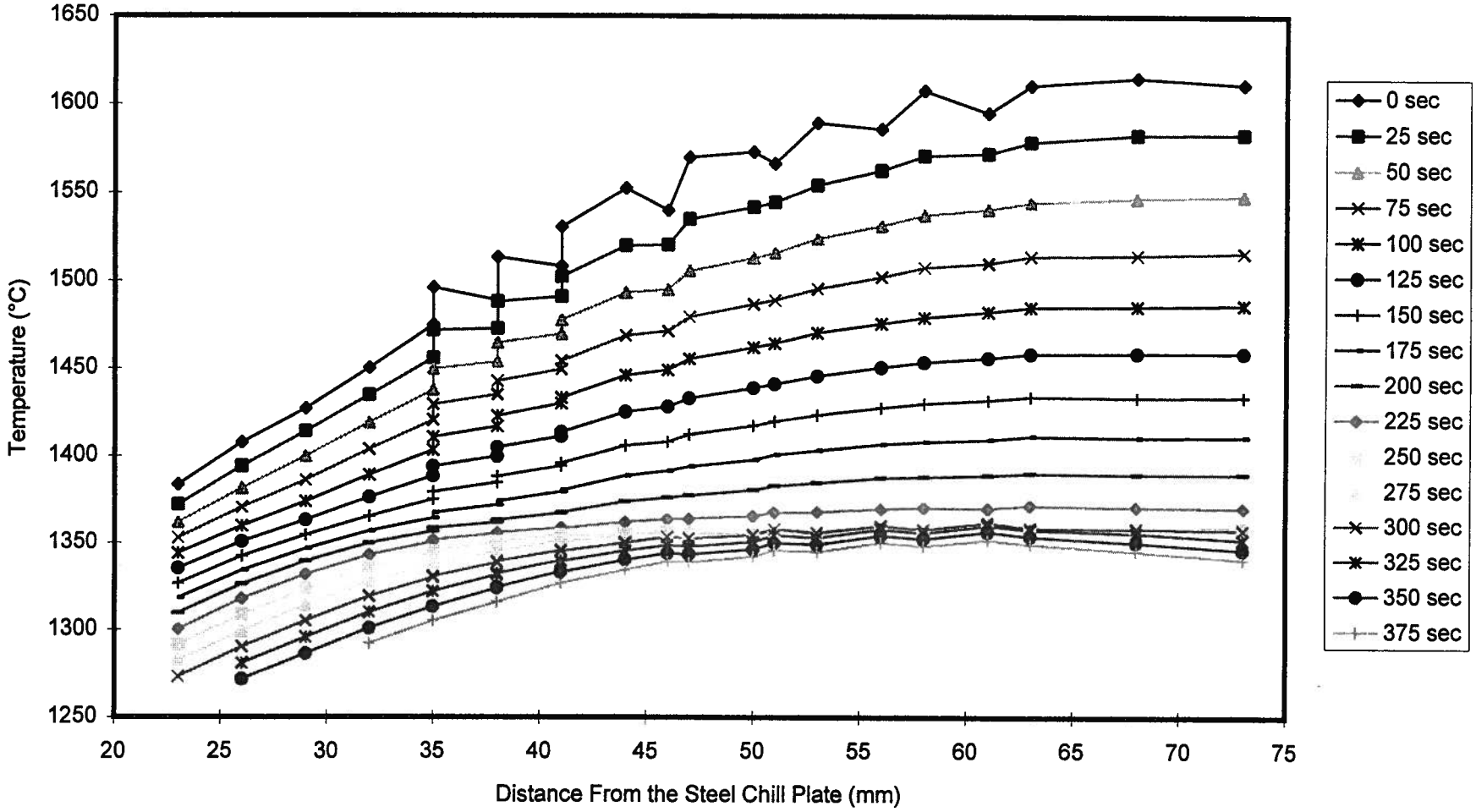

Figure 5.35
Thermal Profiles Recorded Every 25 Seconds
in CET Experiment "F" with MAR-M200+Hf

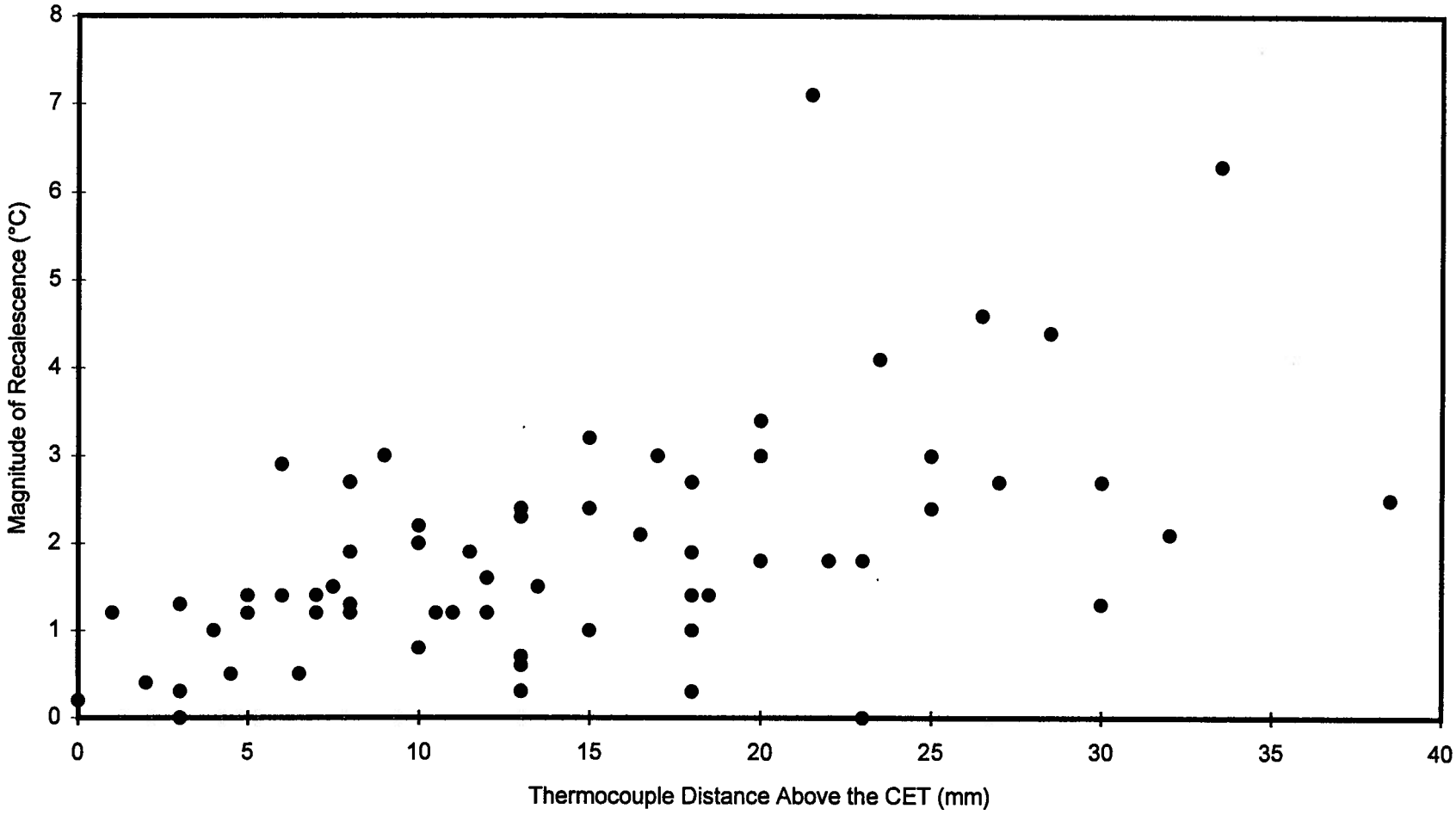

Figure 5.36
Magnitude of Recalescence vs Distance From the CET
in MRCET Series of Experiments With MAR-M200 + Hf

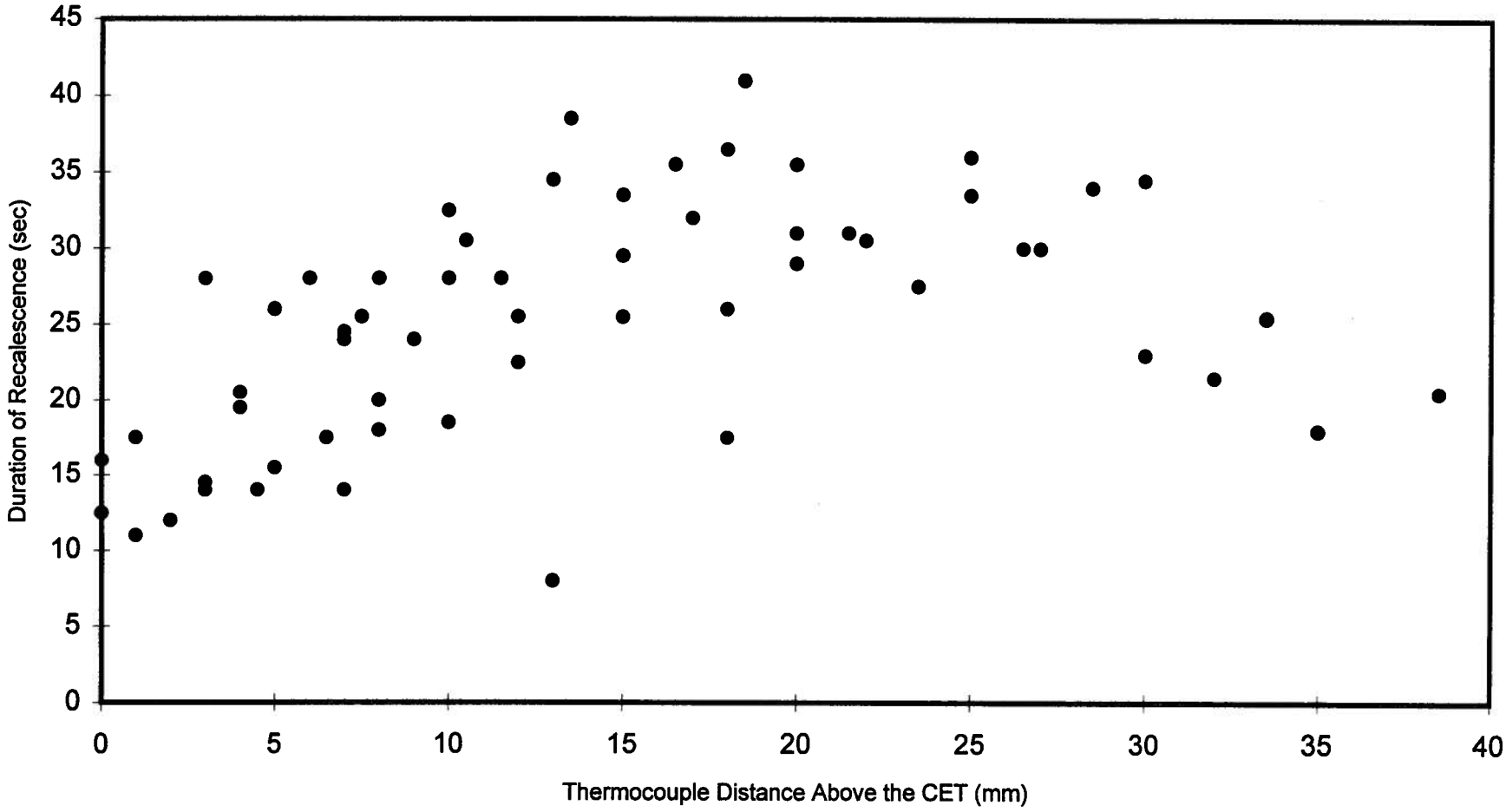

FIGURE 5.37

Duration of Recalescence vs. Distance From the CET
in MRCET Series Experiments With MAR-M200+Hf

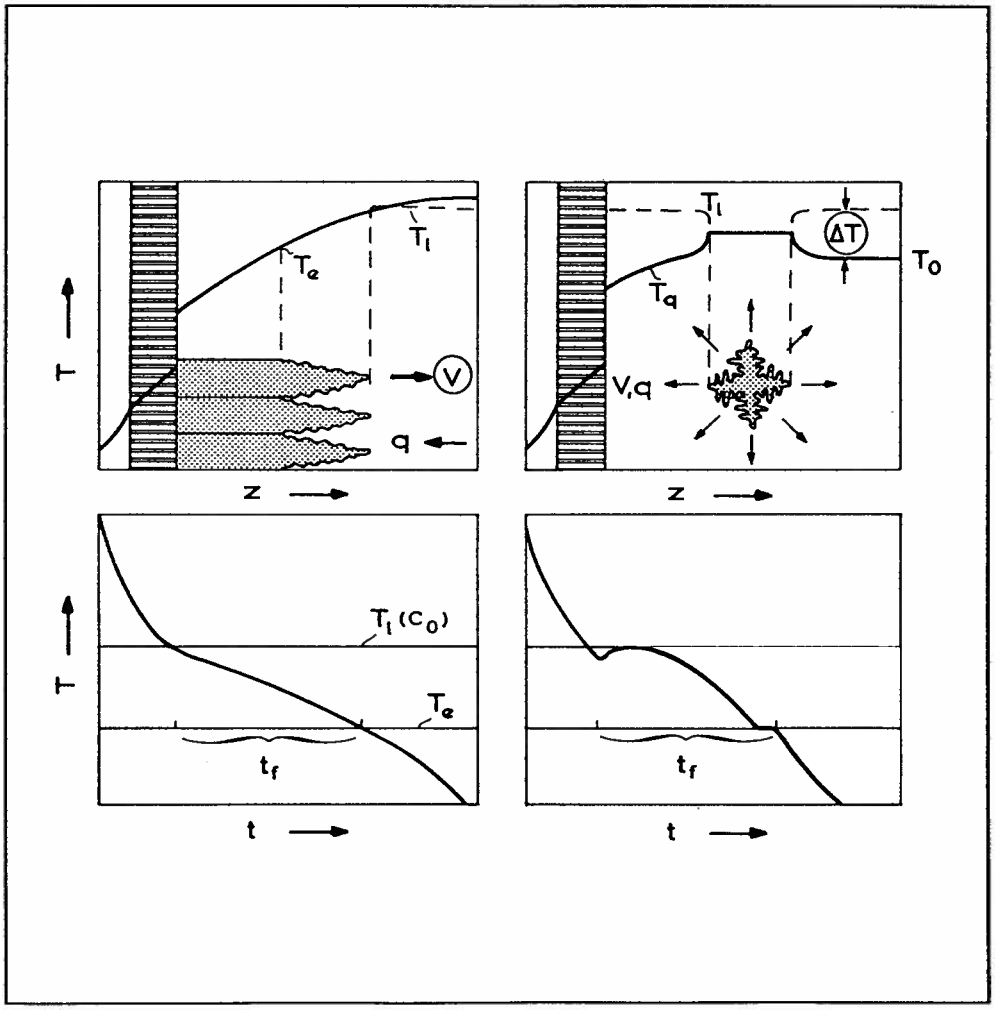

Figure 5.38: Thermal Response of Equiaxed and Columnar Dendritic Solidification in an Alloy[26]

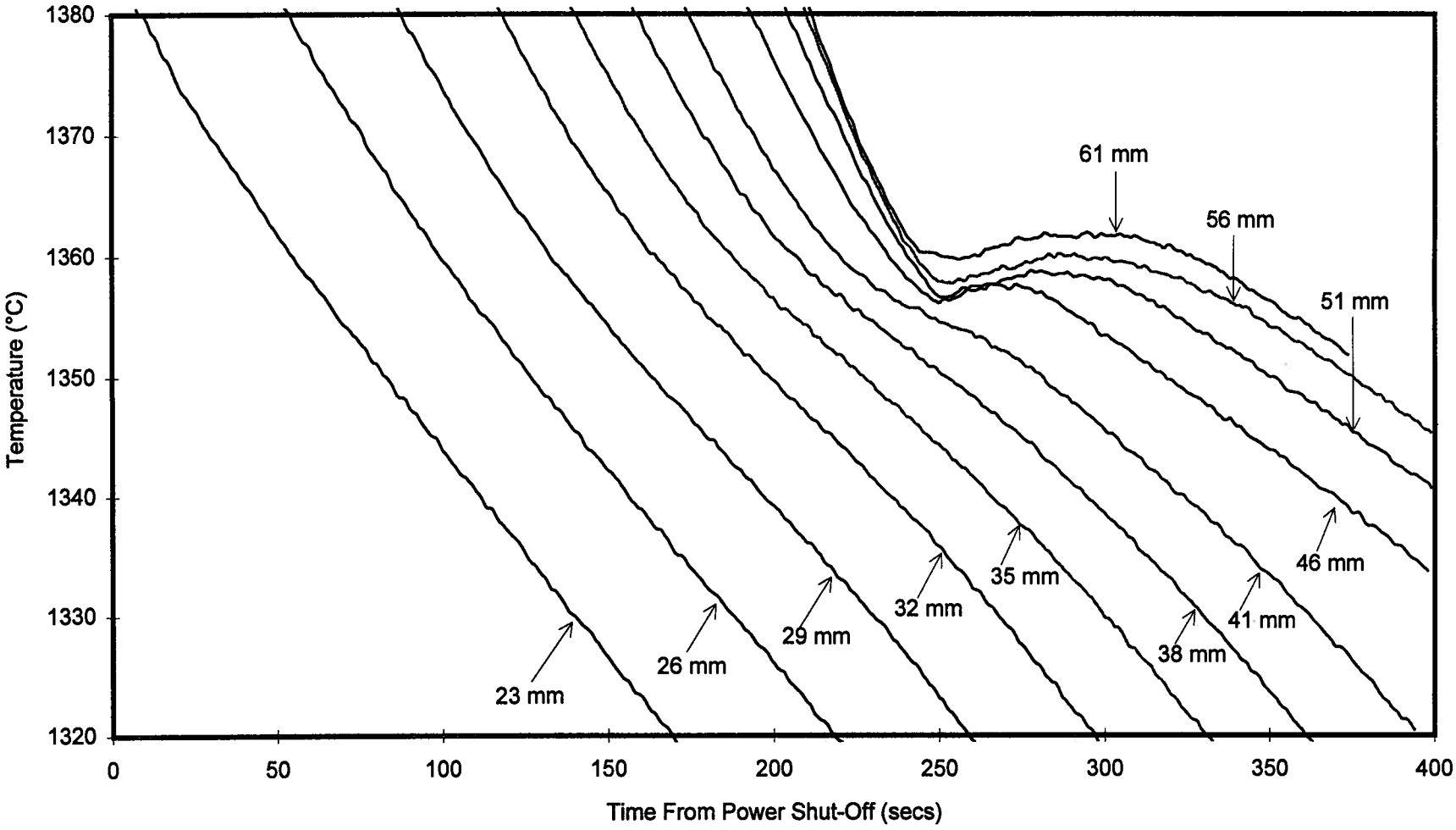

Figure 5.39
Thermal Histories at Different Locations
Above the Steel Chill Plate in CET Experiment "F" With MAR-M200+Hf

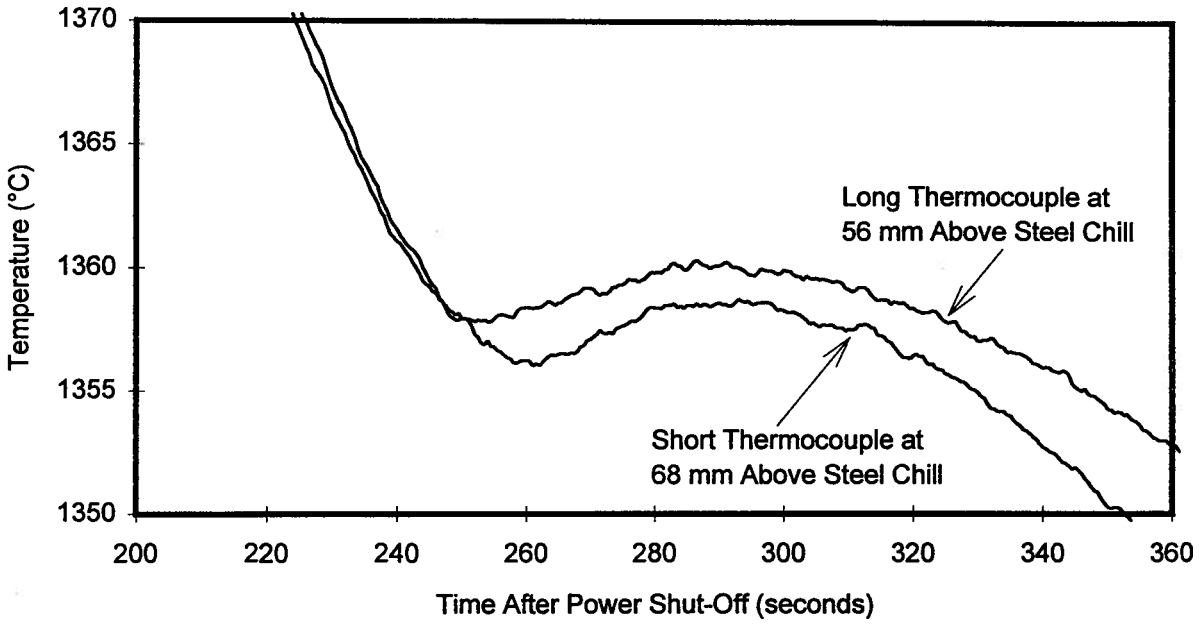

Figure 5.40a : Comparison of Thermal Histories Measured by Long and Short Thermocouples as the CET is Approached

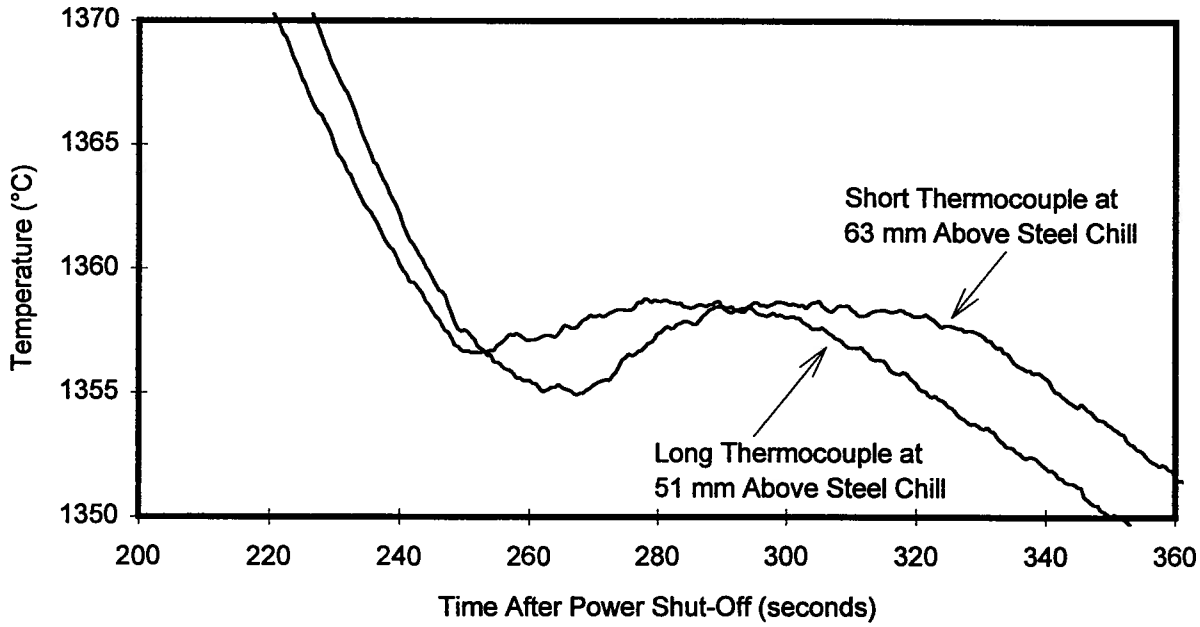

Figure 5.40b : Comparison of Thermal Histories Measured by Long and Short Thermocouples as the CET is Approached

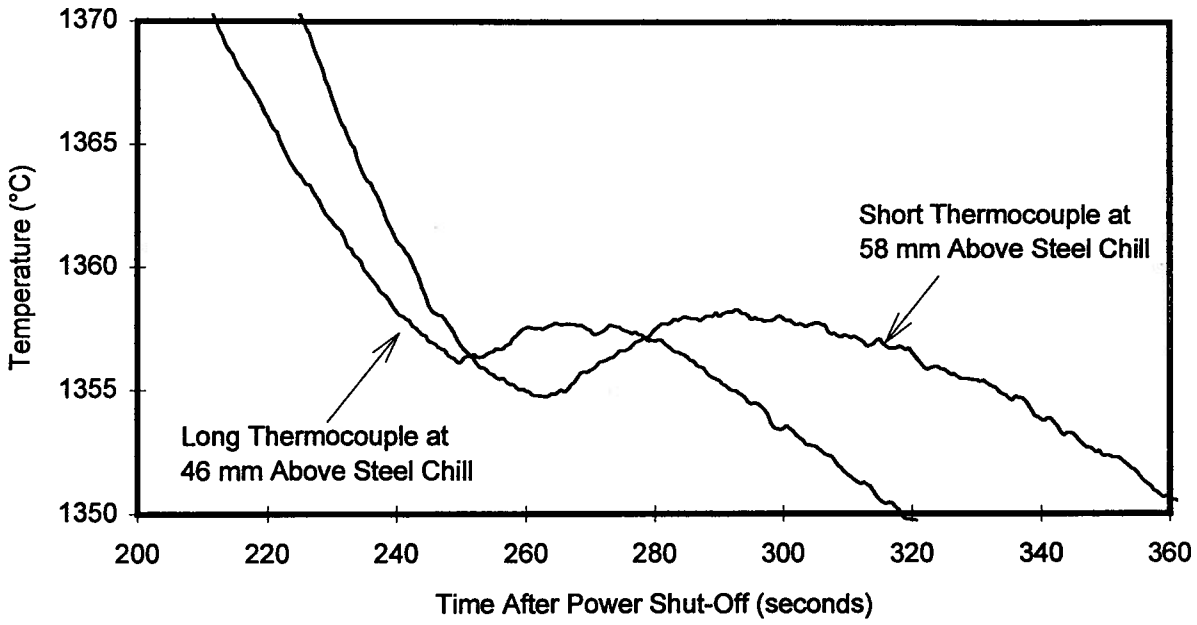

Figure 5.40c : Comparison of Thermal Histories Measured by Long and Short Thermocouples as the CET is Approached

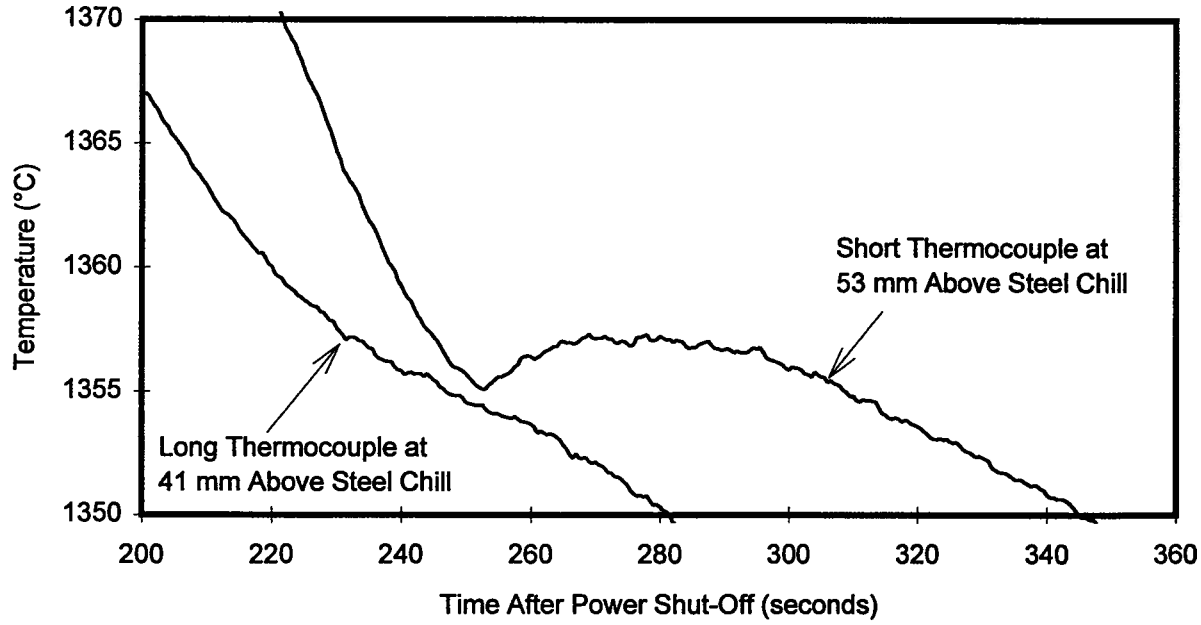

Figure 5.40d : Comparison of Thermal Histories Measured by Long and Short Thermocouples as the CET is Approached

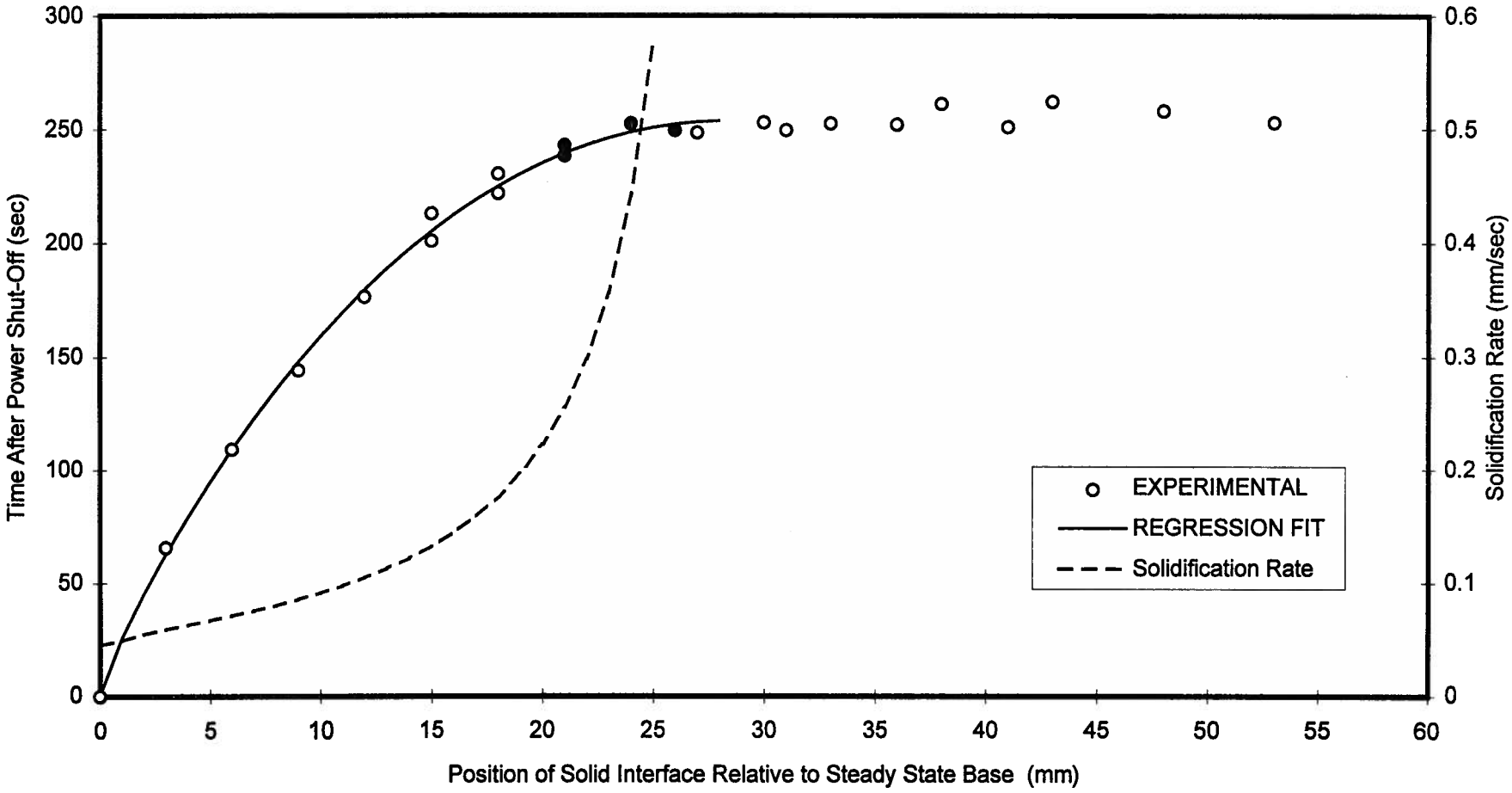

FIGURE 5.41
Regression Fit to Solid Interface Position vs Time
And Solidification Rate For Experiment MRCETF

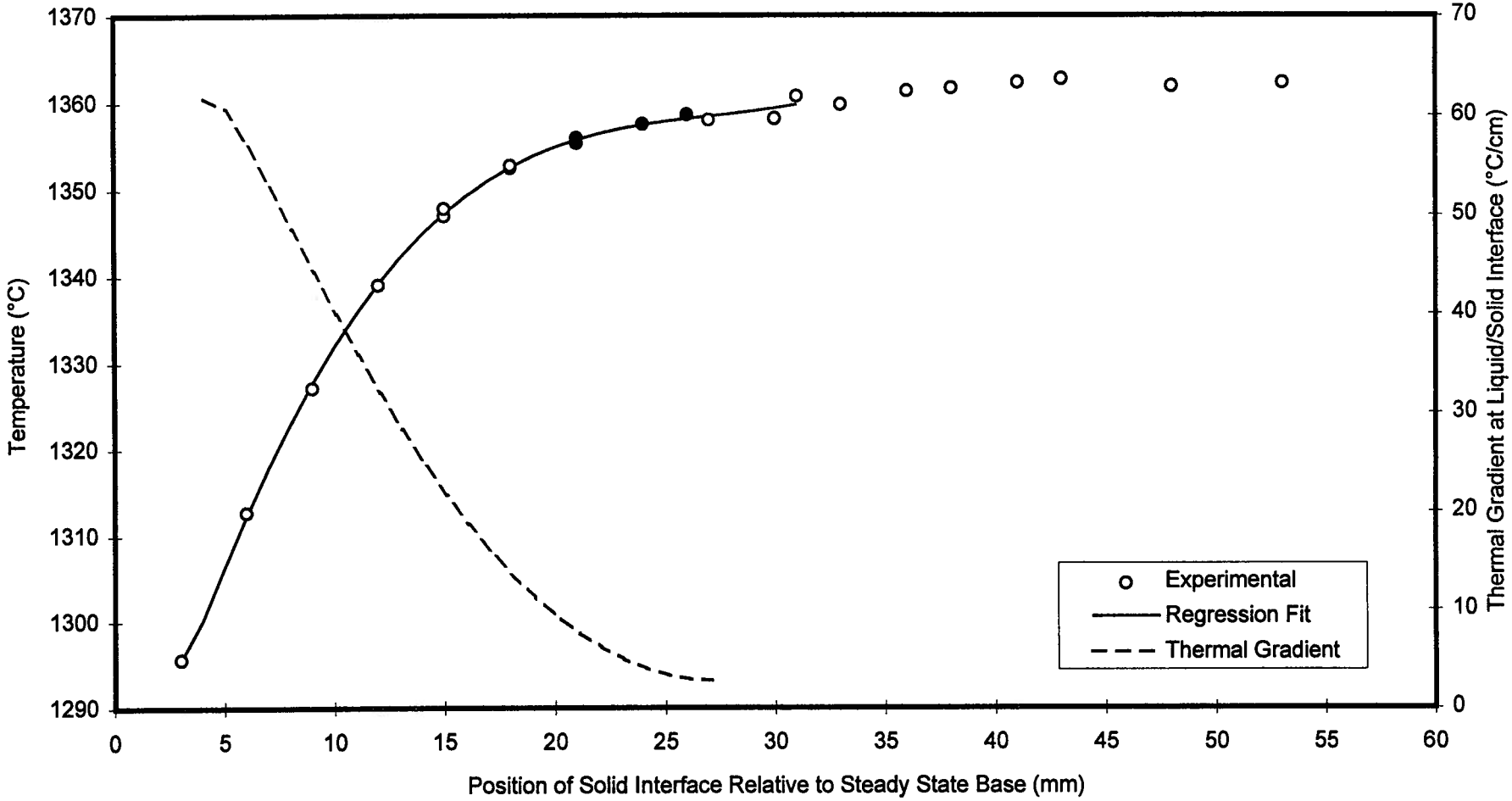

Figure 5.42
Regression Fit to Thermal Profile and Thermal Gradient in
Experiment MRCETF During Recalescence

CHAPTER 6: Mathematical Analysis of Experimental Results

6.1 Isotherm Tracking Program

A program in FORTRAN was created to track the isotherms in the CET samples directly from the thermal data. For every half second during casting, the thermal field is read from a data file. A least squares regression analysis as in equation (21) is applied to the data in order to develop an expression for the temperature at every point along the centerline in the measured region of the casting at that time. A predetermined isotherm temperature is input into the program. The program calculates the position of the isotherm at a given time, and the thermal gradient at that isotherm. Figure 6.1 shows a typical plot of the results of tracking 10 isotherms, each in increments of 1/2°C. The highest temperature isotherm tracked is 1358.5°C, which is 0.5°C more than the was determined to be the liquidus of the alloy by DTA analysis. The top plot shows the position of the isotherm in time and is associated with the leftmost Y-axis, while the bottom plot shows the thermal gradient corresponding to the position of the isotherm, and is associated with the rightmost Y-axis.

It is very significant that the three lowest temperature isotherms show a sudden slowing in their rate of advance at the same time during solidification, which corresponds to the time at which the recalescence was measured. As the temperature of the isotherm tracked is increased beyond the peak recalescence temperature, it is no longer subject to

the slow down at recalescence. Of further significance is the monotonic decrease in the thermal gradients at each isotherm as it moves up the casting, with a sudden increase corresponding to the recalescence measured during the experiment. This shows that the growth of equiaxed grains ahead of the columnar front causes a sudden increase in thermal gradient in the columnar zone. Whether this would thermally arrest the advancing columnar zone can only be resolved with the application of a complex heat flow model, which is beyond the scope of this work. However, Figure 6.1 shows direct evidence that the release of heat from the growing equiaxed grains affects the thermal conditions in the columnar zone below.

6.2 Dendrite Tip Tracking Program

While the isotherm tracking program is useful for showing key features of the heat flow conditions, it cannot be used to accurately track the dendrite tips. Isotherm velocity in a casting is often correlated to dendrite tip velocity in the literature. However, this is only valid under near steady state conditions where growth rate changes little with time. In the present study, the rapidly increasing growth rates near the CET would cause the dendrite tip to increasingly undercool with time, which would change its position relative to that predicted by an isotherm. This effect is exacerbated in the low thermal gradients observed near the CET.

Therefore the isotherm tracking program was modified to directly track the columnar dendrite tips by incorporating the KGT undercooling vs. growth rate formulation

modified with the pseudo-binary alloy method. In order to determine whether evaporative losses during the experiments affected dendrite tip growth kinetics, the end experiment alloy compositions previously calculated were used to recalculate the pseudo binary parameters. Table 6.1 shows the results of each calculation. Table 6.1 shows that evaporative losses give rise to only small differences in the pseudo binary parameters m, k and c.

The dendrite tip undercooling calculations were performed for a thermal gradient of 10°C/cm. Previous calculations showed that doubling or halving the thermal gradient of 10°C/cm led to a change in tip undercooling of less than 0.001°C for a growth rate of 0.4 mm/sec in either alloy. Therefore, under the gradients observed near the CET in the present study, the undercooling of the dendrite tip is assumed to be entirely dependent on growth rate. The pseudo binary parameters corresponding to average alloy compositions at the beginning and end of an experiment were input into the KGT formulation with results shown in Figure 6.2. Figure 6.2 shows that there is only a slight difference in the undercooling of the tip calculated using beginning and end compositions of either alloy (about 0.1 °C in the range of growth rates observed experimentally). As this difference is certainly less than the accuracy of the initial calculation, only beginning alloy compositions will be considered in all calculations.

In order to achieve fast program running times, the data plotted in Figure 6.2 was regression fit with a simple polynomial which fit at all growth rates up to 1mm/sec to

within 0.1% of the calculated tip undercooling. The polynomial was used as a function in the FORTRAN program to return a tip temperature for a given tip growth rate. The dendrite tip tracking program is essentially an isotherm tracking program which dynamically changed the isotherm temperature tracked according to the results of each analysis step. An initial isotherm temperature is tracked through the sample for one time step in order to determine the rate of advance and hence the tip undercooling. The predetermined liquidus temperature is used to yield the temperature of the tip. If the returned tip temperature does not match the initial isotherm temperature to within 0.005°C, the program iteratively finds the isotherm traveling at the rate which corresponds to its undercooling below the predetermined liquidus. Due to the nature of the present experiments and the design of the furnace, cooling rates decrease with time. As a result, lower temperature isotherms travel more slowly through the casting than do higher temperature isotherms. This is exactly opposite to the trend for dendrite tip growth, where growth rate increases as tip temperature falls. Therefore, there is a unique isotherm traveling at a growth rate which corresponds to its undercooling below any specified liquidus temperature.

In order for the program to fix a thermal gradient and tip velocity at the CET, at least two of the following are required: the liquidus temperature, position of the CET and time at which the CET occurs. The uncertainty in the measurement of temperatures in this work has been established from the thermocouple calibration experiments which showed a standard deviation of approximately 2°C. Due to this known uncertainty in the

measurement of temperature, the time of occurrence and position of the CET were used as the key variables. Therefore, when necessary, minor modifications were made to the liquidus temperature (generally within ±2°C) for each experiment, until at the average time of recalescence the program predicted a dendrite tip position corresponding to the CET position physically measured from the cast sample. The base values for liquidus temperatures used for the analysis correspond to the DTA measured values of 1359°C for AM1 and 1358°C for MAR-M200+Hf. The average time of recalescence was calculated from the two lowest positioned solidification cycles in the equiaxed zone (one for each thermocouple). Therefore an error in the measurement of G and R from the tracking program is estimated by considering the two times of recalescence individually. The resulting gradients, growth rates and their errors are given in Table 6.2. Table 6.2 shows that the dendrite tip tracking program predictions for R and G_{TIP} and their ranges of uncertainty agree well with those taken directly from the regression fit thermal plots. These results may be analyzed with the modified Hunt CET model in order to determine nucleation kinetics in the alloys studied.

6.3 Application of Hunt's CET Model to Experimental Results

Although equation (23) could be used to solve for the G and R conditions leading to the CET, the full mathematical development of the Hunt CET model was used in order to more easily incorporate the KGT formulation for dendrite tip undercooling modified with the pseudo binary approximation. The formulation was implemented as a

FORTRAN program. In order to determine the conditions leading to the CET, a single control volume of liquid is tracked as it cools from the equilibrium liquidus temperature of the alloy to the temperature of the advancing columnar dendrites. The cooling rate is defined by a predetermined thermal gradient and solidification rate. The initial value of the solidification rate is small, and is iteratively augmented until the CET occurs for a given thermal gradient.

For each iteration, the total time necessary for the control volume to cool over the desired temperature interval is divided into 500 time steps. For each time step, nucleation kinetics as given in equation (1) are applied to the liquid, along with a specified nucleation undercooling and population of potential sites. From Hunt, the heterogeneous nucleation undercooling is defined as that undercooling at which one site per cubic centimeter per second becomes active. The fraction of potential sites activated per time step is calculated, and equiaxed growth is allowed to occur at a rate governed by the undercooling of the control volume. The numbers and sizes of the equiaxed grains are tracked during each time step using the method of Hunt, where

$$n = n' + Idt \tag{24}$$

$$nr = nr_{t-1} + n \cdot dr \tag{25}$$

$$nr^2 = nr_{t-1}^2 + 2nr \cdot dr \tag{26}$$

$$nr^3 = nr_{t-1}^3 + 3nr^2 \cdot dr \tag{27}$$

where

n = the number of active nucleation sites per cubic centimeter

r = radius of a grain (cm)

These parameters may then be used to find the volume fraction of equiaxed grains by

$$\phi_E = \frac{4}{3}\pi \cdot \sum_i n_i r_i^3 \tag{29}$$

where ϕ_E is the extended volume fraction of equiaxed grains[94], as the above simplified analysis does not consider impingement of neighboring grains. The CET occurs at a real equiaxed grain volume fraction of 0.49, which corresponds to an extended volume fraction of 0.66. The mathematical development of the extended volume fraction has been carried out by Christian[94] and is based on a grain growth model which incorporates the effects of impingement of neighboring grains on the development of grain structure. The CET is considered to occur when an extended volume fraction of 0.66 of equiaxed grains is found ahead of the columnar dendrite tips. Equations (24-27) are applied to the control volume of liquid at each time step, and Equation (29) is applied once the control volume has reached the undercooling of the columnar dendrites. The iteration is stopped once ϕ_E = 0.66, otherwise the solidification rate is incrementally increased and the iteration is restarted for the same thermal gradient. The Hunt model assumes constant thermal gradients throughout the system, and that the equiaxed grains grow with the same undercooling vs. growth rate relationship that governs columnar dendritic growth.

A sensitivity analysis was performed on the model in order to ascertain the effects of changing important variables on the conditions leading to the CET. The most important variables are the number of potential nucleating sites (N_0), nucleation undercooling (ΔT_{HET}) and amount of solute in the alloy (C). The base data used for the calculations was N_0=5 per cc, ΔT_{HET}=3.5°C and C = 36 wt%. Figure 6.3 shows the effect of changing N_0 from 1 to 10000 per cc. Varying N_0 leads to no significant difference in the G and R values preceding the CET at low thermal gradients, however N_0 becomes the critical factor at high thermal gradients. Figure 6.3 shows that the CET will not occur at high thermal gradients without a sufficient number of nucleating sites. Figure 6.4 shows the effect of varying the nucleation undercooling. The CET is most sensitive to changes in ΔT_{HET} at low thermal gradients, where solidification rate is the controlling factor. Figure 6.5 shows that increasing the solute content of the alloy decreases the growth rate required to provoke a CET at all values of G. Therefore, given the solidification conditions present this technique can be used to effectively determine nucleation kinetics.

6.3.1 Calculation of Nucleation Kinetics in AM1 and MAR-M200+Hf

The Hunt model can be used to predict the nucleation undercooling of the equiaxed grains in the CET if the growth rate, thermal gradient, and number of nucleation sites per cubic cm are given. The nucleation site population has been determined from the average equiaxed grain size in each sample while the dendrite tip tracking program was

used to give values of R at the CET. As previously discussed, the average thermal gradient in the liquid ahead of the dendrite tips rather than at the dendrite tips is used for the present analysis.

Nucleation kinetics for each alloy (AM1, EB refined AM1 and MAR-M200+Hf) were calculated using the average thermal gradients and growth rates for the 5 experiments performed on the alloy. Maximum and minimum bounds on the nucleation undercooling were established by using the maximum and minimum N_0 observed in the 5 experiments. In addition, the level of uncertainty in the nucleation undercooling for a given alloy and N_0 was established by using the maximum and minimum values of R and G_{LIQ} from their respective ranges of uncertainty in a set of experiments. The values of R, G_{LIQ}, their uncertainties and N_0 used in the calculation of ΔT_N are given in Table 6.3.

The nucleation undercooling (ΔT_N) was calculated by running the programmed modified Hunt model with a given N_0 and incrementally augmenting ΔT_N until both G and R matched the desired values. Both equation (23) and the fully programmed model were used to calculate ΔT_N with results differing by less than 0.1 °C in all cases. Results of the calculations are given in Table 6.3. Figure 6.6 shows a representative plot of the experimental results for the normal AM1 series of experiments, and the modified Hunt model predictions over a much wider range of conditions. Figure 6.6 together with the sensitivity analysis shows a very important result: the modified Hunt CET model is insensitive to grain size and thermal gradient in the ranges of these two variables

observed in the experiments. This corresponds precisely to the observed experimental results, and shows that the rate of solidification is the principle variable from which nucleation kinetics are determined.

The average ΔT_N for all alloys is 3.7 ± 0.4°C, with MAR-M200+Hf and normal AM1 yielding almost identical ranges, and EB refined AM1 showing a slightly larger value. However, the differences are all within the range of uncertainty in the calculation. The similarity in ΔT_N among the three alloys suggests that the differences in alloy chemistry (between AM1 and MAR-M200+Hf) and the EB refining of AM1 are not factors which strongly determine nucleation undercooling. Rather, the most obvious similarity between the alloys (FCC structure and lattice parameter) suggests that the Turnbull-Vonnegut theory relating lattice mismatch to nucleation undercooling is applicable to Ni-based superalloys, and that the same foreign substrate is responsible for nucleation in all three systems. However, the value of ΔT_N of 3.7°C is well below any of the predicted undercooling values shown in Table 2.1, hence the foreign substrate itself remains unknown.

Table 6.3 shows that the range of uncertainty in ΔT_N in a given alloy arises primarily from the uncertainties in R and G_{LIQ} rather than from the different values of N_0 used. This indicates that the level of accuracy in the determination of ΔT_N is limited by experimental error rather than variations in the grain size from sample to sample. Furthermore, the modified Hunt model calculations indicate that in the range of thermal

gradients and N_0 observed, the CET is relatively insensitive to N_0. This is important as the present study is biased toward a relatively large grain size as observed in the equiaxed zone of the CET castings. In industrial equiaxed castings with higher cooling rates, much smaller grains sizes are observed, as those found in the bases of some of the CET castings. This raises the possibility of an extended family of nucleating sites which become active at lower undercoolings than those observed during the present study. Therefore, the present experiments show results applicable for the ranges of cooling rates (G·R) shown.

According to the modified Hunt model, the above results indicate that in the alloys studied, an undercooling of 3.7 ± 0.4°C below the liquidus will produce 1 active nucleus per cm^3 per second. This explains the statistical nature of the appearance of spurious grains in the platforms of turbine blade castings. The platforms are typically 2 mm in thickness, and approximately 40 mm in length and 30 mm in width (measured from a single crystal blade sample provided by General Electric). Approximately half of the platform area is occupied by the blade at the center. Therefore the platform which extends beyond the blade contains an approximate volume of 1.2 cm^3, a fraction of which would be undercooled during the casting process. As seen with the SNECMA experiments, the volume of undercooled liquid present has a profound influence on the rate of nucleation of equiaxed grains. However, a proper analysis of the probability of spurious grain generation in a typical platform would require complex modeling of the

heat transfer during solidification of a turbine blade, which is beyond the scope of this work.

Table 6.1: Pseudo Binary Alloy Values for AM1 and MAR-M200+Hf

Pseudo-Binary Value	AM1 Starting Composition	AM1 Ending Composition	MAR-M200+Hf Starting Composition	MAR-M200+Hf Ending Composition
c	0.360	0.351	0.388	0.375
m	-4.35	-4.41	-3.12	-3.03
k	0.806	0.800	0.778	0.774

TABLE 6.2: Growth Rates and Thermal Gradients from Regression Calculations and the Dendrite Tip Tracking Program

Experiment Designation	Regression Calculated Gradient G (°C/cm)	Regression Calculated Growth Rate R (mm/sec)	Tip Tracking Program Gradient (°C/cm)	Tip Tracking Program Growth Rate (mm/sec)
AMCETB	2.6-4.0	0.33-0.44	4.6 ± 2.2	0.39 ± .05
AMCETC	6.4-10.8	0.19-0.33	6.9 ± 1.7	0.31 ± .03
AMCETD	3.8-9.1	0.22-0.40	4.5 ± 1.3	0.23 ± .05
AMCETE	0.0-2.7	0.45-0.15	5.0 ± 2.1	0.39 ± .06
AMCETF	4.1-9.0	0.22-0.46	5.6 ± 1.2	0.33 ± .05
MRCETB	4.7-7.2	0.33-0.60	4.3 ± 1.1	0.37 ± .04
MRCETC	4.7-7.2	0.33-0.50	7.5 ± 2.3	0.39 ± .04
MRCETD	4.5-7.9	0.32-0.49	6.0 ± 1.5	0.39 ± .06
MRCETE	0.07-2.8	0.34-0.50	4.1 ± 2.2	0.35 ± .05
MRCETF	3.3-8.1	0.28-0.45	6.7 ± 2.6	0.36 ± .04
AMSX90	3.7-8.0	0.35-0.50	5.8 ± 1.9	0.34 ± .05
AMNORM	4.1-8.9	0.24-0.35	13.6 ± 3.3	0.30 ± .05
AMTIN	8.9-13.5	0.28-0.38	5.3 ± 2.5	0.35 ± .04
AMSX45	2.6-6.3	0.31-0.48	3.5 ± 1.1	0.31 ± .05
AMMGAL	0.2-3.9	0.50-1.10	4.5 ± 2.0	0.33 ± .07

Table 6.3: Calculation of Nucleation Kinetics in AM1, EB Refined AM1 and MAR-M200+Hf

Alloy Used	N_0 Employed (nuclei/cm^3)	Average R (mm/sec)	Average G (°C/cm)	ΔT_N (°C)
Normal AM1	4	0.32 ± .05	1.60 ± 0.59	3.5 ± 0.6
Normal AM1	24	0.32 ± .05	1.60 ± 0.59	3.7 ± 0.4
EB Refined AM1	12	0.33 ± .05	0.93 ± 0.38	3.9 ± 0.4
EB Refined AM1	25	0.33 ± .05	0.93 ± 0.38	3.9 ± 0.4
MAR-M200+Hf	4	0.38 ± .04	1.47 ± 0.39	3.5 ± 0.4
MAR-M200+Hf	18	0.38 ± .04	1.47 ± 0.39	3.8 ± 0.3

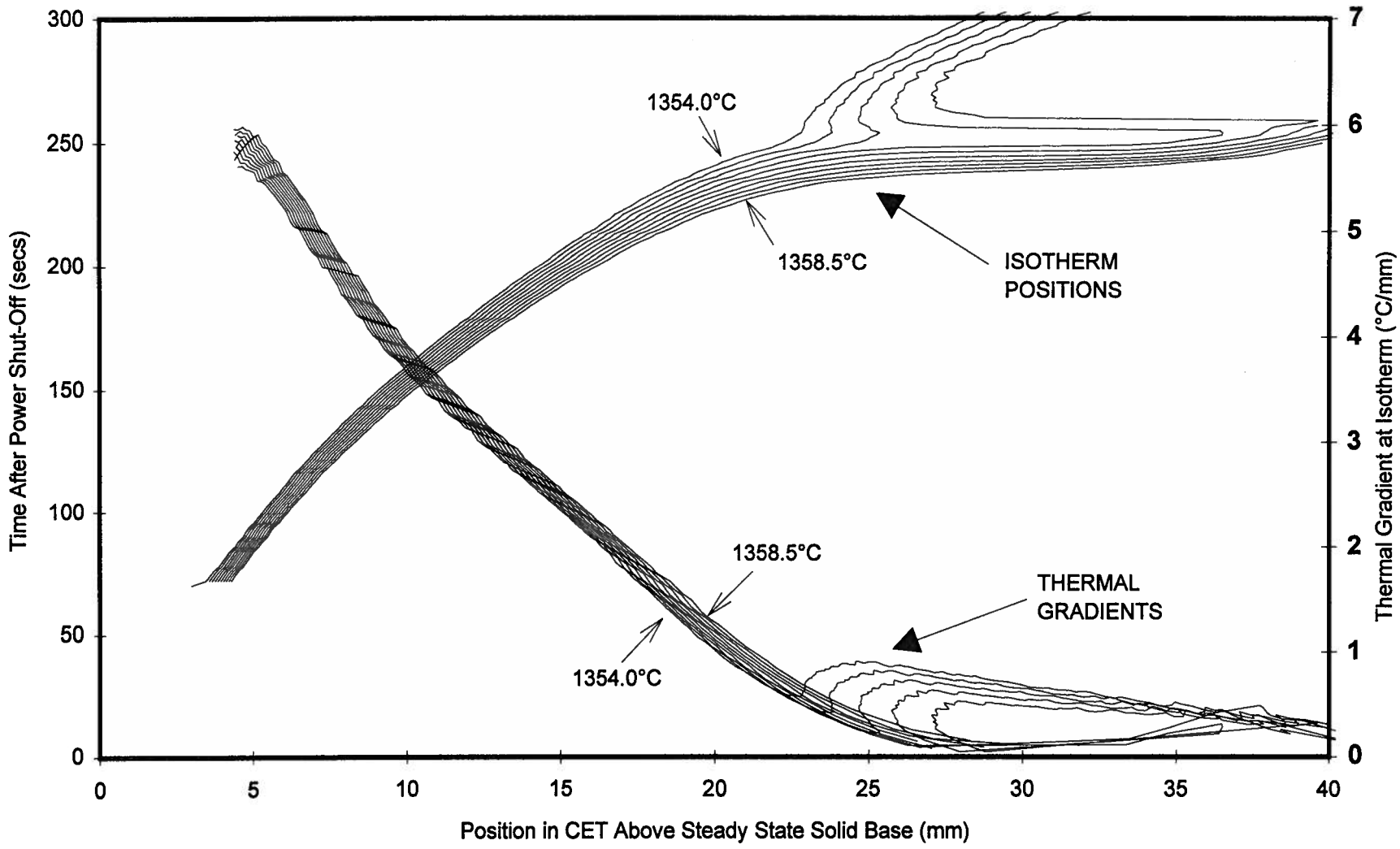

Figure 6.1: Position of Isotherm and Thermal Gradient at Isotherm During Solidification in MRCETF Series Using Isotherm Temperatures of 1354.0 - 1358.5°C

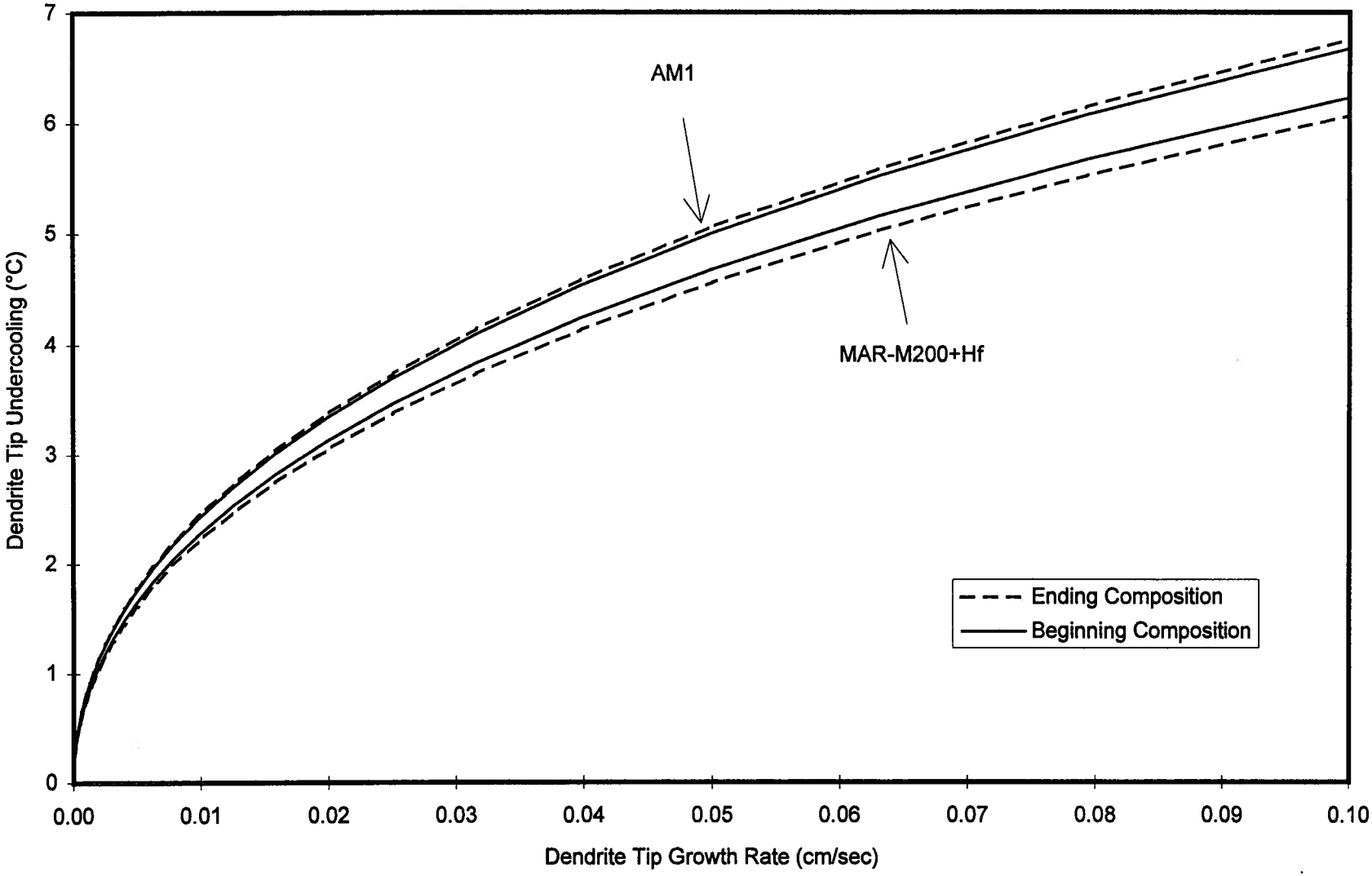

Figure 6.2: Dendrite Tip Undercooling vs. Growth Rate for MAR-M200+Hf and AM1

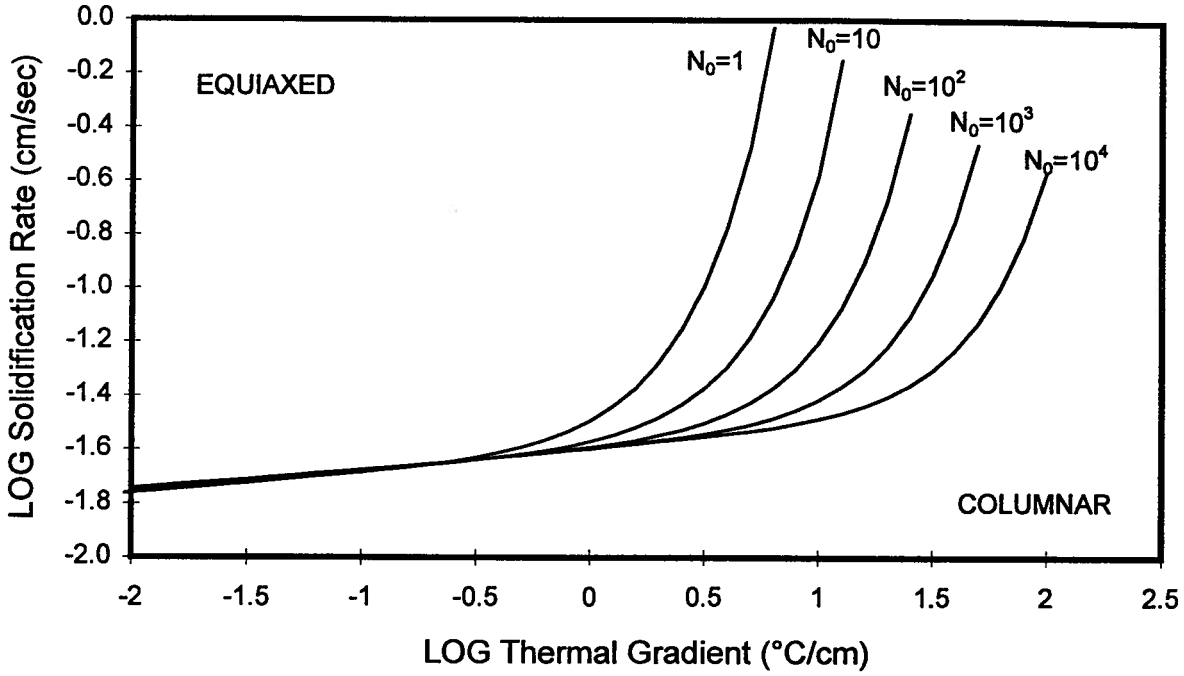

Figure 6.3: Conditions for the CET in Superalloy AM1 With Varying Populations of Potential Nucleation Sites Per cm^3

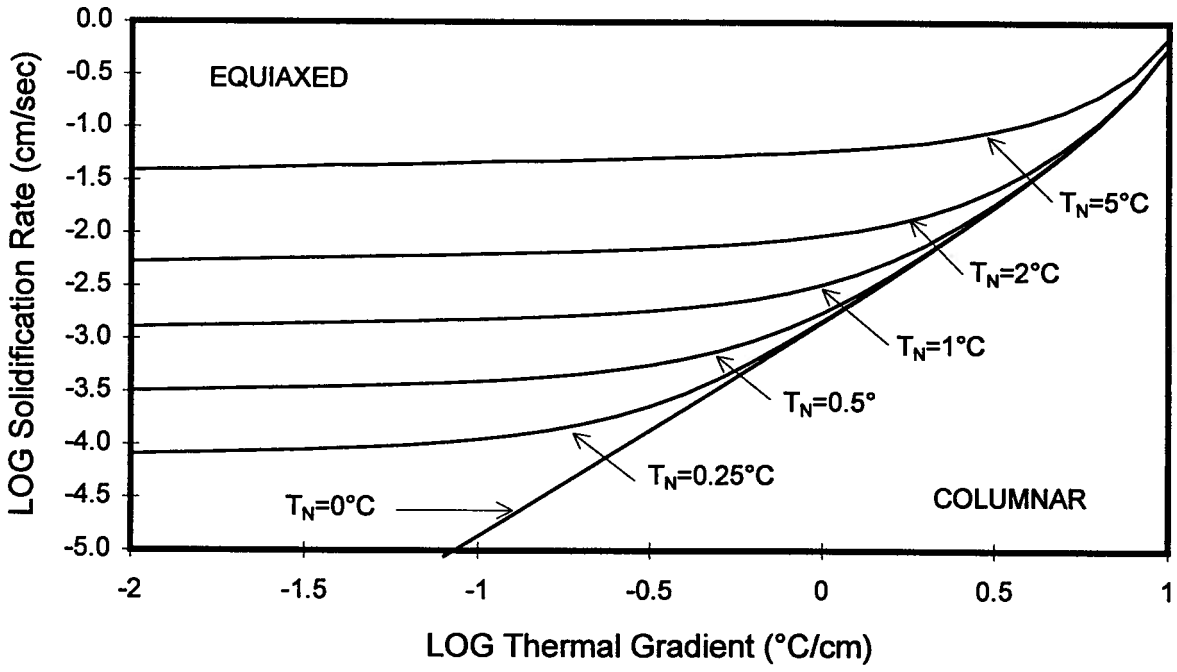

Figure 6.4: Conditions for a CET in Superalloy AM1 With Varying Heterogeneous Nucleation Undercooling

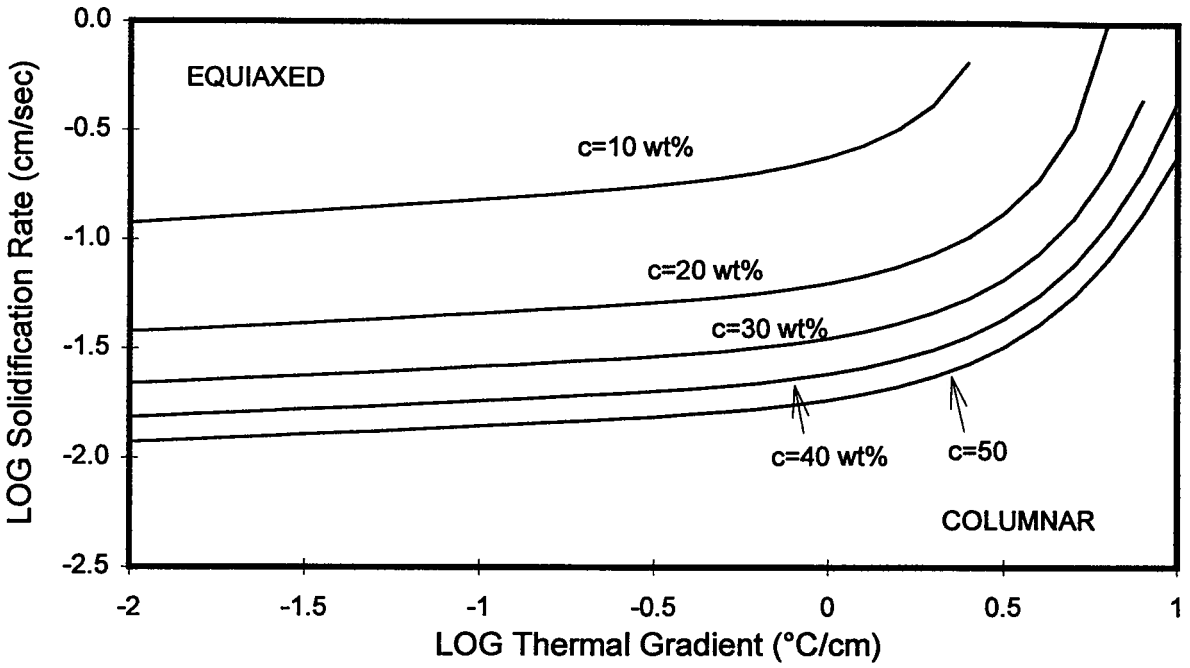

Figure 6.5: Conditions for the CET in Superalloy AM1 With Varying Equivalent Binary Alloy Content

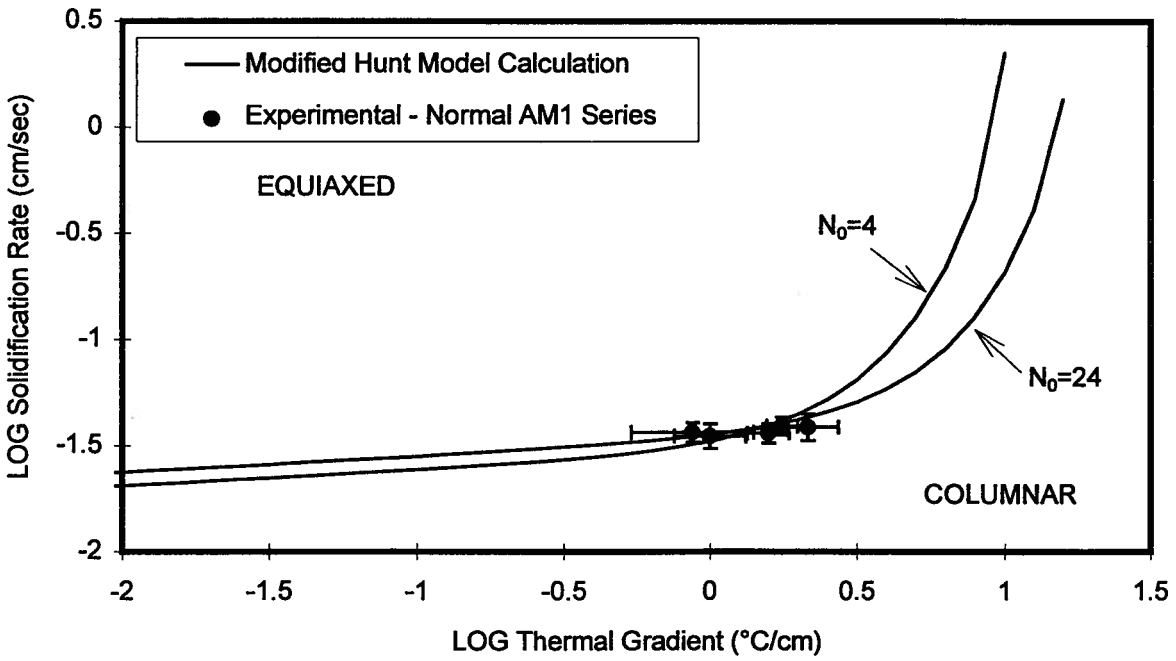

Figure 6.6: Solidification Conditions for a CET in Normal AM1 Series: Model and Experiment

CHAPTER 7: Summary and Recommendations

7.1 Summary

The purpose of the present work was to measure the nucleation kinetics in the Ni-based superalloys AM1, EB refined AM1 and MAR-M200+Hf. This was done by reproducing a CET in these alloys and experimentally measuring the growth rate and thermal gradient ahead of the solid front prior to the CET, as well as the number of equiaxed grains per cc. This data was analyzed by the modified Hunt model to yield the undercoolings at which one nucleation site per cc per second is activated. The present study also contributes to the general knowledge of the CET in Ni-based superalloys. The important features of the work are summarized as follows:

1. Physical Features of the CET

The transition from columnar to equiaxed grains was observed to occur abruptly, with no region of mixed columnar and equiaxed grains. The CET interface was horizontal and in most cases flat. There was no indication that nucleation of equiaxed grains occurred on the alumina tube wall.

2. Source of Equiaxed Grains for the CET

The thermal profiles in the regions of the castings which could be accurately measured showed a lack of any negative thermal gradient at the top of the sample, which indicates that supercooling and hence nucleation did not occur there. The thermosolutal convection and dendrite arm remelting observed by Pollock were not observed during these trials. Thermal data in terms of recalescences and the observed thermal profiles indicated that nucleation and growth of equiaxed grains occurred first in the region of constitutionally undercooled liquid ahead of the advancing columnar interface. This is in accordance with the CET model of Hunt.

3. Criteria for the CET in Superalloys

The SNECMA experiments showed that the presence of undercooled liquid does not guarantee the occurrence of a CET. The transverse heat flow operating in the Bridgeman furnace at SNECMA created a highly curved columnar front, which reduced the volume of undercooled liquid ahead of the vertically growing peripheral dendrites. Because no classical CET was observed to occur during the SNECMA experiments, it is assumed that the reduction in the volume of undercooled liquid was the critical difference between those experiments and the UBC experiments which showed similar conditions of solidification as measured along the centerline. The number of active nucleating sites in the alloys used was determined to be 7.5 per cc for the SNECMA experiments and

ranging from 4 to 25 per cc for the UBC experiments. Therefore, the occurrence of a CET in Ni based superalloys depends on the presence of a minimum undercooling and a minimum volume of undercooled liquid due to the low numbers of active nucleation sites available per unit volume.

The ranges of G and R observed at the CET are too limited to either confirm or deny the G/R criterion for the CET. The findings of the present study do not contradict the work of Pollock et al. because of the significantly different conditions of solidification employed during the experiments. Rather, the two studies are complimentary to one another and show the possibility of provoking a CET in Ni based superalloys from either of two unique sources of equiaxed grains.

4. Nucleation Kinetics in Superalloys

Application of the Hunt CET model to experimental data showed that the undercooling of heterogeneous nucleation was consistent among the alloys studied and averaged 3.7 °C. This defines the undercooling at which one site per cc per second becomes active. The similarity of the undercooling among the alloys suggests that the same foreign substrate is responsible for the nucleation of equiaxed grains in all three alloys.

7.2 Conclusions

- A CET was reproduced in 5 experiments each with AM1, EB refined AM1 and MAR-M200+Hf Ni based superalloys. The extensive thermal data recorded is the first of its kind for the CET in Ni based superalloys, and contributes significantly to the general CET data available in the literature.

- Experimental results confirmed that the only source of equiaxed grains was heterogeneous nucleation in the region of constitutionally undercooled liquid ahead of the advancing columnar front.

- A CET was found to occur at an average of R=0.32±0.05 mm/sec and G_{LIQ}=1.6±0.58 °C/cm for normal AM1, R=0.33±0.05 mm/sec and G=0.93±0.47 °C/cm for EB refined AM1 and R=0.38±0.05 mm/sec and G=1.47±0.39°C/cm for MAR-M200+Hf.

- The undercooling at which one nucleation site is activated per second per cc was found to be almost identical among the three alloys, averaging 3.7±0.4°C.

- The CET in Ni-based superalloys depends on the presence of a sufficient volume of undercooled liquid as well as on the extent of undercooling. This explains the statistical nature of the appearance of spurious grains in the platforms of turbine blades. The direct application to industrial practice of the results of the present experiments requires complex heat transfer modeling and/or experimental

measurements to confirm the nature of the undercooling in platforms, which is beyond the scope of this work.

7.3 Recommendations for Further Work

• An investigation of the possible sources of nucleation in Ni based superalloys could be carried out using the method of Bramfitt. Pure Ni could be used as the metal as theory suggests that the undercooling of nucleation observed in pure Ni should be the same as that observed in any alloy of Ni which has an FCC structure and a similar lattice parameter.

• A fully coupled heat transfer model could be applied to the present experimental results to investigate the nature of the CET to a greater depth, including the possibility that the columnar front is thermally arrested after nucleation of the equiaxed grains, rather than arrested by mechanical blockage as suggested by Hunt.

• The conditions leading to the CET could be determined for a wide range of alloys, to confirm or deny the similarity of nucleation kinetics among the Ni based superalloys.

• The UBC CET furnace should be redesigned in order to achieve a wider range of solidification conditions (in particular, raising the thermal gradient) at the CET. This could be done by increasing water flow at the Cu chill plate to enhance cooling and using a longer CET sample which would offer an increased thermal bulk at the top.

BIBLIOGRAPHY

[1] Van Drunen, G. *Ironmaking and Steelmaking*. 1975 vol.2 pp.125-130.

[2] Ganaha, T., Pearce, B.P. and H.W. Kerr. "Grain Structures in Aluminum Alloy GTA Welds". *Metallurgical Transactions A*, vol. 11A August 1980 pp. 1351-1359

[3] Pardo, E., Villafuerte, J.C., and Kerr, H.W. "A Finite Element Study of the Columnar- Equiaxed Transition in GTA Welding of Stainless Steels". Recent Trends in Welding Science and Technology Ed. Vitek, J.M. and David, S.A. ASM International 1985 pp. 159-164.

[4] Choudhury, A. Vacuum Metallurgy, ASM International 1980, pg. 149.

[5] Hunt, J.D. and Flood, S.C. "Columnar to Equiaxed Transition." Metals Handbook, 9th Edition. vol 15. ASM International 1988. pp. 130-136.

[6] Genders, R. *Journal of the Institute of Metals*. vol. 35 (1926).

[7] *Z. Krist.* A 92 (1935) pg. 89.

[8] Winegard, W.C. and Chalmers, B. *Transactions of the American Society for Metals*, vol. 46 (1954) pg. 1214.

[9] Southin, R.T. *Transactions of the Metallurgical Society of the AIME.* vol. 239 (1967) pg. 220.

[10] Ohno, A., Motegi, T., and Soda, H. *Transactions of the Iron and Steel Institute of Japan*, 1971. Pg 18.

[11] Uhlmann, D.R., Seward III, T.P., and Chalmers, B. *Transactions of the AIME*, vol. 236, 1966, pg. 527.

[12] Doherty, R.D., Cooper, P.D., Bradbury, Bradbury, M.H. and Honey, F.J. "On the Columnar to Equiaxed Transition in Small Ingots." *Metallurgical Transactions A.* vol. 8A, March 1977, pg. 397.

[13] Tarshis, L.A., Walker, J.L., and J.W. Rutter. *Metallurgical Transactions*, vol. 2, Sept. 1971, pp. 2589-2597.

[14] Cole, G.S., Casey, K.W., and Bolling, G.F. *Metallurgical Transactions*, vol. 5, Feb 1974, pp. 407-411.

[15] Campbell, J. *International Metals Review*. vol. 26, 1981, pg. 71.

[16] Chalmers, B. Principles of Solidification. John Wiley and Sons, Inc. 1964 pg. 70.

[17] Turnbull, D. and Cech, R.E. *Journal of Applied Physics*, vol. 21 1950, pg. 804.

[18] Glicksman, M.E. and Childs, W.J. "Nucleation Catalysis in Supercooled Liquid Tin." *Acta Metallurgica*. vol. 10, Oct. 1962, pp. 925-933.

[19] Hoffmeyer, M.K. and Perepezko, J.H. "Nucleation Catalysis by Dispersed Particles." *Scripta Metallurgica*. vol. 22, 1988, pp. 143-1148.

[20] Bramfitt, Bruce L. "The Effect of Carbide and Nitride Additions on the Heterogeneous Nucleation Behaviour of Liquid Iron." *Metallurgical Transactions*. vol. 1, July 1970, pp.1987-1995.

[21] Ohashi, T., Fujii, H., Nuri, Y. and Asano, K. "Effect of Oxides on Nucleation Behaviour in Supercooled Iron." Transactions of the Iron and Steel Institute of Japan Vol. 17, No 5, 1977. Pg 262-269.

[22] Rasmussen, D.H. and Javed, K. "Undercooling and Nucleation in Iron-Nickel Alloys." Undercooled Alloy Phases. Proceedings of a Symposium: C.C. Koch, Hume Rothery Memorial Symposium. Ed. E.W. Collings, Pub.TMS 1986, Pub. pp. 79-95.

[23] Willnecker, R., Herlach, D.M. and Feuerbacher, B. *Applied Physics Letters*, no. 49 vol. 20, Nov. 17, 1986, pp. 1339-1341.

[24] Perepezko, J.H., Rasmussen, D.H., Anderson, I.E., and Loper, C.R. "Undercooling of Low-Melting Metals and Alloys." Proceedings of a Conference: International Conference on Solidifidation and Casting, Sheffield, July 1977, pp. 169-174. Pub. 1979 The Metals Society, London.

[25] Cech, R.E. and Turnbull, D. *Journal of Metals*. vol 242, 1951, pg. 242.

[26] Kurz, W. and Fisher, D.J. Fundamentals of Solidification. Third Edition. Pub. Trans Tech Publications, 1989. pg. 88.

[27] Ivanstov, G.P. *Doklady Akademii Nauk SSSR*, vol. 58, 1947, pg. 567.

[28] Zener. *Transactions of the TIM-AIME*, vol. 167, 1946, pg. 550.

[29] Glicksman, Schaefer, Ayers. *Metallurgical Transactions A*, vol. 7A, 1976, pg.1747.

[30] Langer, Muller-Krumbhaar. *Acta Metallurgica*, vol. 26, 1978, pg. 1681.

[31] Langer, Muller-Krumbhaar *Acta Metallurgica*, vol. 26, 1978, pg. 1689.

[32] Langer, Muller-Krumbhaar *Acta Metallurgica*, vol. 26, 1978, pg. 1697.

[33] Mullins, W. W. and Sekerka, R. F. "Stability of a Planar Interface During Solidification of a Dilute Binary Alloy." *Journal of Applied Physics*, vol. 35, no. 2, Feb. 1964, pp. 444-451.

[34] Kurz, Giovanola, Trivedi. *Acta Metallurgica*, vol. 34, 1986, pg. 823.

[35] Kurz and Trivedi. *Acta Metallurgica*, vol. 38, 1990 pg. 1.

[36] Trivedi and Mason. *Metallurgical Transactions A*, vol. 22A, 1991, pg. 235.

[37] Chopra, Glicksman and Singh. *Metallurgical Transactions A*, vol. 19A, 1988, pg. 3087.

[38] Tassa, M. and Hunt, J.D. "The measurement of Al-Cu Dendrite Tip And Eutecitc Interface Temperatures and Their Use for Predicting the Extent of the Eutectic Range." *Journal of Crystal Growth*, vol. 34, 1976, pp. 38-48.

[39] Coates, D.E., Subramanian, S.V. and Purdy, G.R. "Solid-Liquid Interface Stability During Solidification of Dilute Ternary Alloys." *Transactions of the Metallurgical Society of the AIME*, vol. 242, May 1968, pp. 800-809.

[40] Bobadilla, M., Lacaze, J. and Lesoult, G. "Influence Des Conditions de Solidification Sur le Deroulement de la Solidification des Aciers Inoxydables Austenitiques." *Journal of Crystal Growth*, vol. 89, 1988, pp. 531-544.

[41] Rappaz, M., David, S.A., Vitek, J.M. and Boatner, L.A. "Analysis of Solidification Microstructures in Fe-Ni-Cr Single Crystal Welds." *Metallurgical Transactions A*, vol. 21A, June 1990, pp.1767-1782.

[42] Witzke, S. and Riquet, J.P. "Columnar-Equiaxed Transition in Al-Cu Alloy Ingots." *Acta Metallurgica*, vol. 30, 1982, pp. 1717-1722.

[43] Fredricksson, H. and Olson, A. "Mechanism of Transition from Columnar to Equiaxed Zone in Ingots." *Materials Science and Technology*. vol. 12, May 1986,
pg. 508.

[44] Lipton, J. W. Kurz, W Heinemann Concast Technology News. Vol 22, 1983 pg 4

[45] Hunt, J.D. "Steady State Columnar and Equiaxed Growth of Dendrites and Eutectic." *Materials Science and Engineering*, vol. 65, 1984, pp. 75-83.

[46] Flood, S.C. and Hunt, J.D. "A model of a Casting." *Applied Scientific Research*, vol. 44, 1987, pp. 27-42.

[47] Flood, S.C. and Hunt, J.D. "Columnar and Equiaxed Growth" *Journal of Crystal Growth*, vol. 82, 1987, pp. 543-551.

[48] Witzke, S., Riquet, J.P. and Durand, F. "Diffusion Field Ahead of a Growing Columnar Front: Discussion of the Columnar - Equiaxed Transition." *Acta Metallurgica*. vol. 29, pp 365-374.

[49] Brown, S.G.R. and Spittle, J.A. "Computer Simulation of Grain Growth and Macrostructure Development During Solidification." *Materials Science and Technology*, vol. 5, April 1989, pp. 362-368.

[50] Zhu, P. and Smith, R.W. "Dynamic Simulation of Crystal Growth by Monte Carlo Method II: Ingot Microstructures." *Acta Metall. Mater.* vol 40, no. 12, 1992, pp. 3369-3379.

[51] Rappaz, M. and Gandin, Ch.-A. "Probabilistic Modelling of Microstructure Formation in Solidification Processes." *Acta Metall. Mater.* vol. 41, no.2, 1993 pp. 345-360.

[52] Wang, C.Y. and Beckermann, C. "Prediction of Columnar to Equiaxed Transition During Diffusion Controlled Dendritic Alloy Solidification." *Metallurgical and Materials Transactions A*, vol. 25A, May1994, pp.1081-1093.

[53] Mahapatra, R.B. and Weinberg, F. "The Columnar to Equiaxed Transition in Tin-Lead Alloys." *Metallurgical Transactions B*, vol. 18B, June 1987, pp.425-432.

[54] Ziv, I. and Weinberg, F. "The Columnar-to-Equiaxed Transition in Al 3 Pct Cu." *Metallurgical Transactions B*, vol. 20B, Oct 1989, pp. 731-734.

[55] Spittle, J.A. and Tadayon, M. R. "Observations on the Numerical Prediction of the Columnar to Equiaxed Grain Transition in Castings." *Cast Metals*, vol. 7, no. 2, 1994, pp. 123-126.

[56] Pollock, T.M., Murphy, W.H., Goldman, E.H., Uram, D.L. and Tu J.S. "Grain Defect Formation During Directional Solidification of Nickel Base Single Crystals." Proceedings of a Conference: Superalloys 1992. Pg 125-134, Pub The Minerals, Metals and Materials Society, 1992.

[57] McLean, M. Directionally Solidified Materials for High Temperature Service

Pub. The Metals Society, London, 1983.

[58] McLean, M. and Quested, P.N. "Solidification Morphologies in Directionally Solidified Superalloys." *Materials Science and Engineering*, vol. 65, 1984, pp. 171-180.

[59] Sahm, P.R. and Schubert, F. "Keynote Address: Solidification Phenomena and Properties of Cast and Welded Microstructures." Proceedings of a Conference: Solidification and Casting of Metals, pp 389-400, Pub. London 1979, The Metals Society

[60] Ma, D., Meyer ter Vehn, M., Busse, P. and Sahm, P.R. "Solidification Behavior of Ni-Base Superalloy CMSX-6." Proceedings of a Conference: Euromat 93: The Third European Conference on Advanced Materials and Processes: Journal de Physique IV, Colloque C7, Suppl. JP III, vol 1, no.11. pp. 339-342. Ed. Pichoir, R. and Costa, P. Pub Nov 1993 Les Editions de Physique.

[61] Yu, K.O., Oti, J.A., Robinson, M. and Carlson, R.G. "Solidification Modelling of Complex Shaped Single Crystal Turbine Airfoils." Proceedings of a Conference: Superalloys 1992, pp.135-144. Ed. Antolovich, S.D. Pub. The Minerals, Metals and Materials Society 1992.

[62] Tiller, W.A., Jackson, K.A., Rutter, J.W. and Chalmers, B. *Acta Metallurgica*, vol. 1, 1953, pg. 428.

[63] Tien, J.K. and Gamble, R.P. *Materials Science and Engineering*, vol. 8, 1971, pg. 152.

[64] Bhambri, A.K., Kattamis, T.Z. and Morral, J.E. *Metallurgical Transactions*, vol.6B, 1975, pg. 523.

[65] Flemings, M.C. Solidification Processing. Pub. McGraw-Hill, New York, 1974.

[66] Copley, S.M., Giamei, A.F., Johnson, S.M. and Hornbecker, M.F. "The Origin of Freckles in Unidirectionally Solidified Castings." *Metallurgical Transactions*, vol. 1, Aug 1970, pg. 2193.

[67] Quested, P.N, McLean, M. and Winstone, M.R. "Evaluation of Electron-Beam Cold Hearth Refining (EBCHR) of Virgin and Revert IN738LC." Procedings of a Conference: Superalloys 1988. Ed. D.N. Duhl, Pub. The Minerals, Metals and Materials Society 1988.

[68] O'Connell, M.F., Biederman, R.R. and Morra, J.M. "Quantitative Characterization of Inclusions in Electron Beam Melted Rene 95 Buttons." Proceedings of a

Conference: Electron Beam Melting and Refining - State of the Art 1991. Reno, Nevada, Oct25-27, 1992. Bakish Materials Corp. Ed R. Bakish, pp. 151-169.

[69] Mitchell, A. "Thermochemistry of Inclusions in Superalloys" Proceedings of a Conference: Advanced Materials and Processing Techniques for Structural Applications, Paris 7-9 Sept., 1987, Pub. Office National D'Etudes et de Recherces Aerospatiales. Ed. Kahn, T. and Lasalmonie, A. pp. 233-241.

[70] Bol'shov, L.A., Stomakhin, A., Sokolov, V.M. and Teterin V.G. "Solubility of Nitrogen in Multicomponent Ni-Based Melts." (Izvestiya Akademii Nauk SSSR. No. 5 pp60-62 1984) Russian Metallurgy Metally, 1985, Pg 64-67. Pub. Allerton Press 1985.

[71] Lin, K.F., Lin, Y.L. and Hsu, S.E. "Interaction of Ceramic Shell Mold With Ni-Base Superalloy During Single Crystal Casting." Proceedings of a Conference: Superalloys 1984, Pub. The Minerals, Metals and Materials Society, 1984 pp. 285-293.

[72] Lux, B., Haour, G. and Mollard, F. "Dynamic Undercooling of Superalloys." Proceedings of a Conference: Rapid Solidification Processing Principles and Technologies, II. Ed. Mehrabian, Kear and Cohen. Second International Conference on Rapid Solidification, Virginia, March 1980. Pub. Claitor's Publishing Division, pp. 429-439.

[73] Lamberigts and Lecompte-Beckers. "Reverting Foundry Nickel-Base Superalloys." Proceedings of a Conference: High Temperature Materials for Gas Turbines and Other Applications. Liege, Belgium. Pub. Kluwer Academic Publishers 1986. pp. 777-787.

[74] Painter, R.E., Quested, P.N. and Young, J.M. "Effect of Nitrogen Additions on the Casting Quality of Ni-Based Superalloys." Solidification Processing 1987. The Institue of Metals, 1988. pp. 23-25.

[75] Chechenstev, V.N., Saburov V.P. and Zameshaev, E.V. "Bulk Inoculation of Ni Alloys for Casting Production." *Soviet Casting Technology*, vol. 9, 1988, pp. 34-36.

[76] Liu, Zhen, Banerji, Reif and Fu. "Effect of Solidification Parameters on the Microstructure of IN738LC Ni Based Superalloy." Proceedings of a Conference: The Eleventh Ineternational Conference on Vacuum Melting, 1992, pp. 83-85.

[77] Fredholm, A. Monocristaux D'Alliages A Base de Nickel; Relation Entre Composition, Microstructure et Comportement en Fluage a Haute Temperature, PhD Thesis: Ecole Nationale Superieure des Mines (Paris) 1987.

[78] Chehaibou, A. Formation et Evolution des Structures et des Microsegregations Lors de la Solidification Dirigee D'Alliages A Base de Nickel, PhD Thesis: Institute National Polytechnique de Lorraine 15 Nov 1988.

[79] Sellamuthu, R. and Giamei, A.F. "Measurement of Segregation and Distribution Coefficients in MAR-M200 and Hafnium Modified MAR-M-200 Superalloys." *Metallurgical Transactions A.* vol. 17A. March 1986. pg. 419.

[80] Willemin, P. Equilibre de Phase dans les Alliages A Base de Nickel Contenant de L'Aluminium, du Tantale and du Titane, PhD Thesis: Institute Polytechnique de Grenoble, France. 1988.

[81] Cook and Guthrie. *Foundry Trade Journal*, vol. 19, 1966, pg. 686.

[82] Siredey, N. Solidification de Monograins Base Nickel: Microstructure et Qualite Cristalline PhD Thesis: L'Institut National Polytechnique de Lorraine, 1991.

[83] Diffusion and Defect Data. vol. 8, no. 1-4, 1974. pg. 141 Ed. F.H. Wohlbier. Trans Tech Publications, Ohio, USA.

[84] Zou, J., Wang, H.P., Doherty, R. and Perry, E.M. "Solidification Behaviour and Microstructural Formation in a Cast Nickel Based Superalloy: Experiment and Modelling." Proceedings of a Conference: Superalloys 1992, Ed. Antolovich, S.D. Pub. The Minerals, Metals and Materials Society 1992.

[85] Superalloys, A Technical Guide. Ed. Bradley, E.F. Pub. ASM International, 1988.

[86] Bassler, B.T., Hoffmeister, W.F., Carro, G. and Bayuzick, R.J. "The Velocity of Solidification of Highly Undercooled Nickel." *Metallurgical Transactions A.* vol. 25A, June 1994, pp. 1301-1308.

[87] Rappaz, M. and Thevoz, Ph. "Solute Diffusion Model for Equiaxed Dendritic Growth: Analytical Solution" *Acta Metallurgica*, vol. 35, no. 12, 1987 pp. 2929-2933

[88] Ludwig, A., Steinbach, I., and Hofmann, N. "Modeling of Undercooling Effects During the Directional Solidification of Turbine Blades" Proceedings of a Conference: Modeling of Casting, Welding and Advanced Solidification Processes VI, Ed. Piwonka, Voller and Katgerman. Pub. The Minerals, Metals and Materials Society 1993. pp. 87-94.

[89] Cockcrocft, S.L., Rappaz, M., Mitchell, A., Fernihough, J. and Schmalz, A.J. "An Examination of Some of the Manufacturing Problems of Large Single Crystal Turbine Blades for Use in Land-Based Gas Turbines" Proceedings

of a Conference: Materials for Advanced Power Engineering 1994, Ed. Coutsouradis, D. Pub. Kluwer Academic Publishers. pp.1145-1154.

[90] Lacaze, J., Chehaibou, A. and Lesoult, G. "Microsegregations During Directional Solidification of a Ni-Al-Ta Alloy." *Zeitschrift Für Metallkunde*, vol. 80, Jan. 1989, Heft 1, pp. 15-20.

[91] The Omega Complete Temperature Measurement Handbook and Encyclopedia. Vol 28, Pub. 1992, Omega Engineering, Inc. pg. A8.

[92] ASM Engineered Materials Reference Book, Pub. ASM International, 1989. Pg. 168.

[93] Hansen, M. and Anderko, K. Constitution of Binary Alloys. Second Ed. (1958) Pub. MacGraw-Hill, New York.

[94] Christian, J.W. The Theory of Transformations in Metals and Alloys. Pub. Pergammon Press, Oxford, 1975. pg. 17.

[95] Dominick, B. "Mathematical Modelling of Heat Transfer in the Vacuum Investment Casting of Superalloy IN718. MASc Thesis: The University of British Columbia1993.

[96] The Iron and Steel Institute. Proceedings of a Conference: "The Solidification of Metals" Brighton, U.K. 4-7 Dec. 1967. ISI Pub 110.